

Force Generation by Growing Microtubules

Force Generation by Growing Microtubules

PROEFSCHRIFT

TER VERKRIJGING VAN
DE GRAAD VAN DOCTOR
AAN DE UNIVERSITEIT LEIDEN,
OP GEZAG VAN DE RECTOR MAGNIFICUS DR. D.D. BREIMER,
HOGLERAAR IN DE FACULTEIT DER WISKUNDE EN
NATUURWETENSCHAPPEN EN DIE DER GENEESKUNDE,
VOLGENS BESLUIT VAN HET COLLEGE VOOR PROMOTIES
TE VERDEDIGEN OP WOENSDAG 20 NOVEMBER 2002
TE KLOKKE 14.15 UUR

DOOR

MARCEL ERNESTUS JANSON

GEBOREN TE DRACHTEN IN 1972

Promotiecommissie:

Promotor: Prof. dr. M. Dogterom
Referent: Prof. dr. E.D. Salmon (University of North Carolina, USA)
Overige leden: Prof. dr. R. Bruinsma
Prof. dr. T. Schmidt
Prof. dr. C.F. Schmidt (Vrije Universiteit Amsterdam)
Prof. dr. J.T.M. Walraven (Universiteit van Amsterdam)
Prof. dr. B.M. Mulder (Wageningen Universiteit)
Prof. dr. P.H. Kes

Force generation by growing microtubules
Marcel Ernestus Janson

Cover: Iliya Cerjak

ISBN 90-801704-9-6

A digital version of this thesis can be downloaded from <http://www.amolf.nl>

The work described in this thesis was performed at the FOM Institute for Atomic and Molecular Physics (AMOLF), Kruislaan 407, 1098 SJ Amsterdam. This work is part of the research program of the "Stichting voor Fundamenteel Onderzoek der Materie (FOM)", which is financially supported by the "Nederlandse organisatie voor Wetenschappelijke Onderzoek (NWO)".

aan mijn ouders

This thesis is partly based on the following articles:

M. Dogterom, M.E. Janson, C. Faivre-Moskalenko, A. Van der Horst, J.W.J. Kerssemakers, C. Tanase and B.M. Mulder,
Force generation by polymerizing microtubules, (Chapters 3 and 6)
Applied Physics A-Materials Science & Processing **75**, 331-336 (2002).

M. Dogterom and M.E. Janson,
Duwen en trekken in de cel, (Chapters 3 and 6)
Natuur en techniek **68**, 22-27 (april 2000), in dutch.

M.E. Janson, M.E. de Dood and M. Dogterom,
Force induced dynamic instability of microtubules, (Chapter 4)
submitted.

M.E. Janson and M. Dogterom,
Force-velocity curves for single microtubules, (Chapter 3)
in preparation.

M.E. Janson and M. Dogterom,
Rigidity measurements on elongating microtubules, (Chapter 5)
in preparation.

J.W.J. Kerssemakers, M.E. Janson, A. Van der Horst and M. Dogterom,
An optical trap set-up for measuring cytoskeletal pushing forces, (Chapter 6)
in preparation.

E.E.F. Riemsdag, M.E. Janson and M. Dogterom,
Motor proteins as couplers to growing microtubules, (Chapter 6)
in preparation.

M.E. de Dood, M.E. Janson and M. Dogterom,
Catastrophe statistics for stalled microtubules, (Chapter 4)
in preparation.

Contents

1	Introduction	9
1.1	Microtubules: dynamic assemblies in living cells	9
1.2	Experimental evidence for force generation by cytoskeletal filaments	14
1.3	Energetics of assembly driven motion	17
1.4	Thesis layout	22
2	Experimental set-up and data analysis	23
2.1	Design considerations	23
2.2	Construction of barriers	24
2.3	Synthesis of nucleation sites	27
2.4	Preparation of the sample cell	28
2.5	Microscopy and image analysis	30
2.6	Theory of buckling	33
2.7	Curve fitting	37
2.8	Acknowledgements	41
3	The effect of force on microtubule growth velocity	43
3.1	Introduction	43
3.2	Materials and methods	44
3.3	Results	46
3.4	Discussion	56
3.5	Acknowledgements	62
4	Dynamic instability of microtubules under load	63
4.1	Introduction	63
4.2	Materials and methods	64
4.3	Results	65
4.4	Discussion	72
4.5	Acknowledgements	75
5	Rigidity measurements on growing microtubules using higher order thermal shape fluctuations	77
5.1	Introduction	77
5.2	Materials and methods	80

Contents

5.3	Results	94
5.4	Discussion	101
5.5	Acknowledgements	106
6	Final considerations and new research directions	107
6.1	Probing microtubule dynamics with optical tweezers	107
6.2	Motor proteins as linking agents to growing microtubules tips	112
6.3	On the mechanism of dynamic instability	120
6.4	Acknowledgements	124
	Bibliography	125
	Summary	133
	Samenvatting	137
	Nawoord	141
	Curriculum Vitae	143

I

Introduction

Living cells consist for a large part out of proteins that interact with each other. These interactions change continuously, which causes live to be dynamic and not static. Some proteins are designed to bind to identical duplicates and assemble into long filamentous structures, which form the cytoskeleton of the cell. These filaments can generate pushing forces when assembly takes place near growth opposing cellular structures like chromosomes. Cells are known to exploit these forces to remodel their internal structure continuously. This thesis deals with forces generated by specific filaments called microtubules but many of the described observations have implications to other cytoskeleton filaments as well. Microtubules are important for numerous cellular processes including cell division and have remarkable assembly properties. In this first chapter I will describe concepts that are used to describe these properties. I will summarise evidence for force generation by assembly in living cells and in experimental model systems. A physical framework for the description of the effect of force on assembly properties will be outlined.

1.1 Microtubules: dynamic assemblies in living cells

Living cells contain a complex mixture of many molecules, which include proteins, DNA, lipids, water and many other small molecules [1]. When viewed with a microscope cells appear to be highly organised and one can observe all kind of structural details. Cells are thus no small bags filled with a homogeneous mixed substance but molecules self-assemble to form cellular structures like chromosomes or mitochondria. Cells are never at rest but can grow, divide or just do their work like a muscle cell that contracts. In

Chapter 1

these processes cellular structures are constantly remodelled. Somehow the cell must be able to exert mechanical forces in order to accomplish these changes. It is now well established that protein molecules are able to convert chemical energy into mechanical energy. This thesis deals with forces that can be generated by the proteins that form the cytoskeleton.

Role of cytoskeletal filaments

Especially in eucaryotic cells, which include animal and plant cells, one can find a remarkable system of filaments called the cytoskeleton [1]. Identical proteins are able to bind to each other and thereby form these long elongated filaments. Actin proteins assemble into actin filaments and tubulin proteins form thin hollow tubes called microtubules. Intermediate filaments are the third member of the cytoskeletal family. Cytoskeletal filaments are used by the cell as structural components to support for example the fragile plasma membrane or for constructing the tail of a sperm cell. Without a cytoskeleton most cells would collapse under external pressure. Besides this static structural function, the cytoskeleton plays other more dynamic roles. Together with motor proteins the cytoskeleton takes care of intracellular transport and force generation. Motor proteins can bind to cytoskeletal filaments and translate along their protein lattice in a directed manner [2]. These proteins are able to change their shape by a conformational change using chemical energy available through the hydrolysis of Adenosine Tri-Phosphate (ATP). By a sequence of binding and unbinding events between the shape changing motor protein and the filament, a motor protein can move to the next lattice site. Much work has been done in characterising these events and motors have been studied on a single molecular level [2-4]. In fact, research on motor proteins is a very active field within biophysics. In living cells motors play many roles in combination with cytoskeleton filaments. Motor proteins when attached to lipid membranes organise the shape of the endoplasmic reticulum [5,6] or transport other proteins to the tips of long axons in neuronal cells [1]. In muscle cells myosin motors walk along filaments build from actin to contract these cells and thereby perform work [1]. Apart from their interactions with motor proteins, cytoskeleton filaments are involved in dynamic force generation in a second much less studied manner. When elongating or shrinking, filaments can push and respectively pull on objects connected to their ends [2]. These forces are applied to move complete cells like fibroblasts, organise the mitotic spindle before cell division (Fig. 1.2) or propel pathogens like *Listeria monocytogenes* and *Shigella flexneri*. In this thesis I will focus on force generation by elongating microtubules.

Microtubule dynamics

In solution, α - and β -tubulin, which have strong sequence and structural similarity [7], form dimers with a total molecular mass near 100,000 D. Both dimer subunits bind one Guanosine Tri-Phosphate (GTP) molecule. Dimers assemble into long tube like structures

Introduction

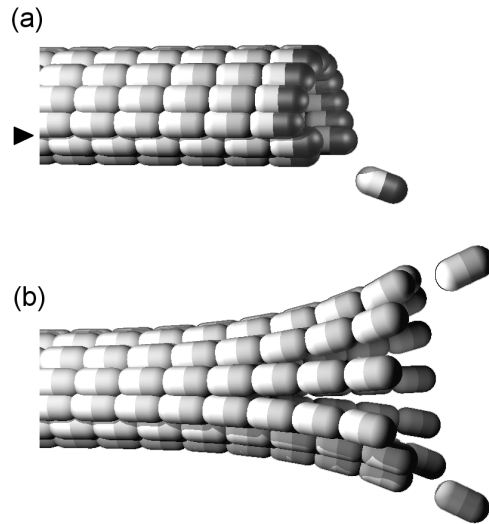


Figure 1.1 A schematic representation of the structure of (a) an elongating and (b) a shortening microtubule. Microtubules contain 8 nm long tubulin dimers formed from α - (white) and β -tubulin (grey). All dimers have the same polarity and lateral contacts between the approximately 13 protofilaments are made mainly by α - α and β - β bonds except at the two protofilaments that form the seam (arrow) where α - β bonds are formed. The plus end (right side) has exposed β -subunits that may have predominantly GTP bound (black), whereas GTP has been hydrolysed to GDP in the remaining β -subunits. Somehow the number of GTP- β -subunits at the tip regulates the stability of a microtubule against catastrophes. The number of GTP-subunits needed for stabilisation is under debate. The tip of an elongating microtubule is not always closed into a cylinder, as in (b), but sheets of protofilaments have been reported at elongating tips [16,59]. Microtubule shortening, which is initiated by a catastrophe, is marked by protofilament peeling. First the lateral contacts between protofilaments are lost which are then rapidly disassembled into free dimers. Extended peeled filaments or 'rams horns' are only seen under conditions that stabilise the bond between two dimers [60]. Dimers in solution can exchange GDP for GTP and can be reused. The diameter of a microtubule is around 25 nm.

[8,9] each containing approximately 13 so called protofilaments that are laterally connected (Fig. 1.1). Because of their structure microtubules are much stiffer than actin filaments [10] (only two sub-filaments) or intermediate filaments. Microtubules are able to withstand significant forces without collapse over length scales equal to the size of living cells, typically several tens of micrometers.

Microtubules show remarkable assembly behaviour that has been the focus of many studies which were reviewed by Desai and Mitchison [9]. Microtubules nucleate spontaneously in purified solutions of tubulin-dimers (*in vitro*) if the dimer concentration is high enough [11]. In living cells (*in vivo*), microtubules often elongate from pre-assembled nucleation sites as can be found for example in the centrosomes of animal cells

Chapter 1

[1,12] (Fig. 1.2). Both microtubule ends show different dynamic behaviour. The faster growing end is termed the plus end and has β -tubulin exposed whereas the minus end has exposed α -tubulin (Fig. 1.1). Conformational changes in the proteins that take place after assembly are believed to be responsible for the observed asymmetry in dynamics. Both *in vivo* and *in vitro*, elongating microtubules are seen to coexist with rapidly shrinking microtubules. Apparently microtubules can alternate between phases of elongation and shortening, which is termed dynamic instability [13]. The switch from elongation to shortening is termed a catastrophe whereas the opposite is called a rescue. An elongating microtubule never reaches a steady state length for which there is an equilibrium between the rates at which new dimers are added and removed. Catastrophes prevent microtubules from reaching an equilibrium length. The assembly process occurs far from equilibrium.

Dynamic instability is somehow related to hydrolysis of GTP at the β -tubulin. GTP at the α -tubulin subunit can not be hydrolysed. Microtubules grown in the presence of the slowly hydrolysable GTP-analogue GMPCPP [14] do not show catastrophes indicating that elongation does not require GTP hydrolysis whereas dynamic instability does. GDP tubulin, i.e. tubulin dimers with hydrolysed GTP at the β -side, can assemble into single filament closed rings [15] with a curvature resembling the filament curls that can be observed at the tip of disassembling microtubules (Fig. 1.1b) with the electron microscope [16,17]. Apparently the energy of GTP hydrolysis is used to curve the tubulin dimers, which creates stress inside the microtubule lattice. The microtubule is hypothesised to be stable during elongation because a few terminating subunits that did not hydrolyse their GTP keep the protofilaments together (Fig. 1.1a). The outcome of the tug-of-war between protofilament peeling and lateral binding [18] depends on the amount of GTP-tubulin in the stabilising cap. The dynamics of cap loss (catastrophe), recapping (rescue) and possible intermediate states (pauses during elongation and shortening) are not well understood at the molecular level. High levels of free GTP-dimers clearly stimulate elongation and decrease the catastrophe probability [11,19]. *In vivo*, many proteins have been found that regulate dynamic instability. This was clearly demonstrated in cellular extracts where the addition of one single regulatory protein which is at the top of a chain of regulatory processes dramatically changed the occurrence of catastrophes and thereby the average microtubule length [20].

Microtubules during cell division

The regulation of microtubule dynamic instability inside living cells is very clearly seen before and during cell division when the mitotic spindle [1,21,22] is formed by microtubules. The main events that eventually lead to cell division are depicted in Fig. 1.2 for an animal cell. Before cell division (interphase), all the genetic information of the cell that is encoded in the DNA is confined within the cell nucleus. Connected to the cell nucleus is a single centrosome which radiates relatively long stable microtubules (Fig. 1.2a). Before the start of cell division, the cell duplicates both its DNA and centrosome.

Introduction

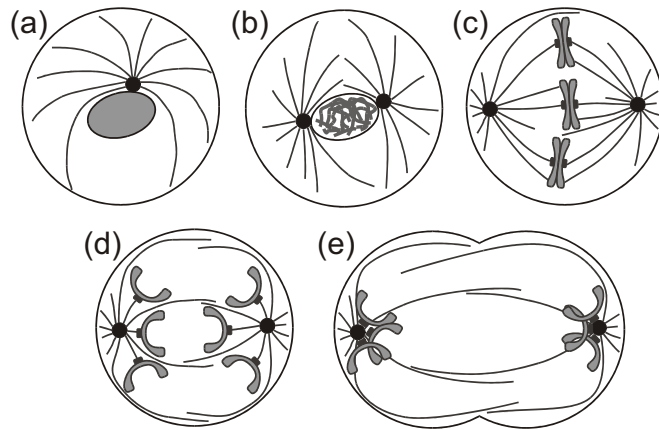


Figure 1.2 The cell cycle of animal cells is subdivided into different characteristic stages [1]. These stages are described in the text. (a) Interphase. (b) Prophase. (c) Metaphase. (d) Anaphase. (e) Telophase. Note that prometaphase and cytokinesis are not represented here. Centrosomes are represented as dark filled circles with microtubules radiating as curved lines. The cell nucleus is shown as a grey blob that later falls apart into chromosomes with two kinetochores (dark grey dots) attached to them. Only a fraction of the total number of microtubules is depicted. Many microtubules attach to a single kinetochore.

Then at the onset of cell division, the DNA condenses into the much more compact chromosomes (Fig. 1.2b) which are released when the nuclear envelope breaks down. Chromosomes each contain two closely associated identical sister chromatids. At this stage, the microtubules are very dynamic and often switch from elongation to shortening. Tips of growing microtubules attach to specialised protein complexes on the chromatids called kinetochores (Fig. 1.2c). After some time each chromosome is connected to microtubules emanating from both centrosomes. These bi-oriented chromosomes oscillate between motion towards the left or the right centrosome, which corresponds to microtubule elongation at one kinetochore and disassembly at the other [22]. Both growing and shrinking microtubules can stay attached to the kinetochores. When all chromosomes are bi-oriented in the middle of the cell the connection between sister chromatids is lost and kinetochore connected microtubules disassemble and pull the chromatids towards their corresponding centrosome (Fig. 1.2d). Then, when the chromatids are near the centrosomes, the distance between the centrosomes is increased involving long overlapping microtubules and the plasma membrane contracts in the middle of the cell eventually leading to two cells (Fig. 1.2e).

The motions observed during cell division are generated by a complex cooperation between microtubules and motor proteins [21,23,24]. Motor proteins are connected to the kinetochores and chromosome arms and exert forces along the microtubules. Other motors

Chapter 1

form complexes which generate forces between overlapping microtubules. As mentioned earlier, microtubules themselves can generate pushing and pulling forces when growing or shrinking and motor proteins might function to couple microtubule force generation to motion of the chromosomes. Growing microtubules impinging on chromosomes are likely to generate pushing forces and generate so called polar ejection forces away from the centrosomes that form the poles of the mitotic spindle. The tug-of-war between pulling forces generated by shrinking kinetochore-attached microtubules and the polar ejection force is believed to be responsible for chromosome alignment and the oscillatory motions observed [22,25,26]. The enormous complexity of the system makes it difficult to establish what the individual roles are of microtubules and motors in the spindle. To fully understand the build up and dynamics of the mitotic spindle, we need insight in the biochemical regulation of motors and microtubule dynamics and we should be able to answer questions like ‘Do motors effect microtubule dynamics?’ and ‘What is the effect of force on growth dynamics of individual microtubules?’. This thesis will mainly deal with the last question. In the following paragraph we will first summarise evidence for force generation by cytoskeleton filaments.

1.2 Experimental evidence for force generation by cytoskeletal filaments

Because tubulin and also actin assembly processes occur far from equilibrium, there is for both filamentous systems a strong drive towards assembly. The question can be asked whether the cell harnesses this potential to generate useful work. There are an increasing number of reported cellular observations that provide strong evidence that the cell actually does use assembly driven force generation. Observations in living cells are often difficult to interpret because it is hard to ascertain the individual roles of force generating motor molecules and force generating cytoskeletal filaments. However, many *in vitro* observations using simplified model systems have proven unambiguously that filaments are indeed able to generate force. Biological examples where cytoskeletal filaments are believed to generate force have been reviewed in general [27] and for actin [28] and microtubules [29] separately.

Actin force generation

Growth of actin filaments is believed to produce force inside living cells to push the plasma membrane of crawling cells forwards (Fig. 1.3a). Assembly seems to be the mayor force generating mechanism because knocking out motor proteins could not stop the locomotion of these cells whereas drugs that prevent actin filament elongation stopped membrane protrusions. A recent report on actin dynamics near the leading edge of these cells [30] showed that filament elongation is slower in the direct vicinity of the membrane, which seems in agreement with a regulatory effect of force on elongation as suggested by theoretical models [31-33]. Analysis of the forces involved in protrusion showed that actin

Introduction

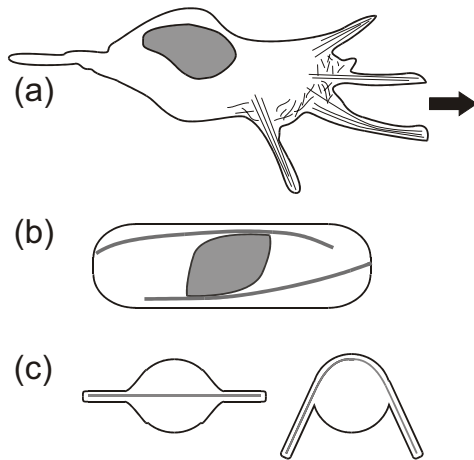


Figure 1.3 Examples of force generation by assembling cytoskeletal filaments. (a) Actin filaments inside crawling cells assemble in close proximity of the outer membrane and form gel-like networks and bundles. Figure adapted from [1]. (b) In the fission yeast, microtubules attached to the nucleus (grey blob) grow towards the cellular ends and upon arriving they exert forces that deform and position the nucleus. Figure after [42]. (c) Microtubules trapped inside lipid vesicles are able to extend sleeve-like membrane protrusions. Involved forces are large enough to buckle 7.5 μm long microtubules. Figure adapted from [46].

alone might be capable of generating sufficient force [34]. Actin dynamics is often harnessed as well to generate force during fertilisation. The sea cucumber *Thyone* forms a 60 μm long bundle by rapid assembly of a highly concentrated pool of actin monomers [27,28,35]. A different filamentous system, called MSP, is likely to generate the crawling motion of sperm cells of worms like *Ascaris* [36,37]. Actin assembly also plays an eminent role in the propulsion of pathogens like *Listeria Monocytogenes* and *Shigella flexneri* [38]. These pathogens are capable of generating a cross-linked actin gel that propels them forward. Similar motions were observed *in vitro* on actin-nucleating micrometer-sized beads [39].

Microtubule force generation

The discussion about assembly-driven force generation by microtubules in living cells has mainly focused on the processes of cell division and positioning of the cell nucleus. In living cells the nucleus is believed to be centred by a microtubule aster that is radiated by a nucleus-attached centrosome or other microtubule nucleating structure. An additional action of motor proteins can, however, not be ruled out [40,41]. Proof for a microtubule-based pathway came from experiments in the fission yeast where the limited number of microtubules allows for a clear visualisation of the role of individual microtubules. Microtubules were seen to deform the nuclear membrane when contacting the cellular ends [42] (Fig. 1.3b). The direction of deformation seems to rule out pulling by motor

Chapter 1

proteins at the cellular ends and it is the combined action of several microtubules that pushes the nucleus towards the cell centre. This mechanism is important for a correct cell division.

The pushing forces, or polar ejection forces, generated by the mitotic spindle during cell division have been assessed by cutting chromosomes using the cutting action of a focused laser beam [43]. Parts of chromosome arms missing a kinetochore were seen to move away from the densely packed centre of microtubule asters. The local density of microtubules clearly effected this force, but a combined mechanism with motor proteins can not be ruled out. Arms of chromosomes are known to bear motor proteins [44].

In vitro results

Convincing evidence for force generation *in vitro* first came from experiments where non-assembled cytoskeletal subunits were enclosed inside lipid vesicles. During the assembly of filaments the vesicle loses its characteristic spherical shape and spike-like protrusions are reported for actin filaments [45] and thinner sleeve-like protrusions for microtubules [46]. These filaments were thus able to generate the force needed to deform vesicles. Buckling of 7.5 μm long possibly individual microtubules inside vesicles was observed (Fig. 1.3c), which indicated that microtubules are able to generate forces on the order of 2 pN. Both growth and microtubule dynamic instability sustained during force generation. Subsequently, a new model system was developed to allow for a better quantitative control over the generated force. Microtubules attached with one end to a substrate were observed to buckle when their growing end pushed against a microfabricated rigid barrier [47]. Microtubule growth velocity was studied as a function of force by observing different microtubule lengths. Velocity decayed as a function of force and a maximum force of 4 pN was measured. The rate of decay was shown to contain valuable information about the microtubule tip structure and assembly behaviour in general [47,48]. I will come back to these issues later on in this chapter.

Again other experimental systems were developed to study the mechanism underlying the centring of a nucleus by an aster of microtubules in the confined geometry of the cell. *In vitro*, an aster of microtubules was shown to be able to find the geometric middle of a confining box using forces generated by microtubule assembly [49]. Dynamic instability was shown to be a crucial requisite [50,51].

Pulling forces

Apart from pushing forces, cytoskeletal filaments can generate pulling forces as well. After a catastrophe, a microtubule has a strong drive towards disassembly, which might pull on objects that are able to stay attached to a disassembling tip. In an *in vitro* assay, chromosomes connected to microtubules were seen to be pulled along with a shrinking microtubule end after a catastrophe was induced [52]. The fact that this motion persisted in the absence of ATP indicated that microtubules can generate, without an active role of

Introduction

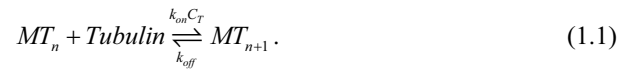
motor proteins, a pulling force enough to work against the viscous drag that acts on the attached chromosome. Additional evidence for pulling forces came from both *in vivo* and *in vitro* work on endoplasmic reticulum membranes that are distributed by microtubules and motors [5,6]. Membrane tubules were formed by both elongating and shrinking microtubules that attached to the membranes by specialised linking proteins. Even in the absence of ATP, pushing and pulling forces were generated.

1.3 Energetics of assembly driven motion

Microtubule growth is possible because the free energy is lowered when a GTP-tubulin dimer binds to a microtubule [2,9]. How much the free energy is lowered depends on the concentration of free tubulin dimers. If a microtubule has to grow against a growth-opposing load, the free energy difference between the bound and unbound state is lowered [33,47,53,54]. Force thus effects the rate of microtubule assembly. The effect of force can be described in terms of force dependencies of molecular rate constants. Therefore we start with a description of the rate constants for freely growing microtubules.

Free microtubule growth

The reaction that extends a microtubule that contains n subunits with one extra subunit can be written as



The rate by which GTP-tubulin is assembled onto the microtubule is given by $k_{on}C_T$, with k_{on} the bimolecular on-rate constant ($\text{M}^{-1}\text{s}^{-1}$) and C_T , the concentration of GTP-tubulin [2,19]. The reverse direction occurs at the unimolecular off-rate k_{off} (s^{-1}). This rate describes how GTP-tubulin is released from the growing tip and should not be confused with tubulin release after a catastrophe. Using the rate constants we find the net assembly rate

$$\frac{dn}{dt} = k_{on}C_T - k_{off}. \quad (1.2)$$

Each tubulin dimer has a length of 8 nm [8] and an average microtubule contains 13 protofilaments. So each tubulin protein adds on average $\delta = 8/13$ nm to the length of a microtubule. The growth velocity is therefore given by

$$v = \delta(k_{on}C_T - k_{off}). \quad (1.3)$$

Chapter 1

According to this model, the growth velocity should increase linearly with tubulin concentration. This behaviour is indeed observed experimentally in numerous studies [14,16,19,55]. At the critical concentration, C_c , the on- and off-rate are in equilibrium and the growth velocity is zero. The critical concentration therefore equals

$$C_c = \frac{k_{off}}{k_{on}}. \quad (1.4)$$

The link between reaction energy and rate constants [33,53] is given by

$$\frac{k_{on} C_T}{k_{off}} = \exp\left(\frac{\Delta G}{k_B T}\right), \quad (1.5)$$

where ΔG is the difference in free energy between a free and a bound GTP-tubulin dimer. k_B is Boltzmann's constant (JK^{-1}) and T is the absolute temperature (K).

Assembly under load

Now that we made the link between energy and growth velocity, we can study assembly under load. As a first approximation, we model the microtubule as one single filament [33,47] with a decreased subunit size equal to $\delta = 8/13$ nm. The values for k_{on} and k_{off} remain the same. Now, imagine such a simplified microtubule propped up to an object that is pushed with a force, F , against the microtubule. In order to grow by one extra subunit the microtubule has to perform an amount of work against the load force equal to $F \cdot \delta$. The energy difference between bound and unbound state [33,53,54] is lowered by this amount,

$$\Delta G^* = \Delta G - \delta F. \quad (1.6)$$

A star in general denotes a quantity under load. The rate constants under load are given by inserting the new free energy difference into Eq. 1.5,

$$\frac{k_{on}^* C_T}{k_{off}^*} = \exp\left(\frac{\Delta G - \delta F}{k_B T}\right) = \frac{k_{on} C_T}{k_{off}} \exp\left(-\frac{\delta F}{k_B T}\right). \quad (1.7)$$

An expression for the growth velocity under load can only be obtained if we make an assumption about how the effect of force is distributed amongst k_{on} and k_{off} . If we assume that the off-rate is not effected by force [47,53,54], we obtain the following force-velocity relation.

$$v = \delta \left(k_{on} C_T \exp\left(\frac{-F \delta}{k_B T}\right) - k_{off} \right). \quad (1.8)$$

Introduction

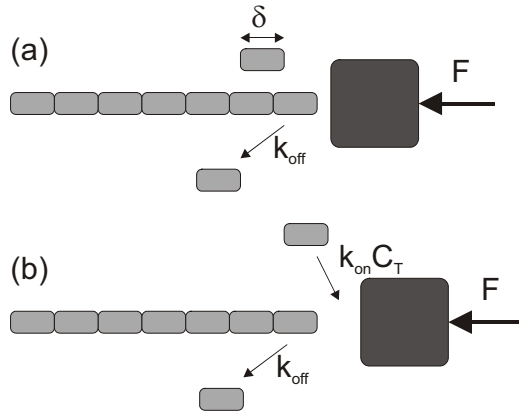


Figure 1.4 Force generation by a ratchet mechanism. (a) An object with a diffusion constant D is pushed against a growing filament with force F . When there is not enough space between the object and filament for the insertion of a new subunit, the only possible process is a slow disassembly with rate k_{off} . (b) Thermal fluctuations occasionally create enough space to allow for new insertions with rate $k_{on}C_T$, while disassembly remains possible. Redrawn from [54].

This expression is plotted in Fig. 1.6 for one set of rate constants. In chapters 3 and 4 we will present evidence for a force-independent off-rate. If the force is increased the on-rate will eventually drop below the off rate and the microtubule will shrink under load. A situation of zero growth is obtained at the stall force, which can be calculated by setting Eq. 1.7 equal to one [33,53,54]

$$F_{stall} = \frac{\Delta G}{\delta} = \frac{k_B T}{\delta} \ln \left(\frac{k_{on} C_T}{k_{off}} \right). \quad (1.9)$$

Brownian ratchet models

The analysis outlined above shows that growth is thermodynamically allowed under load. This is somewhat surprising because at first sight there is just no space between an object and a microtubule for new subunits to be inserted. Therefore, it was proposed to describe assembling cytoskeleton filaments as a Brownian ratchet [32]. Although the object is pushed against the microtubule, thermal fluctuations allow the object to diffuse away from the microtubule over small distances (Fig. 1.4). If diffusion of the gapsize is slow compared to assembly, a new subunit will be added every time the gapsize equals δ . The gapsize will thus never exceed δ . The time scale at which fluctuations of size δ occur is a first passage time problem [2,32]. At zero force this time on average equals $\delta^2/2D$ and the maximal speed that can be obtained in a diffusion-limited process therefore equals

Chapter 1

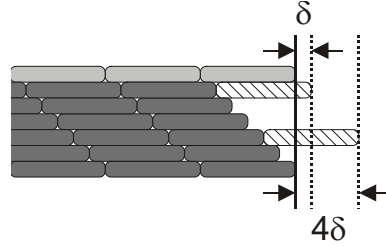


Figure 1.5 Schematic arrangement of protofilaments in a microtubule lattice. Displayed is an unfolded microtubule consisting, for simplicity, out of six protofilaments (dark grey) ordered in a staircase manner. The sixth protofilament is drawn for a second time (light grey) to show the lateral contacts made when the microtubule is folded into a tube. Binding of new dimers (hatched) at different positions will change the total length of a microtubule by multiples of δ , which is the average length increase. If lateral connections between filaments are strong then an extension with only one δ will be the most likely event, because for this event the lateral binding energy is larger.

$$v_{F=0} = \frac{\delta}{t_{\delta}(0)} = \frac{2D}{\delta}. \quad (1.10)$$

Note that we disregarded the off-rate, which is much smaller than the on-rate except at high forces.

If diffusion is fast, the gap-size can become larger than δ without immediate insertion of new subunits. So of all excursions larger than δ only some are used for assembly. For a non-growing microtubule, the probability of a gap larger than δ is given by a Boltzmann-distribution [56]

$$p(x > \delta) = \exp\left(-\frac{Fx}{k_b T}\right), \quad (1.11)$$

where x is the distance between microtubule and barrier. We can weigh the assembly rate with the probability of gap formation larger than δ and obtain a force-velocity relation identical to Eq. 1.8. Again we assumed no effect of force on k_{off} . Note the complete absence of D in Eq. 1.8. It is the maximum assembly rate that limits the velocity and the process is called reaction limited. The Brownian ratchet model and the thermodynamic arguments used in Eq. 1.7 yield the same force-velocity relation. The Brownian ratchet thus explains that growth under load is possible by gap formation due to Brownian motion. To obtain the thermodynamic prediction (Eq. 1.8), which describes the maximum possible velocity, we had to assume that diffusion between microtubule and object is fast. For the experimental system developed by Dogterom and Yurke [47] this was shown to be the case [48]. In the living cell it may depend on the specific configuration and the properties of the object against which is pushed.

Introduction

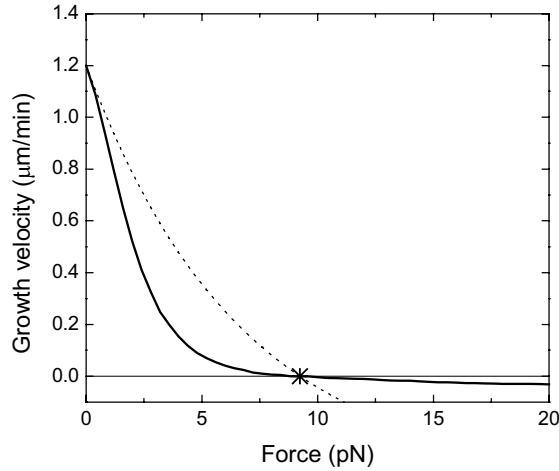


Figure 1.6 Force velocity curve for different assumptions about the growth process. The thermodynamic upper limit for ordered growth (dashed line, Eq. 1.8) and the zero lateral interaction limit for random growth [48] (straight line) are both plotted for $k_{on}C_T = 43.3 \text{ s}^{-1}$ and $k_{off} = 10.8 \text{ s}^{-1}$. The two curves coincide at the stall force, which is given by Eq. 1.9 and is indicated by a star. The number of protofilaments is 13. Figure is adapted from Doorn *et al.* [53].

Filaments with small lateral interactions

So far, we assumed that microtubule growth occurs in an ordered manner, for which all elongations have the same size, δ . This seems a reasonable assumption because the protofilaments in a microtubule are arranged in a staircase manner (Fig. 1.2 and 1.5). However, protofilaments do not necessarily wait for their neighbours to grow and they may grow independently of each other. If the filament that already extended most grows by an extra subunit the length increase of the microtubule is a full 8 nm, whereas a filament that is deeply buried does not elongate the microtubule at all (Fig. 1.5). For growth under a load this means that some filaments stay stochastically behind while others have to perform extra work. The force-velocity curve was calculated for filaments with zero lateral interaction using a Brownian ratchet model [48]. An exact solution of the model can not be given, but the model can be simulated using discrete time steps [48,53]. A simulation result is plotted in Fig. 1.6. for a set of rate-constants that describes the experimentally observed force-velocity curve well [47]. The decay of the velocity with force is faster than in Eq. 1.8 (Fig. 1.6). At high loads it becomes very unlikely that filaments grow in advance of other filaments. Filaments are made to grow in an ordered manner when generating force even though they don't have strong lateral interactions. The stall force for this model can be shown to be identical [53] to Eq. 1.9 for which initially ordered growth was assumed (see Fig. 1.2). More elaborate models for which the relative strength between longitudinal and lateral bonds can be varied were developed [57].

Chapter 1

We should keep in mind that a microtubule is more complex than outlined above. For example, hydrolysis of GTP at the tubulin dimers at the tip [9,58] may change molecular rates. The extent at which this occurs is not clear from the literature. Although the results described in this section were obtained using a simplified view on the microtubule, they do show that the force-velocity curve for assembling microtubules contains important information about molecular details of the assembling microtubule tip.

1.4 Thesis layout

In this thesis I present experimental work on force generation by assembling microtubules using a similar model system as used by Dogterom and Yurke [47]. Our goal is to study the mechanism behind microtubule force generation in a more elaborate way by changing the concentration of tubulin dimers in solution. A correct description of force generation should describe all available data. At the same time, we want to assess whether force affects the rate at which microtubules undergo catastrophes. A possible regulatory effect of force on catastrophes is of interest for example for the study of microtubule dynamics during spindle build up or nuclear positioning.

The choice for microtubules as a model system to study assembly-driven force generation is partly practical and partly because of relevance to living cells. Microtubules are very rigid structures and therefore it is experimentally feasible to apply a compressive force of relevant magnitude. In chapter 2 of this thesis I describe the experimental system used for force measurements. In the described set-up, microtubules can assemble against barriers and as a consequence bend themselves. Methods were developed and rigidity measurements on microtubules were performed to quantify the generated assembly forces by measuring the extent of bending. In chapter 5, I describe a method to analyse thermally-driven shape fluctuations of growing microtubules. From this accurate rigidity estimates were obtained, which were shown to depend on assembly conditions.

In chapter 3 the forces generated by assembling microtubules were analysed in detail. Piconewton forces were measured and force generation was shown to occur at the expense of growth velocity. The decrease in velocity as a function of force was compared to theoretical models. This analysis showed that there is room for the living cell to optimise force generation. While the effect of force on growth velocity is of general importance to biopolymers, the effect described in chapter 4 is of specific importance to microtubules. It is shown that the rate at which microtubules undergo catastrophes is accelerated by force. This observation gives us a better understanding of the way microtubules facilitate organelle positioning inside living cells. Finally, in chapter 6, I will describe first results of two new experiments, designed to give additional insights into microtubule assembly. Optical tweezers were used to study force generation and microtubule growth in more detail and the interplay between molecular motors and assembling microtubules was studied to mimic part of the complexity of living cells.

II

Experimental set-up and data analysis

The results that are presented in chapters 3 and 4 of this thesis were obtained using the experimental methods that will be described here. The experiment is set up such that growing microtubules, nucleated from surface-connected seeds, do strike micro fabricated barriers. The goal of the experiment is to infer forces from the buckling of microtubules while they continue elongation after striking the barriers. We will start with describing the fabrication of barriers on top of glass cover slips. These barriers have shapes that maximize the chance that microtubules buckle after reaching the barriers. Then the synthesis of stabilized microtubules as nucleation sites and the methods used for linking them to the cover slip are described. We will explain image analysis methods that were used to quantify the observed shapes of buckling microtubules. A fitting algorithm was designed to fit these shapes to the theoretical shape of a buckled elastic rod. This algorithm and the equations of buckling are presented in the final two paragraphs of this chapter.

2.1 Design considerations

A schematic view of the desired experimental configuration is shown in Fig. 2.1. For the force generation experiment to work, microtubules growing from surface connected nucleation sites must be confined such that they push against the barriers. The sample cell should thus be designed to maximise the chance that a microtubule builds up a compressive force. Furthermore we should be able to observe the shape of a buckled microtubule while it is pushing.

Microtubules can be observed using video-enhanced differential interference contrast (DIC) microscopy [61]. In this microscopy technique visible light passes through the sample and the difference in index of refraction between the protein rich microtubule

Chapter 2

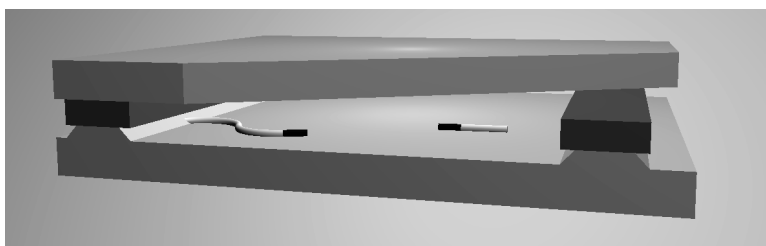


Figure 2.1 Schematic view of the experiment. Microtubules grow from surface-connected nucleation sites towards barriers. The barriers are deposited on the lower glass surface. A small ridge or overhang prevents microtubules from creeping up the barriers. Further confinement of the microtubules is obtained by pressing an agarose-coated glass slide on top of the barriers such that there is little room for the microtubules to grow over the barriers.

and the surrounding liquid is used for imaging. The sample cell needs to be transparent and therefore, we chose to construct barriers on top of glass cover slips. Microscope objectives are optimised for observations through these 170 μm thick cover slips.

The barriers that were used in the experiments are 15 mm long, 15 μm wide and 2 μm high. Two hundred of these barriers make up a 15 mm by 15 mm grid with a barrier spacing of 60 μm . A DIC microscope with oil immersion objective (100 \times , numerical aperture 1.3) was used for imaging. Microtubules positioned further than approximately 0.5 μm away from the focal plane were clearly out of focus. A small ridge, or overhang, under the barriers (see Fig. 2.1) is meant to catch the growing microtubule tip and hold it in the same plane as the nucleation site such that the whole microtubule remains in focus and can be imaged. Microtubules experience considerable Brownian motion that allows them to effectively search for ways to grow in an unconfined manner. Therefore, in an ideal sample, the glass slide that is pushed against the cover slip should contact the barriers such that there is no room for microtubules to grow over the barriers (see Fig. 2.1). To achieve contact, the glass slides were coated with a dried agarose gel [49]. By the application of pressure on the sample, the barriers will slightly indent the agarose layer. This technique was used but was not always successful. It was not possible to obtain a good contact over the complete 15 mm by 15 mm barrier area and many microtubules were observed to grow over barriers. Because enough microtubules did find the overhang and started buckling we decided to keep on using the agarose layer, which has the additional advantage of preventing protein sticking to the glass slides.

2.2 Construction of barriers

Standard photolithography techniques were used for making the barriers. These techniques are well developed and optimised for use on silicon as a substrate, but can be used on glass

Experimental set-up and data analysis

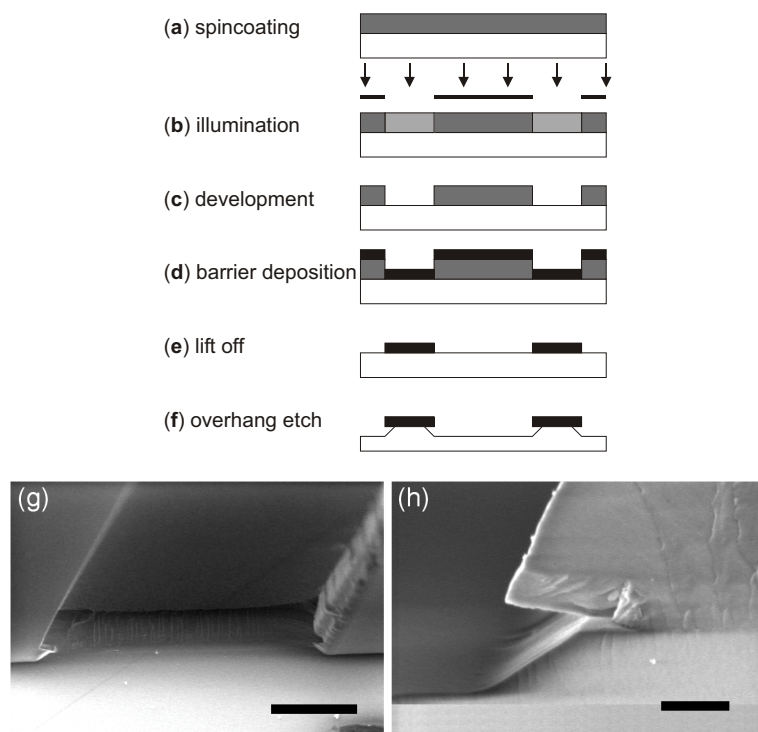


Figure 2.2 Steps taken in the barrier construction process as explained in the text. (a) Spincoating of photoresist (grey) on cover slips (white). (b) Illumination with UV light (arrows) through a mask. (c) Development of the photoresist (d) Deposition of SiO (black). (e) Lift off. (f) Etching of an overhang. (g) A low magnification view showing lines of SiO on top of a glass cover slip in cross section. Scale bar equals 5 μm . (h) Sample viewed at a higher magnification. The overhang is 0.5 μm deep. Scale bar equals 500 nm.

as well [47,49]. In short (Fig. 2.2), we created lines of photoresist, i.e. a light-sensitive polymeric material, on top of glass cover slips. A layer of silicon monoxide (SiO) was deposited in between and on top of the lines of photoresist. After this deposition, the photoresist was dissolved (lift off) which left only the SiO material that was deposited directly on the glass. The sample was then immersed in hydrofluoric acid, which etched into the exposed glass at a faster rate than into the SiO barriers thereby creating an overhang. The successive steps taken in the fabrication are:

Cleaning of glass cover slips. Cover slips sized 24 mm by 24 mm were placed in a teflon holder and immersed in chromosulfuric acid for a few hours. This procedure removed dirt and coatings from the surface. The samples were washed five times with deionised and filtered water (Milli-Q). Next the samples were placed for 10 minutes in a

Chapter 2

2M solution of NaOH in ethanol while sonicating. This dissolves a thin layer of glass and leaves a very clean surface. Again the samples were washed five times with water.

Application of photoresist. The samples were placed on a spin coater and a drop of hexamethyldisilazane (HMDS, Sigma) was spun at 3000 rpm for 30 seconds. Then a 7.5 μm thick layer of positive photoresist (ma-P 275, Micro Resist Technology, Berlin, Germany) was created by spinning 30 seconds at 3000 rpm. HMDS works as an adhesion agent between the glass and the photoresist. The photoresist was polymerised for 5 minutes on a hot plate at 100 °C.

Illumination and development. A photo lithographic mask was ordered from DIMES in Delft, The Netherlands. Using electron beam lithography, a pattern of chromium lines was created for us on top of a quartz plate. The photoresist layer on top of the cover slip was pressed against the chromium lines using a custom made sample holder. The sample holder was positioned in a beam from a 50 W mercury lamp for 2 minutes and the UV component in the light depolymerised the photoresist where it was not shielded by the chromium lines. We used a mercury lamp and lampholder originally designed for use on a microscope (Leica). Samples were then immersed for 1 minute in a developer (ma-D 330, Micro Resist Technology) which dissolved the exposed photoresist and were rinsed three times in water.

Deposition of barriers. Samples were immersed for 30 seconds in an 8% solution of hydrofluoric acid in water. This etches the glass in between the lines of photoresist without removing the photoresist. A clean glass surface was crucial for the adhesion of SiO. The samples were washed five times in water and dried for 15 minutes in an oven at 100 °C. Samples were mounted on a sample holder and were placed inside a vacuum deposition chamber. At a pressure of 1×10^{-6} torr, a layer of 2 μm thick SiO (Goodfellow) was vapour deposited. In this procedure the material is vaporised by heating. By electron microscopy we observed deformation of the photoresist lines which were rectangular in cross section before deposition but after deposition the angles were rounded off. We attributed this to heating of the sample which is indirectly heated as well during deposition. This was probably the cause of the non rectangular shape of the SiO lines shown in Fig. 2.2g, and h.

Lift off. The samples were put in a beaker with acetone, which dissolves the remaining photoresist. The SiO material deposited on top of the photoresist was removed at the same time. If the photoresist pattern is deformed during deposition, this lift off process is hindered because the SiO material on top of the photoresist connects to the material deposited in between the lines. Mechanical work with a cloth of tissue needed to be applied in order to break these connections. After the lift off the samples were cleaned with ethanol and water.

Etching. The samples were put in a buffered mixture of 25 ml hydrofluoric acid (40 % solution in water ordered from Fluka) and 235 ml ammonium fluoride (40 % solution in water, Fluka) for 7.5 minutes. The etch rate was about 70 nm/min in glass and

Experimental set-up and data analysis

slower in SiO. Sometimes the etching went much faster in the direction parallel to the SiO-glass interface. This was attributed to a poor adhesion of the SiO on the glass. The resulting barriers had overhangs of approximately 0.5 μm but deeper overhangs upto 3 μm were observed as well.

Electron microscopy. The barriers were observed by scanning electron microscopy (SEM). Therefore, samples were broken in a direction perpendicular to the barriers in order to view cross sections of the barriers. This procedure allowed the imaging of the overhang (2.2g, and h). The overhang of the barriers shown is about 0.5 μm deep. In this case adhesion of the SiO was good.

Recycling. The cover slips with SiO barriers could be re-used many times in an experiment. Between experiments the samples were cleaned using chromosulfuric acid.

2.3 Synthesis of nucleation sites

In the experiments described in the chapters 3 through 6, we grew microtubules from surface-bound nucleation sites. These sites, which we refer to as seeds, needed to be stable over the course of an experiment and had to stick to the surface in a controlled manner. In living cells nucleation sites pre-exist for example inside centrosomes. These sites are believed to be ring like structures that mimic the microtubule cross section and are able to bind free tubulin [62]. A second route to microtubule formation is self-nucleation that occurs when the concentration of tubulin dimers is high enough. *In vitro*, these conditions can be easily obtained [11]. At lower concentrations these microtubules disassemble as a consequence of dynamic instability. Self-nucleated microtubules can be stabilised and these stabilised structures can serve as sites for growth at concentrations below the limit for self-nucleation. Stabilisation can be achieved using the protein cross-linking agent EGS (ethylene glycol bis-(succinic acid)) that covalently links neighbouring proteins inside the microtubule lattice thereby preventing disassembly. Small seeds can be made by breaking long cross-linked microtubules. The nucleation probability of these structures is in general low because the protein structure is likely to be changed after cross-linking and all tubulin subunits have GDP bound whereas the tip of a growing microtubule contains GTP-tubulin. Alternatively one can self-nucleate microtubules using the slowly-hydrolysable GTP analogue GMPCPP [14]. These microtubules do not experience dynamic instability and disassembly rates are extremely low. The end of such a GMPCPP microtubule is likely to mimic very well the GTP-containing end structure of a growing microtubule and nucleation rates should therefore be large.

The binding between biotin and streptavidin is very generally applied to connect proteins to surfaces. The protein streptavidin has four binding pockets for the small vitamin biotin. The bond is non-covalent but very strong. We grew stable microtubules from biotin-labeled tubulin monomers and GMPCPP and bound them to streptavidin-coated cover slips. Seeds that were bound to the surface did not show the expected large

Chapter 2

nucleation rate. Probably, the forces involved in binding the microtubules to the surface prevent effective nucleation. Therefore we extended the biotin seeds with a small biotin free region before binding them to the surface. These seeds showed very fast nucleation especially at high tubulin concentrations ($> 10 \mu\text{M}$). New nucleation occurred within seconds after a catastrophe event disassembled a microtubule all the way back to the GMPCPP region.

Here we describe the synthesis of these seeds. The binding to streptavidin-coated surfaces is described in the next section.

Self-nucleation of GMPCPP microtubules. Unlabeled and biotin-labeled bovine brain tubulin were obtained from Cytoskeleton, Denver, CO at a concentration of $100 \mu\text{M}$. Because microtubule growth from biotin-labeled tubulin alone is slow we grew microtubules with a mixed lattice with a 4:1 labeled vs. unlabeled ratio. Biotin-labeled tubulin was supplied in a buffer containing 10% glycerol, which is known to increase the rate of GMPCPP hydrolysis manifold [63]. Tubulin was therefore first transferred to a glycerol free buffer. Labeled and unlabeled tubulin were mixed and diluted to $1 \mu\text{M}$ in MRB80-buffer (80 mM Pipes, 1 mM EGTA, 4 mM MgCl_2 , pH 6.8 titrated with KOH). This solution was spun through a Microcon 30 microconcentrator (30 kD molecular weight cut-off), diluted for a second time and again concentrated. Microtubules were assembled from $20 \mu\text{M}$ cleaned tubulin plus 0.5 mM GMPCPP (kindly provided by T.J. Mitchison) for 30 minutes at $35 \text{ }^\circ\text{C}$. After this period the solution is believed to be effectively depleted of free tubulin. Assembled microtubules were a few micrometers long.

Extension with biotin-free regions. Short microtubules were diluted 25 fold in MRB80 plus 0.4 mM GMPCPP and $0.62 \mu\text{M}$ unlabeled tubulin. This mixture was subdivided into small aliquots that were flash frozen in liquid nitrogen. Before an experiment an aliquot was thawed and biotin free regions were assembled on the pre-existing parts during 10 minutes at $35 \text{ }^\circ\text{C}$. This procedure was tested using $0.48 \mu\text{M}$ unlabeled tubulin and $0.14 \mu\text{M}$ rhodamine-labeled tubulin during extension. Using fluorescence microscopy small fluorescent spots with lengths less than $1 \mu\text{m}$, were seen on both sides of the preassembled parts. Self-nucleation is unlikely at this low tubulin concentration and no microtubules consisting out of rhodamine tubulin exclusively were detected.

2.4 Preparation of the sample cell

In order to achieve the experimental configuration depicted in Fig. 2.1, we first had to coat the cover slip with streptavidin, then allow the seeds to bind to the surface and finally add free tubulin and GTP to obtain microtubule growth. These actions could be most easily done using a flow cell. In a flow cell the cover slip is spaced at a certain distance from the glass slide. The liquid in between the two surfaces can flow and can thus be exchanged

Experimental set-up and data analysis

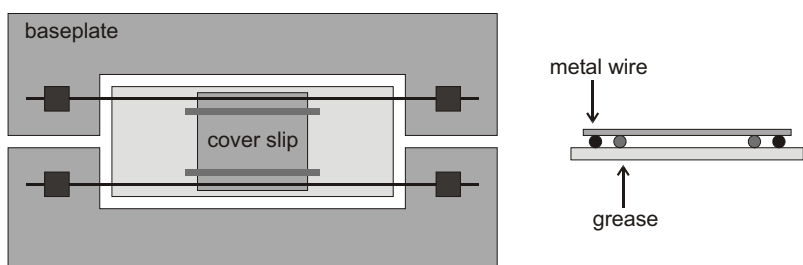


Figure 2.3 Schematic drawing of the flow cell. Two fine 25 μm thick metal wires (black lines) were placed on top of a 1 mm thick, 76 mm by 26 mm large agarose-coated glass slide. The metal wires were connected to two base plates that could be positioned around the glass slide (light grey). In between the metal wires two thin lines of vacuum grease (grey) were deposited using a syringe with a fine needle. A cover slip with barriers was positioned over these lines. Small pressure was applied on the grease such that the surface spacing decreased to approximately the thickness of the wires. After solutions were blotted true the flow cell the base plates with metal wires were removed and pressure, in the form of a 10 kg iron weight, was applied on the cover slip for several minutes while excess fluid was blotted with tissue paper. Especially in the middle of the flow cell, close contact between the surfaces could be achieved.

with other solutions. In order to control the flow of liquids the volume of the flow cell and thus the surface spacing must be known. The flow cell used is depicted in Fig. 2.3 and has the ability to decrease the surface spacing to zero for the final experiment in which microtubules must be prevented from growing over the barriers (see Fig. 2.1). Tissue paper was used to blot liquids at one side while new liquid was added at the other side using a pipette. The volume of the flow cell was approximately 10 μl . The steps taken to perform the experiment are listed below.

Agarose coating. A mixture of 4 mg/ml agarose in water was heated to 100 $^{\circ}\text{C}$ for 5 minutes and then cooled to 70 $^{\circ}\text{C}$. Untreated glass slides were dipped into the gel after which the slides were allowed to dry at room temperature. Glass slides were stored in a closed beaker and were used for up to a week after preparation.

Biotin-BSA coating. A flow cell was created using techniques described in Fig. 2.3. The flow cell was filled with 25 μl biotin-labeled albumin (biotin-BSA, Sigma, 2.5 mg/ml in pH 5.2 sodium acetate buffer). Volumes in excess of the flow cell volume ($\approx 10 \mu\text{l}$) were used to make sure that the complete flow cell was filled or flushed. Biotin-BSA worked as a linking agent for streptavidin. All protein containing solutions introduced into the flow cell were allowed to settle for at least 5 minutes before a new solution was introduced. The biotin-BSA coated the surface of the cover slip. At neutral pH BSA is slightly negatively charged just as the glass surface. By choosing the pH of the solution close to the iso-electric point of BSA the electrostatic repulsion is lowered and the coating should be more effective.

Chapter 2

Streptavidin coating. The flow cell was flushed with 50 μl MRB80 and filled with 1 mg/ml streptavidin in MRB80, which bound to the biotin-BSA layer. Some of the four biotin binding pockets remained vacant and were used to bind biotin labeled seeds in the next step. We also tried a direct linkage of the streptavidin to the surface but the binding of seeds was less reproducible. Because the bond between biotin-BSA and streptavidin has some rotational freedom the streptavidin was able to effectively adapt to the biotin locations on the seeds, that are introduced next. Indirect linkage of microtubules with biotin-BSA was described earlier [64].

Binding of seeds. Next, the flow cell was flushed again with 50 μl MRB80 and filled with seeds diluted in MRB80 (50 fold dilution from stock).

Introduction of tubulin. The cell was flushed for the last time with 50 μl MRB80 to remove unbound seeds. Then a solution containing free tubulin in MRB80 was introduced containing 1 mM GTP and 10 mg/ml non-labeled BSA. BSA was used to compete with tubulin for possible non-specific binding to surfaces. Non-specific binding could lower the free tubulin concentration and would have made the experiments less reproducible. An oxygen scavenging system was added in some cases (4 mM dithiothreitol / DTT, 0.2 mg/ml catalase, 0.4 mg/ml glucose-oxydase and 50 mM glucose). These chemicals consume oxygen while oxidising glucose. Especially free radicals of oxygen have a damaging effect on proteins. The tubulin concentration was varied between 7.2 and 28 μM .

Closure of the sample cell. The tubulin was allowed to settle for 1 minute before the metal wires were removed from the flow cell and pressure was applied for several minutes to adjust the sample thickness to the height of the barriers. Then finally, hot candle wax is deposited along the open sides of the flow cell using a glass pipette. The wax quickly solidifies and prevents evaporation of liquid which otherwise causes currents of fluid in the sample.

2.5 Microscopy and image analysis

Samples were observed with an inverted microscope equipped with DIC optics (Leica, DM IRB/E) and a 100 \times oil-immersion objective (numerical aperture 1.3). Samples were illuminated with a 100 W mercury lamp through an oil-immersed objective. A sleeve was constructed around the objective lens that could be heated or cooled by thermoelectric coolers (Melcor). Excess heat was removed by a connected heat sink that was cooled with water of 20 $^{\circ}\text{C}$. The temperature of the sample was linked to the temperature-controlled objective lens by the immersion oil and the thin cover slip. During sample observations the temperature in the sample was controlled to 23 $^{\circ}\text{C}$, which was calibrated using a dummy sample with a 25 μm thick thermocouple inserted. The DIC-technique is direction sensitive, i.e. the observed contrast depends on the direction of the gradient in index of

Experimental set-up and data analysis

refraction. Samples were rotated such that the barriers generated a minimum contrast while microtubules growing perpendicular towards it were imaged best.

The image acquisition system used for recording microscope images of microtubules consisted of a CCD camera (Kappa, CF8/1), image processor (Argus 20, Hamamatsu), video recorder and computer workstation (SGI, visual). The image processor adjusted the contrast and brightness of the stream of images coming from the CCD camera. Only after this video enhancement microtubules became clearly visible. In addition, the image processor subtracted a stored out-of-focus image from every new image. On this image, no microtubules or other sample details were visible and only the average intensity distribution over the recorded area was reproduced. The subtraction of this image made an increased contrast enhancement possible and corrected for camera and illumination imperfections. During an experiment, the video recorder recorded images at a rate of 25 frames per second while a frame grabber inside the workstation acquired digitised images at a maximum rate of 2 fps. Later digital images at a rate up to 25 fps could be acquired from the video tape offline. Video taping always caused some image deterioration, which was prevented by using online acquisition. This had the added advantage that digitised images were directly accessible after an experiment was performed. Acquired images contain 720 by 576 pixels, each covering 50 by 50 nm ($100 \times$ objective) and having 256 grey values.

Markers were placed on the acquired images to quantify the shape of the observed microtubules. A straightforward but painstaking way would have been to use a computer mouse to place markers on the microtubule. Because of the large amount of images that needed to be analysed, we made an effort to semi-automate this process using computer code written and run in IDL (RSI, Boulder, CO).

Fig. 2.4a shows an example of an acquired image of a microtubule. The intensity variation of the pixels in a pixel column is plotted in Fig 2.4b. Although by eye the location of the microtubule could be easily assigned to pixel number 139, it is hard to judge the location from the intensity plot. The DIC technique seems to cast a shadow onto the microtubule. Going from bottom to top the pixel intensity first becomes darker and then lighter in the vicinity of the microtubule. We simulated this intensity profile by a single period of a sinus with a width of 13 pixels as depicted in Fig. 2.4c. Next we performed a convolution of this shape with the intensity profile of Fig. 2.4a. The resulting curve clearly peaks around the correct pixel value of 139 (see Fig 2.4d). As a consequence of intensity noise and neighbouring objects such as dirt particles or other microtubules, the intensity profile can be distorted and the maximum in the convoluted curve does not always correspond to the true microtubule location. An algorithm which assigned a value for the microtubule location for every pixel column of pixels, was designed to cope with these difficulties.

Chapter 2

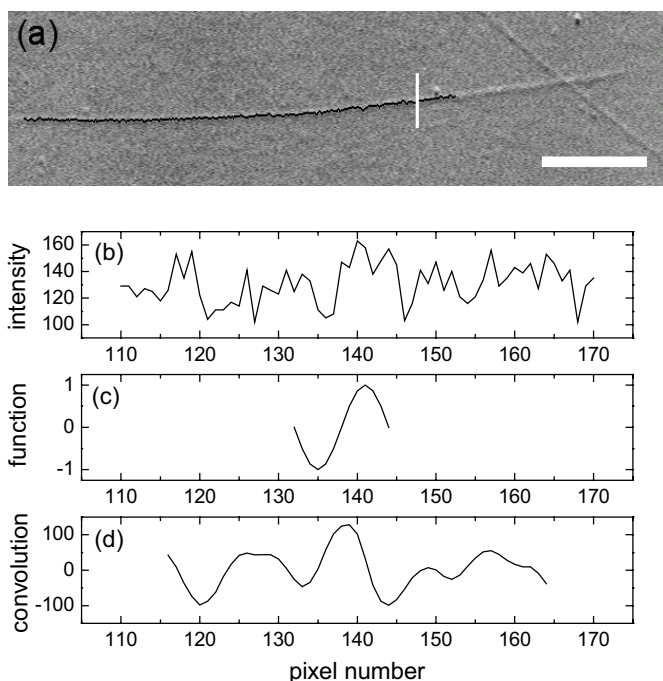


Figure 2.4 Methods used for quantifying microtubule shapes. **(a)** An acquired image of a microtubule. The horizontal scale bar equals 100 pixels or roughly 5 μm . The black line indicates locations found by a semi-automatic tracing algorithm, which was stopped halfway the microtubule to show the underlying microtubule. **(b)** The intensity of the pixels in the pixel column indicated by the vertical white line in Fig. 2.4a plotted versus the vertical pixel number. The origin of Fig. 2.4a coincides with the lower left corner. **(c)** The single period of a sine function used to model the characteristic shadow-like image of the microtubule. **(d)** The result of convolution of the raw data of Fig. 2.4b and the sine period.

This algorithm traced the microtubule from left to right. First a starting point was selected manually. The next pixel column, one pixel to the right, was convoluted and the maximum was assigned as the position of the microtubule. After enough points were obtained in this way, 40 preceding values could be used to extrapolate the most likely location of the microtubule in the next column. When the value found by convolution deviated a lot from the extrapolated value, then the convoluted value was most likely wrong and the extrapolated value was assigned. Using this trick, dirt particles or crossing microtubules had little effect on the assigned values. Large particles or microtubules that run almost in parallel caused failure of the algorithm. The allowed distance between extrapolated and convoluted value was usually chosen equal to five. This value and the length of the extrapolation region were varied to adjust the algorithm to highly curved microtubules or noisy images. The algorithm worked in most cases where the complete length of the microtubule was within the focal depth of the microscope.

Experimental set-up and data analysis

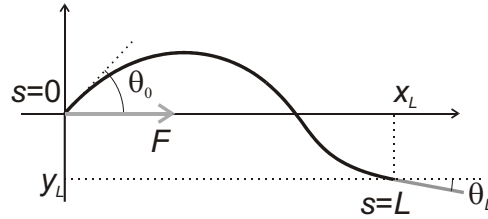


Figure 2.5 Coordinate system used to model a microtubule. The origin coincides with a hinged point where a force (grey arrow) is applied. The x -axis was chosen along the direction of the force. The location of the clamp relative to the chosen coordinate system equals $[x_L, y_L]$. The microtubule is completely described by the tangent angle θ as a function of the path length s , which equals zero at the origin. Angles at the hinged point and clamped end are referred to as θ_0 and θ_L respectively.

2.6 Theory of buckling

The shape of a buckled microtubule as observed in the experiments reported in chapter 3 and 4, contains information about the force that is being applied by the barrier on the microtubule tip. Here we outline the equations that link the shape to the magnitude of the force and which will be used in the next section for fitting experimentally observed shapes. We will assume that the microtubule can be simplified as a homogeneous rod with bending rigidity κ . In chapters 3 and 5 methods will be described to measure the rigidity of microtubules. Here we treat κ simply as a constant. Simplifying a microtubule as a homogeneous rod is allowed if the radius of curvature, R , is much greater than the diameter of the microtubule [64].

In order to calculate the shape of a buckled rod we need to set boundary conditions at both ends. A buckled microtubule is assumed to be free to pivot on the point of barrier contact. In other words, no external bending moments are applied on this hinged end. The other side of the rod is assumed to be clamped in a fixed direction, which models a microtubule seed that is rigidly fixed to the surface. For these boundary conditions we will show that there is only one free parameter that fixes the shape of a buckled rod. When the direction of the force applied to the hinged end is fixed then both the magnitude of the force and the length of the rod are known.

In Fig. 2.5 a buckled rod is drawn to which a force is applied at a hinged end while the other end is clamped. A coordinate system is chosen such the the x -axis is in the direction of the applied force. The path length s along the rod is chosen to be zero at the hinged end and the shape of the microtubule can be completely specified by the tangent angle θ as a function of s . The direction of the y -axis is chosen such that θ_0 , i.e. the angle at $s = 0$, is positive. We can now specify the boundary conditions [65]. At the hinged end these are $x = 0$, $y = 0$ and $d\theta/ds = 0$, which satisfies zero bending moment and at the

Chapter 2

clamped end we have $x = x_L$, $y = y_L$, $\theta = \theta_L$ and $s = L$. The length L is thus taken as the path length until the point where the rod becomes clamped.

We apply the laws of linear elasticity theory [65,66] to calculate the shape of a buckled rod. Everywhere along the rod, the bending moment M is linked to the local curvature by

$$M(s) = \frac{\kappa}{R(s)} = \kappa \frac{d\theta}{ds}. \quad (2.1)$$

The sum of the bending moment and the moment exerted by the force at the hinged end should equal zero at any point of the rod. This balance is given by

$$Fy(s) + \kappa \frac{d\theta}{ds} = 0. \quad (2.2)$$

Differentiating with respect to s gives a convenient expression called the beam equation:

$$\frac{d^2\theta}{ds^2} = -\frac{F}{\kappa} \sin \theta = -\beta^2 \sin \theta, \quad (2.3)$$

where we introduced β^2 as a normalised force. This equation can be solved as follows [64,65]. A single integration step over s yields

$$\frac{1}{2} \left(\frac{d\theta}{ds} \right)^2 = \beta^2 \cos \theta - \beta^2 \cos \theta_0. \quad (2.4)$$

We can write Eq. 2.4 in a convenient way by doing a coordinate transformation. Therefore, we define a new coordinate φ by the following set of equations:

$$k \sin \varphi = \sin \frac{1}{2} \theta, \quad (2.5a)$$

$$\varphi_{s=0} = \varphi_0 = \frac{\pi}{2}. \quad (2.5b)$$

Eq. 2.4 can now be rewritten as

$$\frac{ds}{d\varphi} = \beta \frac{1}{\sqrt{1 - k^2 \sin^2 \varphi}}. \quad (2.6)$$

Expressions for s , x and y as a function of φ in terms of elliptic and goniometric functions can now be calculated. Integration of Eq. 2.6 gives

Experimental set-up and data analysis

$$s = \beta \left(H(\varphi, k) - H\left(\frac{\pi}{2}, k\right) \right), \quad (2.7)$$

where H is the Legendre elliptic integral of the 1st kind [67]. The y -coordinate can be calculated by combining Eq. 2.2, 2.4 and 2.5:

$$y = -2 \frac{k}{\beta} \cos \varphi. \quad (2.8)$$

To obtaining x , we use

$$\frac{dx}{d\varphi} = \frac{dx}{ds} \frac{ds}{d\varphi} = \frac{ds}{d\varphi} \cos \theta. \quad (2.9)$$

Integration combined with substitution of Eq. 2.6 yields

$$x = \beta \left[2E(\varphi, k) - 2E\left(\frac{\pi}{2}, k\right) - H(\varphi, k) + H\left(\frac{\pi}{2}, k\right) \right]. \quad (2.10)$$

E is the Legendre elliptic integral of the 2nd kind. The Legendre elliptic integrals are well tabulated [67] or can be calculated using numerical methods [68].

We can simplify Eq. 2.10 in order to get an intuitive feeling for the shape of a buckled rod. For small amplitudes of buckling, Eq. 2.10 can be approximated by,

$$\varphi = \beta x + \frac{\pi}{2}. \quad (2.11)$$

We may therefore interpret φ as a scaled and shifted version of x . Substitution of Eq. 2.11 in Eq. 2.8 shows that the shape of a buckled rod is very well approximated by a sine function, which is also apparent from calculated buckling curves (e.g. Fig. 2.6).

We now need to solve the equations for x and y using the set of boundary conditions. The equations can be written most easily in terms of φ_L , i.e. the value of φ at the clamped end. We write,

$$\frac{y_L}{x_L} = \frac{-2k \cos \varphi_L}{2E(\varphi_L, k) - 2E\left(\frac{\pi}{2}, k\right) - H(\varphi_L, k) + H\left(\frac{\pi}{2}, k\right)}, \quad (2.12a)$$

where k is given by,

$$k = \frac{\sin \frac{1}{2} \theta_L}{\sin \varphi_L}, \quad (2.12b)$$

Eq. 2.12a can be solved numerically for φ_L . For a buckled rod φ_L will be between 1.5π and 2π . In practice the following procedure should be used to calculate the curve of a buckled

Chapter 2

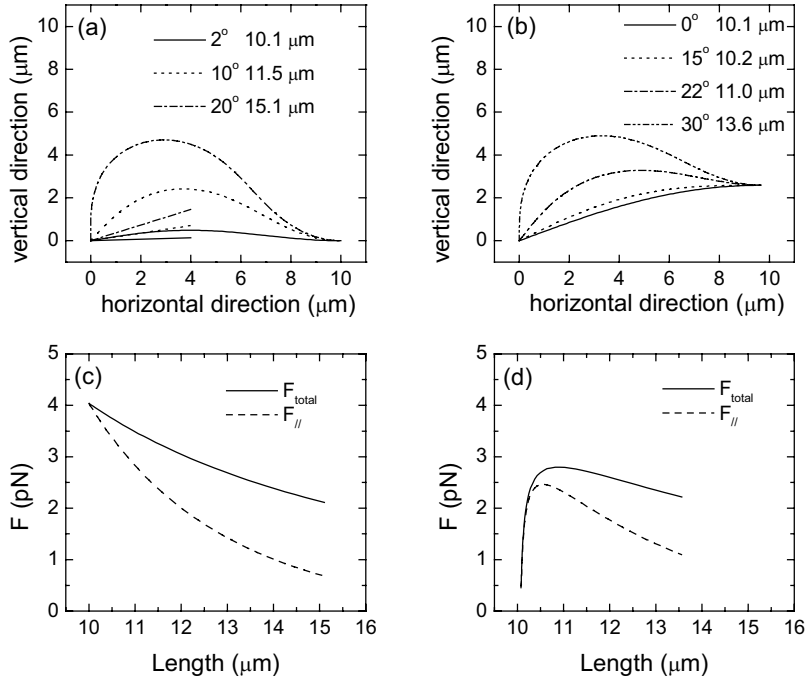


Figure 2.6 Calculation of curves of buckled rods and corresponding forces using $\kappa = 20 \text{ pN}\mu\text{m}^2$, which is a reasonable value for the rigidity of a microtubule (see chapter 5). The distance between the clamp and the pivot point is $10 \mu\text{m}$. **(a)** Curves for a geometry where the pivot point is in line with the horizontal direction of seed clamping. Curves are plotted for three indicated (numerically and as small lines) angles of the force. The angle is relative to the horizontal. The length of each curve is indicated in the legend. **(b)** Similar curves but now for a pivot point that is shifted $2.6 \mu\text{m}$ downward relative to the horizontal clamp. **(c)** Total and tangent force components as a function of rod length for the geometry depicted in Fig. 2.7a. **(d)** Similar plot for the shifted geometry of Fig. 2.7b.

microtubule. Pick a direction for the applied force and construct a coordinate system along this direction. Knowing the location of the seed, calculate its coordinates, x_L and y_L in the new coordinate system. Then using Eq. 2.12 calculate both φ_L and k . The corresponding length and normalised force β can be calculated using Eq. 2.7 and 2.8 respectively with $\varphi = \varphi_L$ substituted. The physically important parameters force and length are thus unambiguously linked to the direction of the force. With the chosen boundary conditions the system has only one free parameter.

For our purposes it is interesting to know the force component tangent to the filament direction, θ_θ , at the free end, which is given by

Experimental set-up and data analysis

$$F_{\parallel} = \kappa\beta^2 (1 - 2k^2). \quad (2.13)$$

It is the tangent force component that it is expected to effect microtubule growth for a buckling microtubule.

Using the methods described we calculated the forces involved in buckling for two geometrically different situations (see Fig. 2.6a and b). In both geometries the direction of clamping is horizontal and the straight distance until the pivot point is 10 μm . In the first situation the pivot point lies exactly in the direction of clamping, whereas in the second situation the pivot point is shifted downwards. Calculated curves are shown for several directions of the applied force. Note that the coordinate system is fixed and not rotated. The magnitude of the force and its tangent component are plotted as a function of the microtubule length in Fig. 2.6c and d. In the straight configuration the force is maximal when the rod has just started buckling and the force only goes down when the length is increased. This behaviour is a bit counterintuitive but can be tested with for example a plastic ruler. One needs less force to buckle a 40 cm long ruler to a length of 30 cm than one needs to initiate buckling of a 30 cm long ruler. A simple equation exists for the force that is needed to initiate buckling in a clamped configuration [65]:

$$F_c = \frac{20.19\kappa}{L^2}. \quad (2.14)$$

This force is known as the critical buckling force and was first calculated by Euler. There exists no critical force when the pivot point is shifted as in Fig 2.6b. Furthermore the maximum in the force curve is considerably lower compared to F_c for a straight configuration with the same distance between seed and pivot point. In such a shifted configuration a microtubule can thus more easily initiate buckling by force generation.

2.7 Curve fitting

In the previous section we outlined the equations that describe the shape of a buckled rod. In the experiments described in chapter 3 and 4 buckling is observed on microtubules. Fitting the theoretical shape to the observed buckling makes a force measurement possible if the rigidity of a microtubule is known. The methods used for fitting are described here.

Fit procedure

An example of a buckled microtubule is shown in Fig. 2.7. First the microtubule was traced using methods that are described in section 2.5. The trace was subdivided into 29 equally sized segments of which average x and y coordinates were calculated resulting in 29 marker points. A typical sequence of images consists out of a few tens of images and begins when the microtubule has just started buckling and ends with a clearly curved microtubule. To all images in the sequence 29 marker points were assigned. Points were

Chapter 2

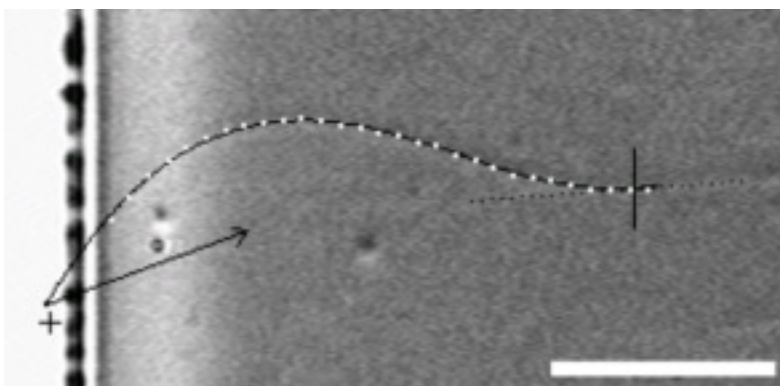


Figure 2.7 Curve fitting to a buckled microtubule. The barrier is on the left. Scale bar is 5 μm . Overlaid over the microtubule are 29 marker points (white dots) and a calculated theoretical curve (Eq. 2.8 and 2.10). During fitting the transition point between clamped and free microtubule was shifted along the dotted line that coincides with the direction of the seed. The vertical black line indicates the transition point found by fitting. The black cross on the left is the location of the initially manual assigned pivot point. The beginning of the arrow denotes the pivot location found by fitting and the arrow direction indicates the direction of the fitted force.

located by hand if the tracing algorithm failed and images were disregarded if the microtubule was not visible over its complete length.

We assumed that the seed that nucleated the microtubule is completely immobilised and does not rotate during buckling. This assumption will be tested experimentally (chapters 3 and 5). The pivot point, i.e. the point of interaction between microtubule and barrier, was obscured by the overhang and was guessed initially. A second important point is the transition point on the seed where the clamped part stops and the free microtubule begins. This transition point is somewhere on a line that coincides with the direction of the seed (see Fig. 2.7). An initial location of the transition point was guessed on this line. With the pivot and transition points picked we now performed a one parameter fit to every microtubule in the sequence. The direction of the force was varied and for every marker point the distance to the theoretical curve given by Eq. 2.8 and 2.10 was calculated. The sum of squared distances for all 29 points was minimised. Next the pivot point was adjusted and the transition point was shifted along the indicated line (in total three fit parameters) after which all microtubule shapes were fitted again. For every set of pivot and transition points the total sum of all squared distances for all microtubules in a sequence was calculated. The points obtained by minimisation of this sum were assumed to be the exact pivot and transition point. For these points the length of each microtubule and the force applied at the pivot point were estimated from the fitting. For minimisation

Experimental set-up and data analysis

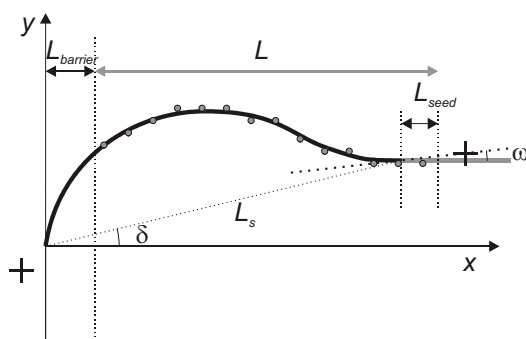


Figure 2.8 Quantities used to describe the geometry of a fit algorithm test. For a given geometry and force a theoretical curve was calculated represented by the thick black line. The clamped part of the microtubule is indicated by the grey thick line. The direction of clamping was horizontal and the location of the clamp relative to the pivot point is given by the angle δ and the distance L_s . In the experimental system a certain part of the microtubule, equal to $L_{barrier}$, which is underneath the overhang, can not be observed. Locations of 25 marker points (grey dots of which only a few are represented) were chosen along a distance L , which includes part of the seed (L_{seed}). Noise was added to the location of the marker points in the y -direction representing experimental noise. A fitting algorithm was started with a pivot point and seed transition point (black crosses) offset from the exact values. The transition point was shifted along a straight line, which crosses the exact transition point at a non-horizontal angle, ω , that was varied to represent an uncertainty in the direction of the seed.

we used Brent's method with parabolic interpolation for one parameter fitting and the downhill simplex or Amoeba method for three parameter fitting [68].

Fit errors

In order to test the accuracy by which the pivot and transition points were found, we tested the fitting algorithm by simulations for a given geometry a series of buckling curves using the equations outlined in the previous section. These series were fitted to observe how well these points were reconstructed by the algorithm. We started each series with an almost straight microtubule and stopped when the microtubule length was increased by a certain value ΔL . The angle of the force was increased in discrete steps in order to increase length. Of all curves a distance $L_{barrier}$ (see Fig. 2.8) equal to $1.5 \mu\text{m}$ was removed to represent the overhang and $1 \mu\text{m}$ (L_{seed}) was added for the seed. The resulting curve was segmented to give 25 marker points, to which noise with a *rms*-value of 50 nm was added to mimic experimental noise. The initial pivot and transition points that were used to initiate the fit algorithm were offset from the exact points as well. The initial x and y -displacement of the pivot point were sampled randomly out of a normal distribution with a *rms*-value of $0.5 \mu\text{m}$. The transition point was shifted randomly (*rms*-value $0.5 \mu\text{m}$) along a line slightly offset from the horizontal (*rms*-value 1.5 degrees), which mimics

Chapter 2

Number	L_s (μm)	δ (degrees)	Series size	$\Delta L/L_s$ (%)	$\Delta L_s = L_s' - L_s$ (μm)	$(F_{//fit} - F_{//})/F_{//}$ (%)	$(v_{fit} - v)/v$ (%)
1	7	0	10	2.6	-0.36 \pm 0.21	9.9 \pm 5.4	2 \pm 18
2	7	0	25	13	-0.14 \pm 0.04	5.8 \pm 1.4	0.5 \pm 4.5
3	7	20	11	2.8	0.58 \pm 1.19	-3 \pm 26	-9.4 \pm 5.5
4	15	0	11	3.0	-0.28 \pm 0.40	1.6 \pm 2.9	-0.3 \pm 3.1
5	15	20	12	3.2	-0.03 \pm 0.40	3.5 \pm 4.8	1.3 \pm 2.1

Table 2.1 Fit results of simulated buckling microtubules. The data were obtained by averaging over eight fits. The number of buckle curves in every series is given as series size. Averages and *rms*-values are shown. Note that the rms-value is often larger than the average so that both numbers together give the total fit error. The parameter δ is explained in Fig. 2.8.

uncertainty in the direction and location of the transition point. Five different series for different geometries were fitted. Each series was fitted eight times with different starting points to obtain statistics on the errors made (see Table 2.1).

For all series we calculated the straight distance, L_s' , between the fitted pivot point and the transition point and from each microtubule in a series we obtained the length and tangent force component. For the simulated data we assumed that the growth velocity of a microtubule is exponentially dependent on force, which is expected on theoretical grounds (see chapter 1). We were then able to calculate an average growth velocity, v_{fit} , and average tangent force, $F_{//fit}$, for every fitted series, which could be compared with the data that was used as input, v and $F_{//}$ (Table 2.1).

The following picture arose from our simulations of the fit algorithm. A large relative length increase during buckling, $\Delta L/L_s$, gave large amplitudes of buckling for which an accurate fitting was possible. The error made in the distance between pivot point and transition point, ΔL_s , for a 13 % increase was on the order of $\pm 0.2 \mu\text{m}$. For a smaller length increase of around 3%, ΔL_s equaled $\pm 0.5 \mu\text{m}$. Large errors were made for short (7 μm) microtubules that had a pivot point that was not in line with the seed ($\delta = 20^\circ$), but offsets that were observed in the experiments were smaller than 20° and most of them were around zero. On the basis of these observations we came to a rule-of-thumb for the errors made in different geometries. For $\Delta L/L_s > 5\%$, we take $\Delta L_s = \pm 0.25 \mu\text{m}$ and for $\Delta L/L_s < 5\%$, we take $\Delta L_s = \pm 0.5 \mu\text{m}$. Although this rule is based on a limited number of simulations it allows to distinguish between geometries with high and low error risks.

In general, for a given geometry, the force scales with L_s as L_s^{-2} . Eq. 2.14 describes this relation for a geometry in which the pivot point is in line with the seed. Therefore an error in L_s translates to an error in the average force following:

Experimental set-up and data analysis

$$\frac{\Delta F}{F} = -2 \frac{\Delta L_s}{L_s} \quad (2.15)$$

This equation will be used in chapter 4 to calculate experimental errors. Fit errors made in the determination of the average velocity during buckling are on the order of 10% with the largest errors made on short microtubules ($L_s = 7 \mu\text{m}$).

2.8 Acknowledgements

I would like to thank Marco Konijnenburg for the development of the image acquisition system, Maurice van de Boer for his assistance in the construction of barriers on cover slips, Tim Mitchison for kindly providing GMPCPP and Nanne Nanninga and his lab members for their help with tubulin preparations.

III

The effect of force on microtubule growth velocity

Living cells employ forces generated by microtubule assembly to move cellular organelles. In this chapter we describe an experiment that allows quantitative measurement of these forces in an in-vitro model system. Microtubules were observed to generate piconewton forces that were large enough to buckle themselves in between barriers. Both the growth velocity and catastrophe probability were changed by the opposing elastic-restoring-force created by the buckled microtubules. Here we analyse the decreased growth velocity as a function of force relative to the initial growth velocity. We show that the relative decrease is independent of the initial growth velocity. This observation suggests that the largest effect of force is on the on-rate of microtubule assembly. The observed forces are large enough to perform useful work inside living cells.

3.1 Introduction

Numerous *in vivo* experiments suggest that growing microtubules are able to generate pushing forces. These forces are likely to be employed by living cells to perform cellular functions. Examples are the centring of cell nuclei and the positioning of chromosomes before cell division [29,42]. Other biopolymers like actin are also believed to generate force by assembly for example during the propulsion of the bacteria *Listeria monocytogenes* and *Shigella flexneri* [38].

Forces generated by filament assembly are difficult to assess quantitatively inside living cells because appropriate force probes are difficult to introduce. Quantitative force measurements on single biopolymers were only performed on microtubules grown from purified tubulin which were made to push against artificial glass barriers [47,54]. Microtubules are a good model system for studying assembly forces because of their large

Chapter 3

rigidity. Experimentally it is very difficult to apply a compressive force on a floppy filament like actin. In the experiment described by Dogterom and Yurke [47] microtubules grown from surface-connected nucleation sites struck micro-fabricated barriers after which they were observed to buckle. Forces generated were inferred from the curvature of the buckled microtubules, while at the same time microtubule growth velocity was measured. The velocity was seen to decrease with increasing force with a rate faster than predicted by a simple energy calculation. The largest forces observed were around 4 pN, comparable to forces generated by motor proteins of which it is generally accepted that they do important work in living cells. The relation between velocity and force was measured for only one experimental condition at which free microtubules grew at 1.2 $\mu\text{m}/\text{min}$. *In vivo* microtubules can grow at much faster rates of up to 20 $\mu\text{m}/\text{min}$ and therefore it is important to study forces generated at larger initial growth velocities and test whether the force-velocity relation at different velocities can be described by a similar mechanism.

In the experiments described in this chapter we measured assembly forces at different concentrations of free tubulin which changed the rate at which microtubules grew towards the barriers. The data will be shown to be consistent with earlier work. We will compare our data with different existing ideas about how microtubule growth proceeds at a molecular level. There does not exist an accurate picture of how new subunits add to the tip of a growing microtubule and how microtubules occasionally switch from growth to shrinkage. New types of experiments, like the one described here, are necessary to come to a good description of microtubule dynamics. Knowledge about the tip structure is for example important to shed light on the working mechanism of proteins that control microtubule dynamics inside living cells by acting on the tip of growing microtubules (see discussion in chapter 6).

3.2 Materials and methods

The experiments described here are mostly done using experimental techniques that are described in chapter 2. In short, microtubules were grown from short GMPCPP-stabilised, biotin-labeled, microtubules (seeds) attached to a streptavidin-coated cover slip. Cover slips with micro fabricated barriers on top were used in order to confine the microtubules. A flow cell was constructed from a glass slide and the cover slip, which allowed the proceeding of all necessary steps for the binding of the nucleation sites. Forces and lengths of buckling microtubules were analysed using the fit procedure described in chapter 2.

Experimental conditions. Before the flow cell was closed, free tubulin (Cytoskeleton, Denver, CO) in MRB80 plus 1 mM GTP and 10 mg/ml non-labeled BSA, was flown into the cell. Buckling experiments were performed using two different tubulin concentrations (C_T), 20 and 28 μM , and a constant sample temperature of 23°C. The oil immersion objective (100 \times , numerical aperture 1.3) used for imaging was thermostated to

The effect of force on microtubule growth velocity

control the temperature. An oxygen scavenging system consisting of 4 mM DTT, 0.2 mg/ml catalase, 0.4 mg/ml glucose-oxylase and 50 mM glucose was used only in the experiments done at $C_T = 20 \mu\text{M}$. Only at a later stage of the experiments we started using this oxygen scavenging system because it helps to stabilise the proteins used and prolongs the lifetime of a sample by preventing the formation of free radicals.

Growth velocity measurements on free microtubules. Growth velocities of microtubules growing from nucleation sites were analysed before they reached the barriers. Microtubules were selected of which free growth could be observed for several minutes. Using analysis software written in IDL (RSI, Boulder, CO) we measured the straight distance from a fixed point on the microtubule seed to the observed location of the tip approximately every 10 seconds using digitised images taken during the experiment. The velocity of each event was obtained by performing a linear fit to the length data as a function of time. For each tubulin concentration the weighted average and standard deviation of the velocity was estimated. The duration of each individual event was used as weight.

Rigidity analysis. Microtubule flexural rigidity was measured in order to calibrate the force measurements done on buckling microtubules. The thermal fluctuations of free-growing microtubules nucleated from surface-connected seeds were analysed in the same samples as used for the force-generation experiment. First, the transition point between seed and free microtubule was estimated. Thermal fluctuations stop at the seed. Fluctuations and therefore the transition point, could be best observed by looking at the real time microscope images at 25 frames/s. Microtubules with an initial length, L , between 5 and 18 μm were analysed. The position of a point on the microtubule with distance L to the seed was scored every 2 seconds as the microtubule grew. The deflection d was calculated as the distance relative to the average location of the analysed point. The persistence length, L_p , was calculated using (see chapter 5)

$$L_p = \frac{L^3}{3 \text{var}(d)}. \quad (3.1)$$

The flexural rigidity κ is given by $k_B T L_p$, where k_B equals Boltzmann's constant and T equals the absolute temperature. The relative error in the rigidity measurement is taken as

$$\frac{\Delta\kappa}{\kappa} = \sqrt{\frac{2}{M-1}} + 3 \frac{\Delta L}{L}, \quad (3.2)$$

where the first part represents the error caused by an uncertainty in the estimation of a variance based on M samples (see chapter 5). The second part is the error introduced by an uncertainty ΔL in the estimation of the seed transition point which over- or under-estimates the length L of the free microtubule. ΔL was taken equal to 0.5 μm .

Chapter 3

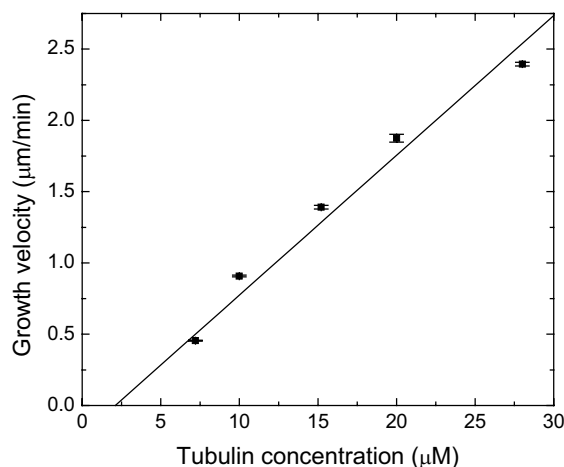


Figure 3.1 Average growth velocity of the plus end of growing microtubules as a function of tubulin concentration. An oxygen scavenging system was added to all samples except for measurements made at 28 μM and some of the 10 μM samples (see text). A linear fit to the data, weighted with the indicated standard error of the mean is plotted as a straight line.

Standard errors or standard deviations. In this chapter we present data on growth velocities and forces of individual microtubules. Standard deviations were calculated to indicate errors on individual events. In the discussion on the average behaviour of many microtubules standard errors of the mean were used.

3.3 Results

Free microtubules

The free growth of microtubules nucleated by the surface-connected seeds characterised first. Later, data on microtubule growth under force was compared with data taken under these zero force conditions. The seeds were observed to nucleate microtubules on both sides. Free microtubules were observed to randomly switch to a state of rapid disassembly, i.e. a catastrophe. Catastrophes occurred more frequently at low tubulin concentrations. Rescues were not observed apart from new nucleation at the stabilised seeds. Growth velocities of microtubule plus ends were measured at five different tubulin concentrations, C_T . The assignment of plus and minus ends was made on the basis of the growth velocity. Plus ends grow on average twice as fast as minus ends [19]. All measurements were made on samples with barriers. The measurement of free growth was stopped when a microtubule reached a barrier. Measurements at $C_T = 20$ and 28 μM were made in the same samples in which microtubule force generation was studied. For $C_T = 7.2, 10$ and

The effect of force on microtubule growth velocity

15.2 μM separate samples were made to measure free growth velocity. The effect of the addition of an oxygen scavenging system on the growth velocity was checked for $C_T = 10 \mu\text{M}$. The measured velocity was $0.88 \pm 0.01 \mu\text{m}/\text{min}$ (average \pm standard error of the mean (SEM)) with the addition and $0.96 \pm 0.02 \mu\text{m}/\text{min}$ without. Because systematic errors like inaccuracies made when pipetting solutions add to the statistical error it was concluded that the addition does not significantly change growth velocities. Velocities are plotted in Fig. 3.1 as a function of concentration. The velocity is expected to depend linearly on the concentration following Eq. 1.3. Using linear regression we found a value for the critical concentration, $C_C = 2.1 \pm 1.3 \mu\text{M}$, for which the rate of tubulin association equals the rate of dissociation. At 5.2 μM microtubule growth was not observed probably because microtubule nucleation from seeds becomes slow [11] and frequent catastrophes [11,19,55] limit the maximum lengths of microtubules severely at low concentrations making it difficult to detect growth. At 28 μM some microtubules were observed that were not connected to surface-attached seeds but were probably created by self-nucleation of microtubules [11]. Large amounts of microtubules cause imaging problems and a severe depletion of the pool of free tubulin.

Buckled and stalled microtubules

To prevent problems caused by excessive self-nucleation we choose 28 μM , for which the average velocity was $2.40 \pm 0.01 \mu\text{m}/\text{min}$ (mean \pm SEM), as starting point for buckling experiments. At this concentration microtubules often grew longer than 20 μm before experiencing a catastrophe (see chapter 4) and most microtubules that grew in a direction more or less perpendicular to the barriers made it to the barriers (Fig. 3.2). Some microtubules were observed to grow over the barriers after which observation was stopped, while others were confined by the ridge that forms the overhang of the barriers. For these last microtubules force generation could be studied. In general, microtubules that were seeded more than approximately 5 μm away from the barriers were seen to continue elongation after they contacted the barrier. Microtubules were seen to bend in two ways to facilitate growth; sliding and buckling. If the microtubule tip slides along the barrier only small forces, of little interest, oppose growth. Often, however, the tip started pivoting around a local barrier irregularity and the point of barrier interaction remained constant for a while. In these cases, microtubules build up compression force and start to buckle (Fig. 3.2), initially generating force equal to the critical buckling force. A period of buckling terminated in different ways. Sometimes, the microtubule lost its point of contact and the microtubule started sliding along the barrier (Fig. 3.2a). Occasionally, a buckling microtubule switched to a phase of rapid shrinkage (Fig. 3.2b), a phenomenon that we refer to as a catastrophe under load and which is analysed in detail in chapter 4.

Chapter 3

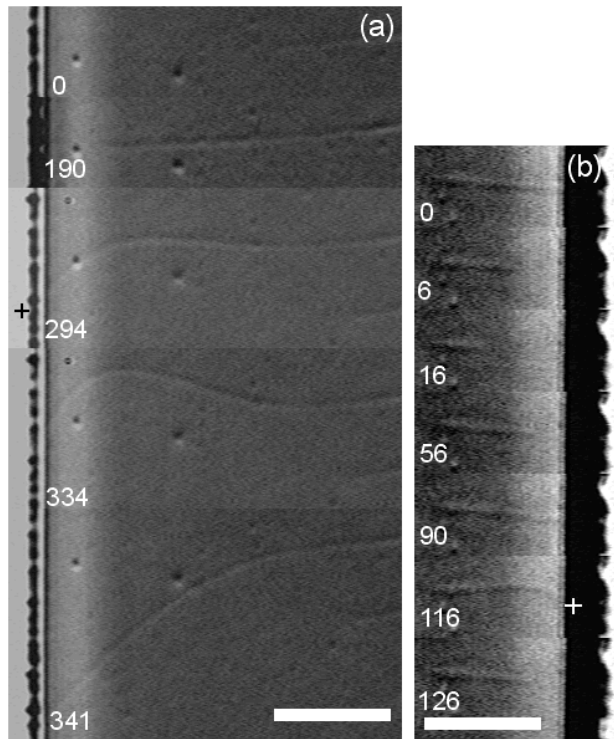


Figure 3.2 Examples of buckling microtubules. **(a)** Growth, buckling and sliding of a relatively long microtubule at $C_T = 28 \mu\text{M}$. The barrier is at the left and the seed at the right side of the pictures. Images show: a microtubule about a minute after nucleation from the seed ($t = 0$ s), the microtubule after substantial free growth ($t = 190$ s), the microtubule during buckling ($t = 294$ s), the moment just before the microtubule starts sliding along the barrier ($t = 334$ s) and the shape observed after sliding ($t = 341$ s). The point of barrier interaction found by fitting is indicated in one of the frames as a black cross. The part of the microtubule underneath the overhang could not be observed. Scale bar = $5 \mu\text{m}$. **(b)** Subsequent growth events nucleated by a seed close to the barrier at $C_T = 28 \mu\text{M}$. A microtubule is shown while it is: just before switching to rapid shrinkage after having pushed for 24 seconds without apparent buckling ($t = 0$ s), shortening ($t = 6$ s), disassembled all the way back to the seed ($t = 16$ s), regrowing ($t = 56$ s), just before the initiation of buckling ($t = 90$ s), at its maximum buckle amplitude ($t = 116$ s) and again shrinking ($t = 126$ s). The point of barrier-contact found by fitting is shown as a white cross. Scale bar = $5 \mu\text{m}$. The image intensity fluctuations seen on the barriers do not represent the end of the etched overhang, but are caused by barriers with a non rectangular cross-section (see Fig. 2.2g and h).

The effect of force on microtubule growth velocity

Many microtubules that were seeded approximately 5 μm away from the barriers were observed to neither buckle nor slide after reaching the barriers (Fig. 3.2b). A catastrophe under load occurred on average 24 seconds after initiation of barrier-contact. In chapter 4 these microtubules are studied in detail and it is shown that if these microtubules are growing during barrier-contact, the growth rate is lower than 0.05 $\mu\text{m}/\text{min}$. Microtubules that are grown from a seed located close to the barrier (Fig. 3.2b) need to generate large forces in order to buckle (see Eq. 2.14). Frequent catastrophes limited the observation time of growth under large forces. Longer microtubules (Fig 3.2a) correspond to lower forces, but these microtubules often escaped the overhang before they started buckling because of large bending fluctuations induced by Brownian motion. Therefore observation time at lower forces is limited as well.

Several more buckling events were measured at a second tubulin concentration of 20 μM , for which the average free growth velocity was $1.88 \pm 0.03 \mu\text{m}/\text{min}$. Catastrophes on free microtubules occur more frequently as tubulin concentration is decreased [11,19,55]. Below 20 μM many microtubules did not reach a length sufficient to reach the barriers and buckling events were too rare to obtain a reasonably amount of data. Qualitatively, the same kind of events were observed at both 20 and 28 μM . Earlier data on force generating microtubules [47] was obtained at 1.21 $\mu\text{m}/\text{min}$ without hindrance of high catastrophe rates. The relation between growth velocity and catastrophe rate is however not constant when comparing different results published in the literature [11,19,55]. Apparently, details like the used tubulin purification scheme and the exact growth conditions influence the catastrophe rate.

Force and length analysis

Shapes of buckling microtubules on digitised images were quantified using computerised image-analysis every 2 seconds (see section 2.5). We only used events where microtubule plus ends were interacting with the barrier. For events where the free growth velocity could not be measured because the microtubule was already near the barrier at the start of our observation, we could often establish that the opposite site was a minus end. Our buckling-analysis method (section 2.7) assumes a seed that is clamped to the surface. Events where the seed rotated during buckling were discarded (2 out of 31 events). Rotation could often be checked by observing the direction of the minus end of the microtubule while the plus end was buckling. We also tested the quality of clamping by analysing thermal fluctuations of microtubules (see chapter 5). These combined observations show that in most cases the seeds are clamped well. In our buckling-analysis we assume as well that the contact point between microtubule and barrier remains constant during buckling. We therefore only analysed sequences of images for which no sliding could be observed by eye.

Chapter 3

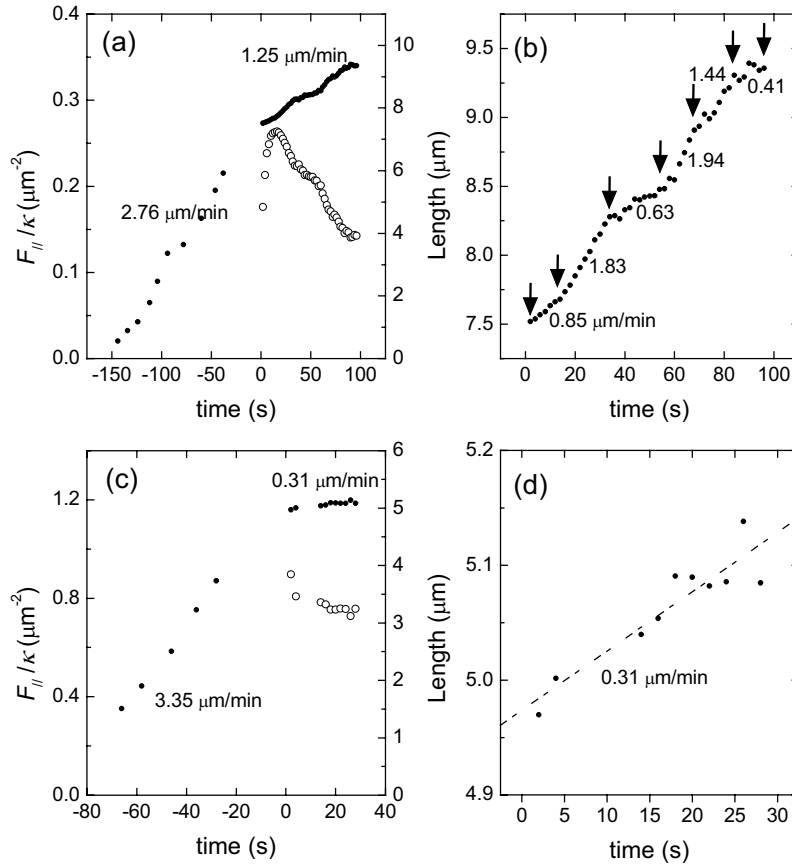


Figure 3.3 Fit results for two buckle events at $C_7 = 28 \mu\text{M}$. **(a)** Microtubule length (closed symbols, right axis) and normalised tangent force (open symbols, left axis) as found by fitting plotted for a microtubule with a moderate distance to the barrier. Before barrier contact ($t = 0$ s), the length of the microtubule is measured as the straight distance from the growing tip to the seed transition point, which is found by fitting. The average velocity, found by linear fitting, before and after barrier contact is indicated. This event terminated in sliding along the barrier. **(b)** An enlarged view on the length data of Fig. 3.3a during buckling. Arrows indicate time points at which the growth velocity apparently changed. Numerical values represent growth velocities in $\mu\text{m}/\text{min}$ as estimated by a linear fit to the data between two arrows. **(c)** A plot similar to Fig. 3.3a but for the microtubule depicted in Fig. 3.2b. This event terminates with the microtubule having a catastrophe while buckling. **(d)** Enlarged view on the length data of Fig. 3.3c, with a linear fit to the data during buckling superimposed. Some time points were skipped because the imaged microtubule was temporarily out of focus and poorly visible. The fitted average growth velocity is indicated.

The effect of force on microtubule growth velocity

Forces and microtubule lengths were derived by fitting the theoretical shape of an elastic rod to the observed shapes using methods that are described in chapter 2. The average distance between the fit and marker points on the microtubule was on the order of 50 nm (standard deviation). An example of the outcome of a fit is depicted in Fig. 3.3a and b for a microtubule for which the fitted barrier contact point is found at 7.5 μm away from the fitted seed transition point. The microtubule of which fit results are shown in Fig. 3.3c and d is depicted in Fig. 3.2b. For this microtubule, the distance between seed and barrier is only 5.0 μm , which makes it the shortest microtubule that was observed buckling and at the same time it corresponds to the largest force measured (10.6 pN). Time zero is chosen equal to the moment at which the microtubule finds a fixed barrier contact point. Buckling was clearly visible, for non-stalled microtubules, within three seconds after the microtubule found a fixed point. The length of a microtubule could often be analysed before it hit a barrier. Not all analysed microtubules were observed growing towards the barriers because they were already buckled (4 out of 29 events) or were very close to the barrier (7 out of 29 events) at the time they were found in the sample. The length of the microtubule before barrier contact is not plotted every 2 seconds, because Brownian motion of the free tip out of the focal depth of the microscope hindered length estimation. From the measured lengths plotted in Fig. 3.3a and c it becomes clear that the average growth velocity after buckling is significantly lower than the speed at which the barrier is approached. During buckling abrupt changes in growth velocity were often observed as visible in the enlarged view on the length data during buckling in Fig. 3.3b. For this event, the average growth velocity between such changes clearly varies around the mean velocity (during buckling) which equals 1.25 $\mu\text{m}/\text{min}$. Values between 0.41 and 1.94 $\mu\text{m}/\text{min}$ were recorded. In other buckling events indications for pauses in growth were found with an approximate duration of 10 seconds. Abrupt changes in growth velocity do not correlate with the tangent force component as plotted in Fig. 3.3a. Enlarged length data for the shorter microtubule is shown in Fig. 3.3d. The average length increase between two points is only 10 nm. No growth velocity variations could be observed because of the short duration of this event and the large relative measurement noise.

For each buckling event, the average velocity during buckling was fitted from the length data and an average value for the normalised tangent force component (F_{\parallel} / κ) was calculated (Fig. 3.4a). From Fig. 3.3a and c it is clear that both the velocity and the force are not constant during buckling. However, we worked with average values because they summarise the individual behaviour of one microtubule. Changes in force were often small during buckling. In fact, the largest relative change is shown in Fig. 3.3a, for which the standard deviation in the force divided by the average value equals 0.2. On average this value was 0.09.

Chapter 3

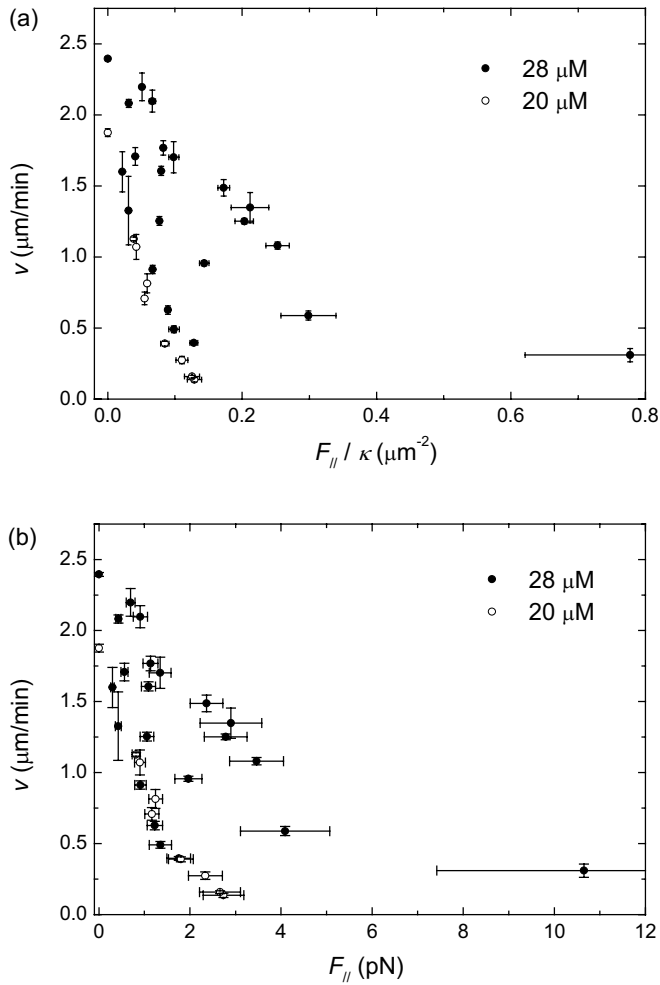


Figure 3.4 Force velocity curves showing average velocity and tangent force values per buckle event. **(a)** Velocity data versus normalised tangent force for 8 events at $C_T = 20 \mu\text{M}$ (open symbols) and 21 events at $C_T = 28 \mu\text{M}$ (closed symbols). The error in the force is based on the geometry of each buckling microtubule following rules that are described in section 2.7. The standard deviation in the fitted average speed is plotted in the vertical direction. Growth velocities at the two concentrations for free microtubule growth plus the standard error are plotted at zero force. **(b)** Same data as in Fig. 3.5a but with forces calibrated with rigidities estimated at the corresponding concentrations. The indicated error includes both the fit error as well as the uncertainty in the rigidity κ .

The effect of force on microtubule growth velocity

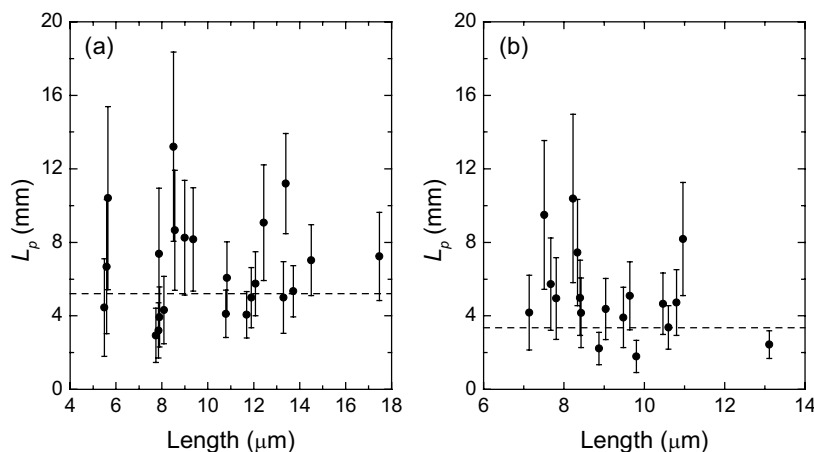


Figure 3.5 Analysis of microtubule flexural rigidity using thermal fluctuations of one single point per microtubule. (a) Persistence length for 23 microtubules at $C_T = 20 \mu\text{M}$ and the experimental error, which is given by Eq. 3.2, plotted versus the length between seed and analysed point. The average value (weighted with the errors) is indicated as a horizontal dashed line. (b) Persistence length data for 16 microtubules at $C_T = 28 \mu\text{M}$.

In paragraph 2.7 we discussed errors made in fitting a buckling event. The error bars on the force are calculated using the rules described there. The error in the measured average velocity during buckling is hard to assess because first, the force is not constant during buckling, second, fit errors are made in length measurements and third, velocity jumps during growth occur that give rise to a non constant velocity. To obtain an indication for the total error we calculated the average squared distance between the measured and fitted length data. Using the root of this value as error on the length data, one can estimate a standard deviation in the fitted average velocity (least-squares fit) [68].

Force calibration

In order to extract quantitative forces from the fit results, the value of the flexural rigidity, κ , of microtubules is needed. In chapter 5 we will summarise rigidity measurement methods used in the literature and present rigidity data obtained using a new approach. The new and literature data strongly suggest that microtubule rigidity depends on the exact growth conditions. Both the addition of an oxygen scavenging system and the tubulin concentration or growth velocity may effect microtubule rigidity. Because of these dependencies we made an effort to derive microtubule rigidity directly from the microtubules observed in the samples with buckling microtubules. The method described in chapter 5 could not be used in this case because the microtubules that were recorded on tape were short and often were only partially in focus because of the Brownian motion.

Chapter 3

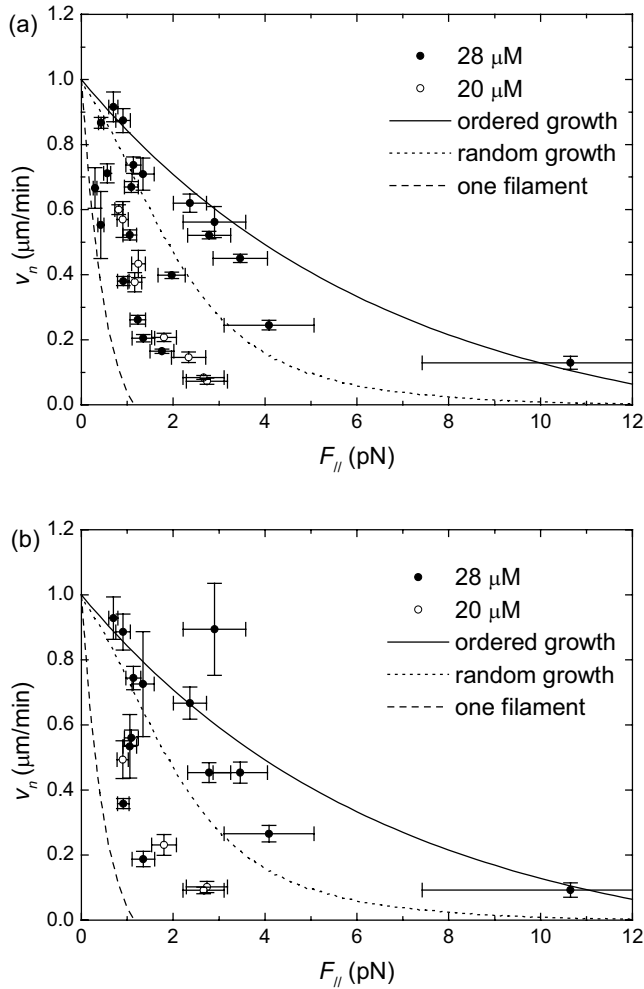


Figure 3.6 Force velocity curves showing normalised velocities, v_n , versus tangent force. **(a)** Events are the same as plotted in Fig. 3.5b but are divided by the average growth velocity at which the microtubule approached the barrier, i.e. $1.88 \pm 0.03 \mu\text{m}/\text{min}$ (\pm SEM) at 20 μM (open symbols) and $2.40 \pm 0.01 \mu\text{m}/\text{min}$ at 28 μM (closed symbols). **(b)** Selected events, 4 buckling events at $C_T = 20 \mu\text{M}$ (open symbols) and 14 events at $C_T = 28 \mu\text{M}$ (closed symbols), for which the velocity could be measured at which the microtubule approached the barrier. Velocity normalisation is done with these individual approach velocities and the plotted standard deviation is determined by both the standard deviations in the velocity before and during buckling. Three theoretical predictions for the normalised force velocity curve, calculated for $C_T = 20 \mu\text{M}$, are superimposed (see text).

The effect of force on microtubule growth velocity

Here, we used a less precise method that is often used in the literature and which uses thermal fluctuations of one single point of the microtubule (see methods section). In chapter five we compare results of both methods. Fluctuations of growing plus ends were analysed in the same samples that were used for the buckling experiments in order to guarantee that rigidity was measured for the right growth condition (see Fig. 3.5). Individual rigidity values are largely scattered around an average value at both concentrations. The error bars are large and the probability that all values at a single concentration can be drawn from a homogeneous parent distribution is 0.4 at 20 μM and 0.25 at 28 μM . The average rigidity, weighted with the error for individual microtubules, found was $21.2 \pm 1.7 \text{ pN}\mu\text{m}^2$ (\pm standard error of the mean) for $C_T = 20 \mu\text{M}$ and $13.7 \pm 1.4 \text{ pN}\mu\text{m}^2$ for $C_T = 28 \mu\text{M}$. Using these values, we calibrated the force data (Fig. 3.4b). The calibrated data clearly show that there are large differences between individual microtubules that can not be explained by the error bars. This is especially true for the 28 μM data around 1 pN, where average growth velocities are observed between 0.5 and 2 $\mu\text{m}/\text{min}$. The data obtained at $C_T = 20 \mu\text{M}$ shows less scatter than the 28 μM data and marks the bottom end of the force velocity data.

Velocity normalisation

The force-velocity data at both concentrations was normalised (Fig 3.6a) with the corresponding average free growth velocity shown in Fig 3.1. The two normalised data sets do more or less coincide although the 20 μM is still lower on average. We checked whether differences between individual microtubules are somehow correlated with the individual velocity, at which a microtubule approached the barrier before buckling that could be estimated for most microtubules. Individual free velocity values were scattered around the average value at a given concentration. The ratio between standard deviation and average was 0.16 and 0.20 at 28 μM and 20 μM respectively. The individual normalised velocity, i.e. the ratio between the average velocity before and after buckling, is plotted in Fig. 3.6b. The relative variance in the growth velocity around 1 pN clearly did not become smaller by normalisation of the velocity. We did not try to correct for possible differences between rigidity values of individual microtubules because the error on individual estimates is too large (Fig 3.5). Because of the individual differences between microtubules observed, we made an effort to extract the average behaviour from our data in order to compare growth at different tubulin concentrations. Therefore, each fit of a buckling microtubule was subdivided into segments consisting of two succeeding points. For each segment an average force was calculated and the velocity was calculated as the change in length divided by the time spacing between the two points, which was usually 2 seconds. Segments for all microtubules at a given tubulin concentration were sorted by force and successively binned. The number of segments in each bin was 43 ($C_T = 20 \mu\text{M}$) or 61 ($C_T = 28 \mu\text{M}$). The binned data is presented in Fig. 3.7 and 3.8 in a way that allows easy comparison with theoretical models.

3.4 Discussion

Stall force

We have presented quantitative results on force generating microtubules at larger growth velocities than studied previously [47]. Forces between 0.4 and 10.6 pN were observed. The largest force corresponds with the shortest microtubule that buckled which was positioned 5 μm away from the barrier at $C_T = 28 \mu\text{M}$. Many microtubules at this length were not observed to buckle but were apparently stalled. Note that length is not the only factor that determines force but that also the position of the barrier contact point relative to the direction of the seed influences force (see section 2.6). The maximum observed force suggests that the stall force is on the order of 10 pN at $C_T = 28 \mu\text{M}$. This is in reasonable agreement with the theoretical value for the stall force [32,53,54] of 17 ± 5 pN that can be calculated using Eq 1.9,

$$F_{stall} = \frac{k_B T}{\delta} \ln \frac{k_{on} C_T}{k_{off}},$$

where δ is taken equal to 8/13 nm and k_{on} ($2.65 \pm 0.27 \text{ s}^{-1} \mu\text{M}^{-1}$) and k_{off} ($5.6 \pm 2.9 \text{ s}^{-1}$) were obtained by fitting Eq. 1.3 to the data in Fig. 3.1. A precise experimental estimate of the stall force is however hard to obtain due to force-induced catastrophes that limit the lifetime of microtubules especially at high forces (see chapter 4). Because the slope of the force velocity curve is very small at high forces it is impossible to extrapolate the stall force with a reasonable accuracy from the force velocity curve [53].

Force dependency of rate constants

We can compare the observed decay in velocity with increasing force with theoretical predictions. In our experiments, force could in principal have influenced both the on- and off-rate for tubulin assembly. According to thermodynamic arguments, the ratio between on- and off-rate should equal Eq. 1.7,

$$\frac{k_{on}^* C_T}{k_{off}^*} = \frac{k_{on} C_T}{k_{off}} \exp\left(-\frac{\delta^* F_{//}}{k_B T}\right).$$

Growth is hereby assumed to be in the direction of $F_{//}$. We have written δ^* instead of δ because as we will discuss later, the microtubule length increase does not necessarily have to equal $\delta = 8/13$ nm for each assembly event. A variable δ was used by Kolomeisky and Fisher [69] to fit the experimentally observed force velocity data [47]. One can express concern about whether or not diffusion-limited behaviour is introduced by the vicinity of a barrier, which would cause Eq. 1.7 to fail in describing the assembly process. Nanometer sized thermal fluctuations of the microtubule tip away from the barrier, which are

The effect of force on microtubule growth velocity

necessary for growth, should be more frequent than the rate of tubulin assembly (k_{on}) for the assembly to be reaction limited [70]. For a microtubule that buckles against a barrier these fluctuations can be shown to be fast enough [48]. Furthermore slow diffusion of tubulin dimers in the close vicinity of the barrier could lead to an effectively lowered tubulin concentration near the barrier. Because the growth velocity is observed to be hardly lowered at small forces this effect can not play a significant role. Therefore we conclude that diffusion does not limit the reaction and Eq. 1.7 should give an accurate description of the assembly process.

We can make two extreme statements about the force dependency of the rate constants, and assume that only one of the two constants is changed [47]. When we assume that the only effect of an increasing force is a decrease in k_{on} , then by combining Eq. 1.3 and Eq. 1.7 we can write

$$v_n' = \frac{v + \delta k_{off}}{v_0 + \delta k_{off}} \approx \frac{\delta k_{on}^* C_T}{\delta k_{on} C_T} = \exp\left(-\frac{\delta^* F_{//}}{k_B T}\right). \quad (\text{Eq. 3.3})$$

For this assumption the quantity v_n' should thus be independent of the tubulin concentration and thus independent of v_0 , the free growth velocity. When we look at Fig. 3.7, we see that the two datasets and the set from literature [47] do indeed decay with approximately the same rate. The data obtained at $C_T = 20 \mu\text{M}$ might decay slightly faster but whether or not this is a consistent effect is hard to tell because of the limited amount of eight microtubules observed at this concentration. The model was fitted to the three data sets displayed in Fig. 3.7 all at the same time. We assumed that k_{off} is equal for the tubulin used here and the tubulin used by Dogterom and Yurke [47]. By fitting this simple model, we found $\delta^* = 1.8 \pm 0.2 \text{ nm}$ ($\chi^2 = 0.72$).

Alternatively, we assumed that the only effect of an increasing force is an increase in k_{off} . The quantity

$$v - v_0 = \delta (k_{off} - k_{off}^*) = \delta k_{off} \left(1 - \exp\left(\frac{\delta^* F_{//}}{k_B T}\right)\right), \quad (\text{Eq. 3.4})$$

now becomes independent of C_T and thus of v_0 . In Fig. 3.8 we plotted the force dependence of $v - v_0$ for the three datasets. Clearly the datasets do not coincide as well as in Fig. 3.7. The model was again fitted to all three data sets at the same time (Fig. 3.8) and again we assumed k_{off} (at $F_{//} = 0$) to be constant for all data sets. The model could not be fitted but converged to a very large value for k_{off} ($>10000 \text{ s}^{-1}$) and δ^* converged to zero. We confined the fit by fixing k_{off} to the experimentally observed value of 5.6 s^{-1} . This resulted in a reasonable value $\delta^* = 2.1 \pm 0.2 \text{ nm}$, but a large value for χ^2 , 13.6.

In conclusion, the combined data sets can be best fitted by a model, which assumes that only the on-rate is effected by force. To obtain this result we made assumptions about

Chapter 3

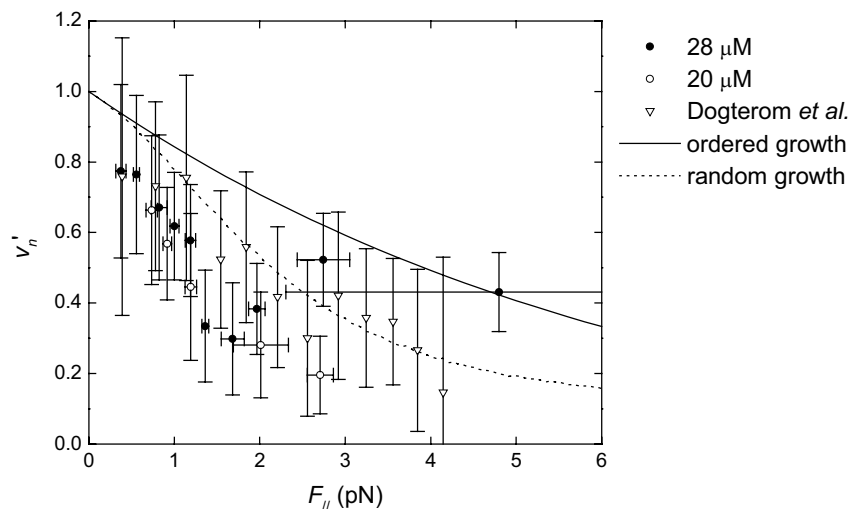


Figure 3.7 Data binned with respect to force following methods described in the text. Plotted is the quantity $v'_n = (v + \delta k_{off}) / (v_0 + \delta k_{off})$, where v is the velocity binned, v_0 the average velocity for free growth at the corresponding concentration, k_{off} the estimated off rate from Fig 3.1 and δ equals $8 \text{ nm} / 13$. The two measured data sets at $C_T = 20$ (open symbols) and $28 \text{ } \mu\text{M}$ (closed symbols) are compared with literature data [47] (triangular symbols). For each bin, the standard error of the mean for the velocity was calculated. The standard error in the binned and free velocity contributed both to the standard error that is shown. The standard deviation of the forces binned is plotted in the horizontal direction except for the literature data. Overlaid are two theoretical predictions based on ordered growth (dashed line) and random growth (straight line). The v'_n values calculated for the ordered model are concentration independent while the random growth model has a slight concentration dependence. The curve plotted here was calculated for $C_T = 20 \text{ } \mu\text{M}$ and the measured rate constants k_{on} and k_{off} .

the off-rate, k_{off} . This value was not estimated for the tubulin used in the earlier work by Dogterom and Yurke (DY) [47] and different values for k_{off} between 0.1 and 45 s^{-1} were reported in the literature [9]. We assumed that the off-rate for the DY-tubulin is equal to the value found for the tubulin used in this new study. However, a similar analysis for only the DY-data set, with a fitted value for k_{off} , can be made [47]. Again a model in which only k_{on} is affected by force was shown to be the more likely model. The combined approach that is chosen here does provide more evidence for this model. In chapter 4 we will present additional evidence for a force independent k_{off} . Despite, our results we can not rule out that both rate constants are effected by force in a way that satisfies Eq. 1.7. All we can say is that the largest effect is most likely on k_{on} . Quantitative statements about rate constants are difficult because of the large experimental variability observed.

The effect of force on microtubule growth velocity

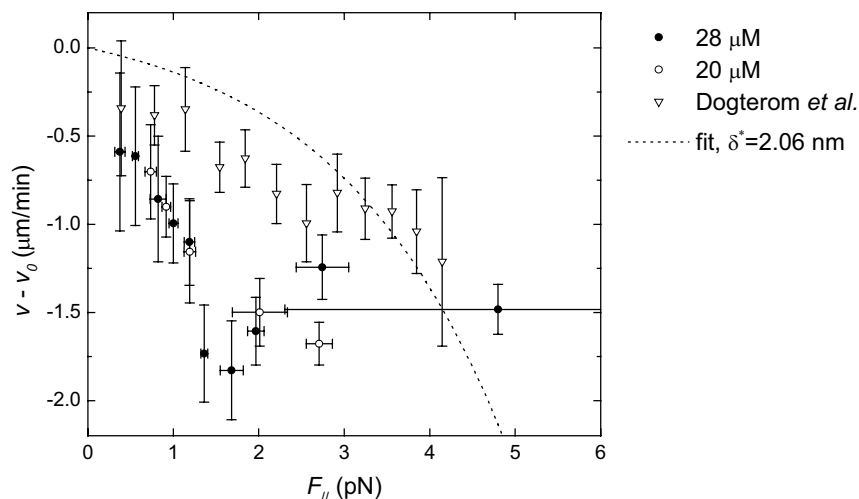


Figure 3.8 The data plotted are the same as plotted in Fig. 3.7, but presented differently. The average free growth velocity, v_0 , is subtracted from the non-normalised binned velocities, v , and plotted versus the tangent force. Symbols used have the same meaning as in Fig. 3.7. A fit to Eq. 3.4 with k_{off} fixed at 5.6 s^{-1} is shown (dotted line).

Multifilament models

As was already mentioned briefly, the elongation of a microtubule is not necessarily equal for each assembly event. Imagine that one of the 13 protofilaments inside the microtubule has grown in advance of the others and is carrying the entire load alone. If this filament grows by another tubulin-dimer it adds a full 8 nm to the microtubule's length and work equal to $F_{||} \times 8 \text{ nm}$ needs to be performed [48]. A filament that lags behind and whose end is positioned more than 8 nm from the barrier does not add to the microtubule's length when an extra dimer is added and no work is done. The value of δ^* in Eq. 1.7 is therefore not constant and thus not well defined. We can therefore understand why the value of δ^* found by fitting (1.8 nm for the constant k_{off} model) deviates from the average value of δ , which equals $8 \text{ nm}/13 = 0.62 \text{ nm}$. Apparently a good model should take collective effects caused by the approximately 13 protofilaments into account. A theoretical upper limit for the growth velocity under force can be obtained by taking δ^* equal to $8 \text{ nm}/13$ in Eq. 3.3 (k_{off} is taken load-independent). The curve is shown in Fig. 3.6a and b for $C_T = 20 \mu\text{M}$, but is only slightly different for $C_T = 28 \mu\text{M}$, when normalised. We refer to this upper limit as ordered growth because it assumes that elongation occurs in discrete steps all equal to $8 \text{ nm}/13$. By far the most normalised measured values are smaller than this upper limit. A theoretical lower limit (plotted in Fig 3.6a and b) can be obtained by setting δ^* equal to

Chapter 3

8 nm in Eq. 3.3 by which we assume that only one single protofilament is generating force while the others are constantly lagging behind. All normalised measured values are lower than this lower limit. Force velocity data for individual microtubules thus obey the thermodynamic limits.

Collective effects have been studied using a Brownian ratchet model, for a scenario where all protofilaments in a microtubule are assumed to grow and shrink independently of each other [48,53]. This random growth occurs when lateral contact between neighbouring protofilaments are weak (see Fig. 1.5). In this light, the described upper limit can be looked at as a situation for which lateral binding energies are high and where it is very unlikely that a protofilament grows in advance of others. The outcome of a simulation based on the measured values for k_{on} and k_{off} and $C_T = 20 \mu\text{M}$ is plotted in Fig. 3.6 and in Fig 3.7 with the right type of normalisation. The simulation for $C_T = 28 \mu\text{M}$ is only slightly different, when normalised. Given the experimental errors and the complete absence of fit-parameters the agreement between model and the average experimental data (Fig 3.7) is striking. The model however does not describe all observations made. The large variability in the observed normalised velocities for individual microtubules (Fig. 3.6) and the velocity jumps observed during buckling (Fig. 3.3b) can not be explained. Experimental uncertainties may explain part of the observed variability, but the model is likely to give an oversimplified view on force generation. Next, we will discuss observations that may explain these discrepancies.

Growth velocity fluctuations

Fluctuations in growth velocity between different microtubules and velocity jumps of single microtubules were already observed for free growing microtubules [71,72]. These fluctuations might be related to structural properties of microtubules. Electron microscopy work has shown that microtubules can be made of out of 10 to 16 protofilaments, form different lattice types and are able to switch between different filament-numbers and lattices while growing [72]. Besides difference in the microtubule core, it was also observed that microtubules are often not closed at their ends but form sheets of lateral connected protofilaments that are not folded into a tube [16]. These sheets do have an intrinsic curvature and curve away from the otherwise straight tube [16,73]. Observed sheets do not contain the full number of protofilaments over their full length but are slightly pointed towards their ends [16]. Microtubules with blunt ends and no sheets are observed as well. It is difficult to assign observed velocity changes to structural features because the structure can not be observed by light microscopy. It is likely that different structural features change the binding energies between tubulin dimers, which causes different assembly rates not only for free growing microtubules but also for microtubules under load. The presence of a sheet at the end of force-generating microtubules would complicate modelling a lot. Forces are now generated in a two step process. First by the growth of the sheet, which because of its intrinsic curvature does not occur at an angle

The effect of force on microtubule growth velocity

tangent to the folded tube and secondly by the closure of the sheet when it loses its intrinsic curvature and straightens against a force. Because these sheets might be transient and different in size [16] it is possible that they generate part of the observed velocity fluctuations under load. To complicate modelling even more, it is not clear how the hydrolysis of GTP interferes with the assembly process at the tip. In the model, only assembly and disassembly of GTP-tubulin is taken into account, while hydrolysis of the dimers at the tip might change rates [9,58] or hydrolysis might as suggested [73] influence sheet folding.

Additional explanations for the observed fluctuations have a more experimental origin. When modelling the growth process it is assumed that the growth process takes place perpendicular to a perfectly smooth barrier. In our experiments the barrier is rough and as the microtubule buckles further, it changes its angle to the barrier. The gap between protofilaments and the barrier is therefore dependent on the geometry, which might cause velocity fluctuations. Finally, we assigned a constant rigidity to all the microtubules under a certain growth condition. The fact that the average rigidity is dependent on the growth conditions, as observed here and in chapter 5, raises the question whether or not large differences in rigidity exist between different microtubules or between different segments in a single microtubule. These fluctuations would put larger error bars on the forces measured and lead to misinterpretations of the force-velocity relation. In chapter 5 no evidence was found for large rigidity fluctuations between seven approximately 30 μm long microtubules. However, the rigidity might fluctuate over a short micron sized length scale, which would average out on the final rigidity estimate for the complete microtubule. Such short-scale changes might be of importance here because we used shorter microtubules. This suggestion can not be tested with the rigidity data presented in Fig. 3.5 because of the large error bars. In chapter 6 we present a new approach to assembly-force measurements using optical tweezers, in which the stiffness of the tweezers calibrates the force instead of the microtubule rigidity. This experiment will complement data described here and does not suffer from rigidity uncertainties.

The above discussion shows the lack in knowledge on microtubule assembly that still exists. Despite this and the observed velocity fluctuations we obtained in Fig. 3.7 a consistent picture on the force-velocity relation averaged over many microtubules. The distance between the average behaviour and the thermodynamic upper limit shows that the assembly process might not be optimised to generate a large velocity under load. Apparently collective effects between multiple filaments play a role and some filaments grow in advance while others lag behind. The most likely end structure of a microtubule is therefore not a blunt end but a slightly frayed one.

We should comment on the implications of our finding to force generation *in vivo*. We have shown that microtubules are capable of generating relevant forces in excess of 4 pN and that the force at which growth is stalled might be around 10 pN for the tubulin

Chapter 3

concentrations studied. Quantitatively these forces are comparable to the forces generated by molecular motors like kinesin (6 pN [4]) for which it is well established that they do significant work inside living cells [1]. By comparing growth conditions for which the growth velocity for free growth was different, we found a consistent picture for which the normalised velocity under force, i.e. the ratio between velocity under force and the initial velocity, is independent of the free growth velocity. Here, we neglected small deviations from this ideal behaviour that are caused by the small off rate, k_{off} . Whether or not this observation can be extrapolated to the large growth velocities up to 20 $\mu\text{m}/\text{min}$ [74] that are observed *in vivo* remains to be investigated. Other proteins, like XMAP215 [75,76] have been shown to partly cause these high growth velocities, but they could also change the way that dimers are assembled or change the structure of the growing tip. It is conceivable that these proteins, or other proteins like for example those assembled onto the kinetochore, can optimise the assembly process such that the force velocity relation is pulled towards the thermodynamic upper limit discussed. Experiments with added assembly-stimulating proteins could be a next step to increase our knowledge about force generation *in vivo*. A possible different decay in the normalised force velocity curve may provide important information about how proteins can change the assembly of microtubules.

3.5 Acknowledgements

I would like to thank Cătălin Tănase for the Brownian ratchet calculations presented in this chapter and Sander van Doorn for his work on the Brownian ratchet model.

IV

Dynamic instability of microtubules under load

Free growing microtubules can switch into fast disassembly by an event, which is termed a catastrophe. This property is used extensively during cellular processes such as chromosomal and nuclear positioning. Observations in living cells suggest that the rate at which catastrophes occur is larger near the boundaries of the cell. In this chapter we show in an experimental model system that the catastrophe rate is increased by a growth opposing force. Force generation by microtubules near cellular boundaries is therefore a likely cause for the observed catastrophe rates. By analysing our quantitative results we show that the decreased assembly rate under load, as studied in chapter 3, is the most likely cause for the increased catastrophe rate.

4.1 Introduction

Microtubules are filamentous assemblies of the protein tubulin that in living cells constantly alternate between states of growth and rapid shortening. This non-equilibrium process, which is fueled by the hydrolysis of tubulin-bound guanosine triphosphate (GTP), is referred to as dynamic instability and is important for a wide variety of cellular processes [9]. Switches between growth and shortening (termed catastrophes and rescues) are clearly regulated by the biochemical machinery of the cell depending on the task at hand. The cell uses dynamic instability for example to find and position chromosomes during the formation of the mitotic spindle [9,29] or to seek contact with the confining cell geometry during positioning of the nucleus in fission yeast cells [42,77,78]. Forces are often applied to microtubules once such contacts are established. Microtubules generate forces by their own assembly [29,42,78] or become subject to forces exerted by motor proteins [41] in the sequence of events that follows after attachment. Despite the wealth of

Chapter 4

knowledge about dynamic instability and its dependence on tubulin concentration and other regulatory factors [9,11,19,79], very little is known about how forces interfere with dynamic instability. Recent *in vivo* work suggests that an opposing force may induce catastrophes when microtubules reach the cellular boundaries in fission yeast cells [42,78] and mammalian cells [74]. Knowledge about the effect of force on the catastrophe rate is needed not only to interpret these observations, but also to assess the possible role of force as a general mechanism to regulate microtubule dynamic instability.

In this chapter we quantify the effect of force on catastrophes by observing the buckling of single growing microtubules that strike a glass barrier *in vitro* [47,54,80]. We use the same experimental data as described in chapter 3 but pay more attention to sudden changes in growth direction that occur while the elastic restoring force of the buckled microtubule pushes the microtubule tip against the barrier. We compare our data to catastrophes under non-force generating conditions, and show that the observed switches under load are catastrophes that occur at a rate that is accelerated by force. The effect of force can be explained by a force-dependent decrease in the tubulin on-rate. *In-vivo* implications of our results will be discussed as well as possible implications for the, still largely unresolved molecular mechanisms behind dynamic instability and microtubule force generation.

4.2 Materials and methods

Most of the experimental techniques used were described in chapter 2 and additional information about the specific experimental conditions under which buckling microtubules were observed can be found in chapter 3. In addition to growth velocities of free growing microtubules we also measured disassembly velocities of shortening microtubules that were observed after a catastrophe. The methods used were similar to the methods used in chapter 3. This chapter mainly deals with catastrophe rates of free and force-generating microtubules. For free microtubules the catastrophe rate is defined as the inverse value of the average catastrophe time, T_c . This last value is the average time that a microtubule spends in an assembly state before it undergoes a catastrophe. Individual values are widely distributed around the mean value.

Measurement of T_c for free microtubules. We used two methods to infer T_c from growth events in our samples. The first method was used at low tubulin concentrations, C_T , of 7.2, 10 and 15.2 μM . Microtubules were observed growing after nucleation by seeds that were far away from the barriers. Catastrophes occurred frequently, which prevented microtubules from reaching the barriers. No rescue events were observed. For each growth event the time between nucleation and catastrophe was measured and the T_c was calculated as the average value. Individual values will be shown to be exponentially distributed around the mean. Therefore the standard error of the mean (SEM) is taken as T_c/\sqrt{N} with N the number of observed catastrophes [81]. At $C_T = 20$ and 28 μM

Dynamic instability of microtubules under load

microtubules grew longer and reached the barriers. For these concentrations T_c was defined as the total observation time of free microtubule growth divided by the number of observed catastrophes. Observation time stopped when a microtubule reached a barrier. The two methods are equal if catastrophe times are exponentially distributed or in other words if the catastrophe probability is independent of the microtubule length.

Measurement of T_c for buckling microtubules. For buckling microtubules, T_c was analysed as a function of velocity. All buckling events observed in a certain velocity range were grouped and the total observation time of buckling was calculated in this range. We included both buckling events that terminated by sliding or by a catastrophe. T_c was defined as the total observation time in a velocity range divided by the number of events that ended with a catastrophe in that particular range.

Buckling analysis of short microtubules. No buckling could be observed by eye for many microtubules that were nucleated within approximately 5 μm away from the barriers. Microtubules might however buckle with very low amplitude. Computer-aided image analysis was used to check for growth during barrier contact. For this purpose, we digitised parts of the recorded videotapes at video rate (25 frames/sec). The motion of a 1 micron-sized segment of an apparently stalled microtubule (Fig. 4.1c) was analysed starting at a time point at which barrier contact was not yet established. For this purpose we traced the microtubule segment (see section 2.5) and calculated its average position. The analysis was stopped when the microtubule disassembled after a catastrophe.

4.3 Results

Catastrophes on buckling microtubules.

Microtubules seeded more than approximately 5 μm away from the barrier were seen to continue elongation after they encountered the barrier (Fig. 4.1a and 4.2a). The shapes of buckling microtubules on digitised images were quantified using computerised image analysis every 2 seconds as discussed in chapter 3. Forces and microtubule lengths were derived by fitting the theoretical shape of an elastic rod to the observed shapes. A period of buckling terminated in different ways. Sometimes, the microtubule lost its point of contact and the microtubule started sliding along the barrier. Occasionally, a buckling microtubule switched to a phase of rapid shrinkage, which we refer to as a catastrophe under load. In Fig. 4.2b, the timed duration of each buckling event, referred to as barrier contact time, is plotted against the average growth velocity during buckling (inset Fig. 4.2a). The moment of buckling initiation is taken equal to the time that the microtubule finds a point of barrier contact that stays constant during buckling. This event evokes a clearly observable change in the lateral Brownian motion that is apparent on free microtubules and which ceases when the growing tip finds a fixed point at the barrier. All buckling events were divided over three velocity regimes. For every regime, the average

Chapter 4

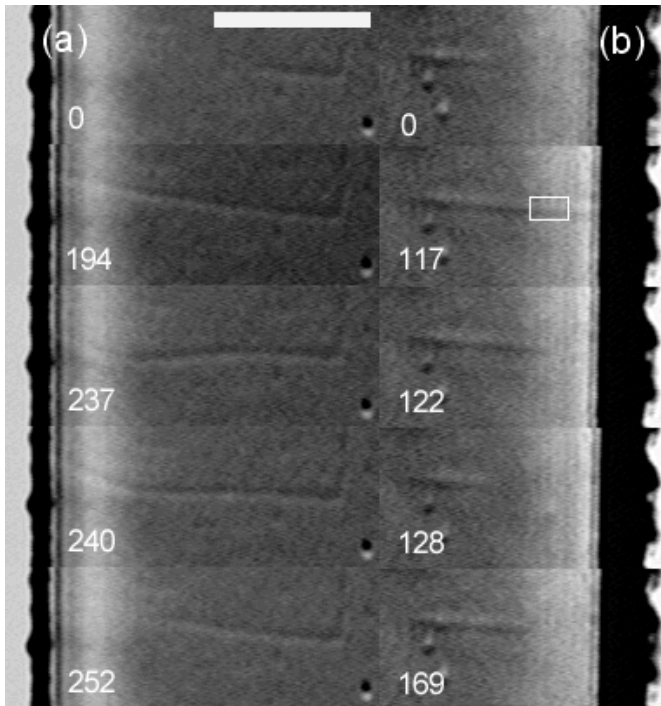


Figure 4.1 (a) DIC images of a growing and subsequently buckling microtubule. The barrier with overhang at the left obscures the imaging of the point of barrier-contact. Images show the initiation of growth ($t = 0$), establishment of barrier-contact, buckling, relaxation of the curved microtubule after a catastrophe and the continuation of shrinkage. (b) DIC images of a non-buckling stalled microtubule representing growth initiation ($t = 0$), the moment just before rapid shrinkage while contacting the barrier, shrinkage, the moment the shrinking microtubule reaches the seed and re-growth. The barrier is at the right. The motion of the segment in the box is analysed in Fig. 4.4. Scale bar equals $5 \mu\text{m}$. Numerical imprints represent time in seconds.

time between barrier contact and catastrophe (T_C) was calculated. The experimental accuracy of the measured T_C is low because of the limited amount of observed catastrophes. Catastrophes occur more frequently as the growth velocity is slowed down by force (Fig. 4.2c). For both concentrations studied, the growth velocity decreased with increasing force as shown in chapter 3.

Dynamic instability of microtubules under load

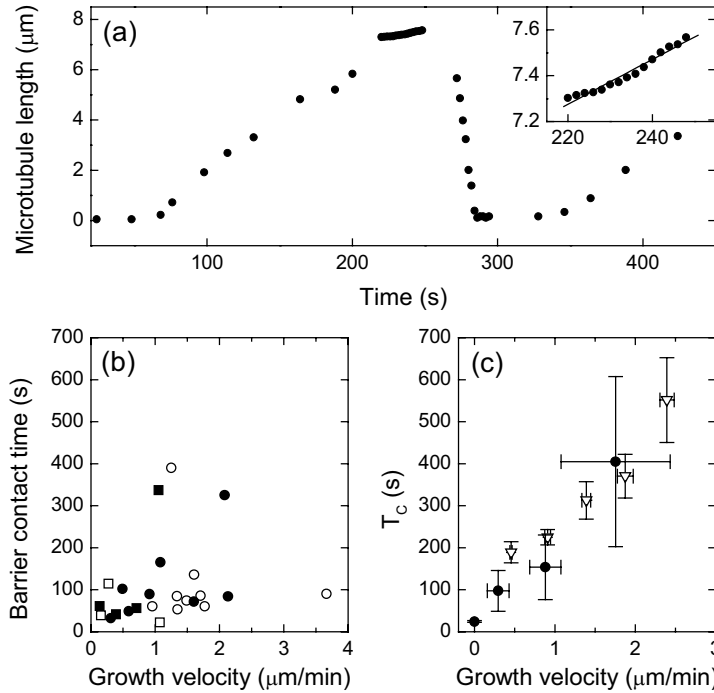


Figure 4.2 Analysis of microtubule dynamics. **(a)** The length of a growing microtubule before, during and after buckling. Nucleation from a seed ($t = 60$ s) is followed by growth at a rate of $2.5 \mu\text{m}/\text{min}$. microtubule-length was measured relative to the end of the seed. After initiation of barrier contact ($t = 200$ s), the average velocity equals $0.6 \mu\text{m}/\text{min}$. Velocities are determined using a linear fit to the length data which is shown expanded in the inset. Slipping of a microtubule over small distances is sometimes observed (e.g. $t = 250$ s) after which detailed length information is lost because a new pivot point can not always be found by fitting. Fast disassembly occurs after a catastrophe ($t = 270$ sec). **(b)** Barrier-contact times for buckling microtubules plotted as a function of the mean velocity during buckling. $C_T = 20 \mu\text{M}$ (7 microtubules, square symbols) or $28 \mu\text{M}$ (17 microtubules, round symbols). Times are shown for microtubules that undergo a catastrophe while buckling (closed symbols) and for microtubules that relax by sliding (open symbols). Complete relaxation by sliding stops barrier-contact time. Small slipping events after which the microtubule remains buckled are included in the contact-time. The velocity attributed to such a row of events is based on the frames for which microtubule shape fitting was possible. **(c)** T_C inferred from various experiments as a function of growth velocity. The average T_C and average growth velocity for free growth were obtained for five values of C_T . Data are plotted from left to right with increasing C_T (∇ -symbols), $7.2 \mu\text{M}$ (58 events), $10 \mu\text{M}$ (152), $15.2 \mu\text{M}$ (49), $20 \mu\text{M}$ (51) and $28 \mu\text{M}$ (30). For buckling microtubules, an average T_C was determined in three regimes of growth velocities using the data in Fig. 2B; $0 - 0.5 \mu\text{m}/\text{min}$, $0.5 - 1.08 \mu\text{m}/\text{min}$ and $1.08 \mu\text{m}/\text{min}$ and higher (\bullet -symbols). Each regime contains four events that terminate in a catastrophe. Average velocities are plotted with the standard deviation, weighted with the duration over which velocity was measured. The standard deviation gives a good indication for the width of velocity regime over which was averaged. The average T_C for stalled microtubules (see Fig. 4.3) is plotted with (standard deviation)/ \sqrt{N} as error (\bullet -symbol) at zero growth velocity.

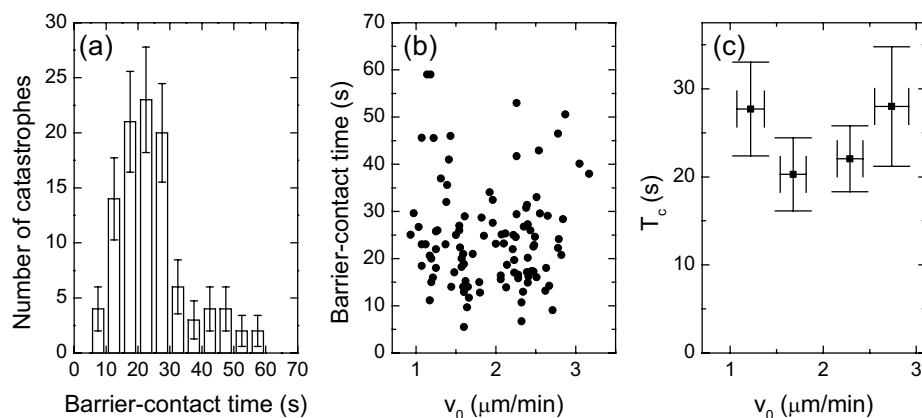


Figure 4.3 Barrier contact times of 103 stalled non-buckling microtubules measured at $C_T = 15.2, 20$ and $28 \mu\text{M}$. Uncommon small sliding events, after which contact was re-established always within 1 second are included in the barrier-contact time. **(a)** Histogram of the barrier-contact times. **(b)** Barrier-contact time as a function of the growth velocity at which the microtubule approached the barrier. **(c)** Average T_C -values in four velocity bins plus the standard errors. The standard deviation of the binned data is plotted as error on the velocity.

Catastrophes on stalled microtubules.

The effect of an opposing force on catastrophes was most clearly seen for microtubules that were seeded at a distance approximately less than five microns away from the barrier (Fig. 4.1b). These microtubules were not observed to grow after reaching the barrier and were apparently stalled. Experiments were done to study these events by focussing on seeds in close vicinity of the barrier at $C_T = 15.2, 20$ and $28 \mu\text{M}$. On average apparently stalled microtubules experienced a catastrophe 24.4 ± 1.1 seconds (average \pm SEM) after reaching the barrier (Fig. 4.3). The distribution of barrier-contact times for 121 non-buckling microtubules looks like a normal (Gaussian) distribution (Fig. 4.3a). No correlation could be found between the growth velocity at which the microtubule grows towards the barrier and the barrier-contact time (Fig. 4.3b and c). To check if a microtubule is really stalled we analysed the motion of a $1 \mu\text{m}$ long segment of a microtubule that by eye appeared to be stalled (Fig. 4.1b). The image quality of this particular event was very good which helped the analysis (Fig. 4.4). The initial Brownian motion of a free growing microtubule is shown to cease as barrier-contact is established and starts again after a catastrophe. The analysis shows that establishment of a fixed point of barrier-contact for a growing microtubule occurs within a few hundred ms. A slight drift in position of the segment equal to approximately $0.1 \mu\text{m}$ is observed during barrier-contact (Fig. 4.4) that could be buckling. Using the buckling equations of paragraph 2.6

Dynamic instability of microtubules under load

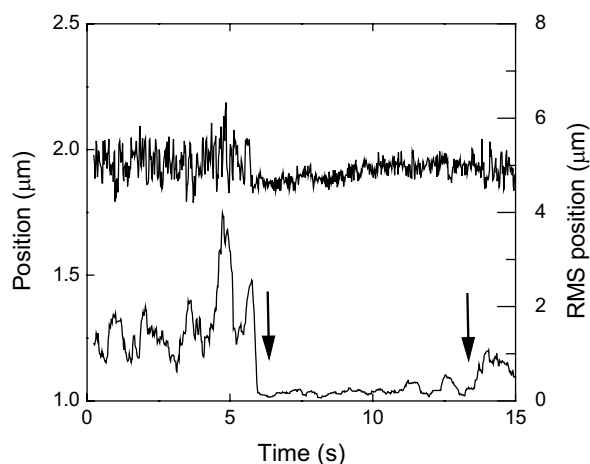


Figure 4.4 Analysis of thermal fluctuation and possible buckling on apparently stalled microtubules. The microtubule segment boxed in Fig. 4.1b was analysed before and after barrier-contact using computerised image tracing every 40 ms. Shown is the average vertical position of the microtubule (left axis, lower plot) as a function of time. The standard deviation of the position, calculated using a 25-point (1-s) moving window, is plotted as well (right axis, upper plot). The microtubule disappeared soon after a catastrophe, which terminated the analysis. Arrows indicate time points at which judging by eye, while looking at the CCD images, the Brownian motion abruptly changed, which corresponds to barrier contact initiation and catastrophe.

we calculated for this drift an upper limit for the growth velocity during barrier-contact of $0.05 \mu\text{m}/\text{min}$. This growth velocity is about a factor 40 lower than the growth velocity before barrier-contact and growth can thus effectively be considered as stalled. The analysis also showed that we could precisely (within 1 sec.) estimate the moment of barrier-contact initiation and catastrophe by eye (Fig. 4.4).

Catastrophe distribution for free growth

One of the unsettled issues of microtubule dynamics is whether or not catastrophes are stochastic events with first order kinetics or in other words: ‘Does the catastrophe probability depend on the time that a microtubule has spend in a growth phase?’. Experimental distributions of microtubule lengths [11] or catastrophe times [82] give some indications that there might be some non-first order kinetics. The catastrophe process under stalling conditions is certainly non-first order because the distribution is clearly not an exponential distribution (Fig. 4.3). As a control experiment, we checked the kinetics of free growing microtubules at $C_T = 10 \mu\text{M}$. We paid extra attention to the time of nucleation and to equal conditions for all analysed events. The length of a microtubule plus-end was measured every 2 s for more than 1 hour (Fig. 4.5a). Length was measured

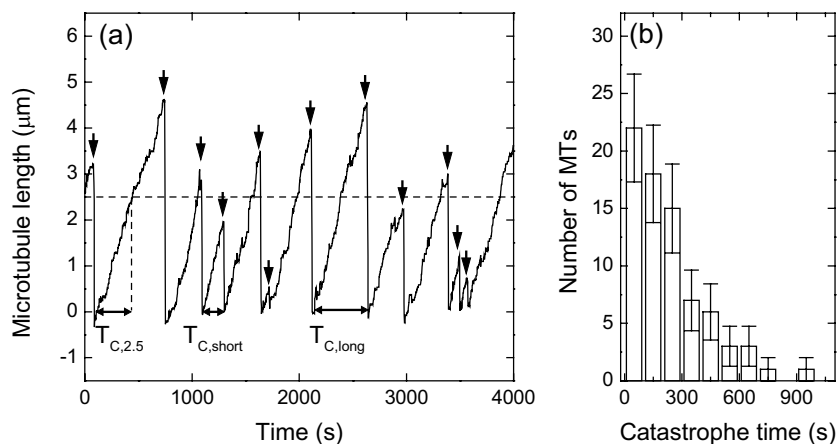


Figure 4.5 Dynamic instability of free growing microtubules measured at $C_T = 20 \mu\text{M}$ (a) The length of microtubules nucleated from a single seed as a function of time measured every 2 seconds. Arrows indicate catastrophe events. $T_{C,long}$ is the measured catastrophe time for a microtubule longer than $2.5 \mu\text{m}$, with $T_{2.5}$ the time at which a length of $2.5 \mu\text{m}$ is reached. $T_{C,short}$ is the catastrophe time for a shorter microtubule. The time of nucleation was estimated using extrapolation of the length data to zero length. (b) The distribution of T_C for the 76 events measured. Bin size = 100 s. The standard error is plotted as T_C/\sqrt{N} assuming a Poisson distribution.

relative to the end of the seed. In total five of these plots were obtained for five microtubules in a single field of view for which conditions were thus exactly identical. The exact moment of microtubule nucleation is hard to tell when observing video images of growing microtubules. By extrapolation of the length data to zero length, we obtained a good estimate of the growth time between nucleation and catastrophe.

The average T_C , equals 243 ± 28 sec. (average \pm standard error of the mean, 76 events) with an apparent exponential distribution (Fig. 4.5b). To check for an effect of microtubule length, we subdivided the microtubule length traces into parts shorter and longer than $2.5 \mu\text{m}$ (Fig. 4.5a). The measured growth times $T_{C,short}$, $T_{C,long}$ and $T_{2.5}$ are explained in Fig. 4.5a. For long microtubules T_C equals 208 ± 41 s (26 events on microtubules longer than $2.5 \mu\text{m}$, $T_C = \sum T_{C,long}/26$) and for short microtubules 264 ± 37 s (50 events on microtubules shorter than $2.5 \mu\text{m}$, $T_C = (\sum T_{2.5} + \sum T_{C,short})/50$). We are likely to miss catastrophe events on microtubules shorter than $0.2 \mu\text{m}$ because of the limited resolution of the microscope. Using an exponential distribution with a mean value of 243 s we found that six events are likely to be missed, which could in principal be added to the 50 events that were observed. Within experimental uncertainties we thus found no proof for a length dependent catastrophe time and the assumption that T_C is exponentially

Dynamic instability of microtubules under load

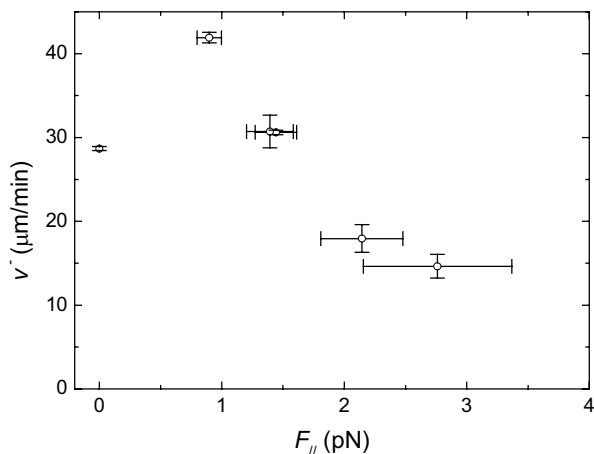


Figure 4.6 Force velocity curve for shortening microtubules. The velocity of shortening, \bar{v} , for five (1 at $C_T = 28 \mu\text{M}$ and 4 at $20 \mu\text{M}$) shortening events under load were derived using the same methods as used in chapter 3. The mean velocity plus the standard deviation are plotted versus the mean force. The error in the force is calculated following rules described in paragraph 2.7. At zero force the mean shortening velocity plus standard error is plotted for disassembly without load (19 events).

distributed is thus justified. We have used this distribution for the evaluation of T_C for free growing microtubules at $C_T = 20$ and $28 \mu\text{M}$ as presented in Fig. 4.2b.

Disassembly rates of microtubules.

To check whether disassembly occurs at a similar rate after a free catastrophe as after a catastrophe under load we measured shortening velocities. As a control experiment we analysed five disassembly events of free, no-force generating microtubules at $C_T = 10 \mu\text{M}$. The average shortening velocity was $27.7 \pm 0.3 \mu\text{m}/\text{min}$ (mean \pm standard error). In an earlier study it was shown that the shortening velocity is independent of C_T [19], and therefore we pooled data from $C_T = 20 \mu\text{M}$ and $28 \mu\text{M}$ to obtain the shortening velocity after a catastrophe under load. The analysis of shortening was started at the moment that a disassembling microtubule let go of the barrier. The average shortening velocity under this zero force condition was $28.9 \pm 0.3 \mu\text{m}/\text{min}$ (mean \pm standard error, 14 events), which seems in agreement with disassembly after a free catastrophe.

In between a catastrophe under load and the moment the disassembling microtubule let go of the barrier, we could study the shortening velocity under load. In total 13 catastrophes under load were observed. Disassembly occurred much faster than microtubule elongation and therefore in this case, the velocity and force during buckling was analysed every 40 ms, using the same techniques as used in chapter 3. Severe sliding along the barrier during disassembly made the fitting of a point of barrier contact

Chapter 4

impossible for 8 out of 13 events. The resulting 5 events were fitted, but sliding is still likely to have caused errors. Shortening velocity as a function of force averaged over each event is plotted in Fig. 4.6, together with the shortening velocity under zero force ($28.7 \pm 0.2 \mu\text{m}/\text{min}$, pooled over the 14 + 5 free shortening events described above). The average velocity over the five shortening events under load was $33.1 \pm 1.6 \mu\text{m}/\text{min}$ (mean weighted with the duration of each event \pm standard error).

4.4 Discussion

Within the limits of our measurements, we observed no difference between the velocity-catastrophe relation for free microtubules and microtubules under load. This observation and the observation that disassembly under zero load occurs at the same rate after both types of catastrophes shows that both events occur due to a similar mechanism. Slowing down a microtubule by the application of force or by the removal of free tubulin has thus a similar effect on the catastrophe time. We can compare our catastrophe measurements on stalled microtubules with data from literature. For free microtubules, a condition of zero net growth can be achieved when growing microtubules are exposed to the critical tubulin concentration, C_c . At this concentration there is thermodynamic equilibrium and the rate of subunit assembly, $k_{on}C_c$, equals the rate of disassembly, k_{off} . A T_C value of 10.8 sec was observed at a tubulin concentration of $3.3 \mu\text{M}$, slightly below C_c ($5 \mu\text{M}$ for this study) [79]. This value corresponds reasonably well with our value of 24.4 s measured for stalled microtubules, again suggesting that force and a decreased tubulin concentration (C_T) are interchangeable causes of catastrophes. The difference of a factor two between the reported values can be caused by differences in temperature (37°C vs 23°C) or experimental uncertainties.

Effect of force on k_{off} during elongation

Our data strongly suggest that force changes the on-rate, but not the off-rate of growing microtubules for the following reasons. Microtubule growth velocity depends on the C_T -dependent molecular on-rate, $k_{on}C_T$ (s^{-1}), and the C_T -independent off-rate, k_{off} (s^{-1}), following $v = \delta(k_{on}C_T - k_{off})$, where δ is the average microtubule length increase per dimer addition [19]. Both the rate constants k_{on} and k_{off} can in principal be force-dependent. Let us compare free growth and growth under load (at a higher C_T) at the same growth velocity. If k_{off} would be force-dependent, then the on-rate must also be different for both conditions in order to balance the velocity. T_C depends on both the on- and off-rate (amongst other parameters) in a way that is not well understood [9]. Therefore, the observed interchangeability between load and C_T (in its effect on T_C) can thus be most easily explained by assuming that k_{off} is force-independent, and both rates are equal at a given growth velocity both in the presence and absence of force. Thermodynamic arguments predict that the stall-force needed to stop microtubule growth equals

Dynamic instability of microtubules under load

$k_B T \delta^{-1} \ln(k_{on} C_T / k_{off})$ [48,54] (Eq. 1.9). Microtubules that grow at a higher velocity (higher C_T) towards the barriers are thus expected to experience a larger opposing force when stalled. We observed a v_0 -independent T_C for stalled microtubules (Fig. 4.3c), which again can be explained by assuming a force independent k_{off} . For stalled microtubules, the on-rate equals per definition the off-rate. Taking k_{off} force independent implicates in this situation a v_0 -independent k_{on} and thus a constant T_C . Brownian ratchet models [48,54] describe the force velocity curve for growing microtubules reasonably well, but suffer from a lack of knowledge about the exact molecular mechanisms at the growing tip (chapter 3). With the present knowledge about force dependencies of rate constants, we may hope to further decrease the level of uncertainties in these models. In addition, the exact mechanism or sequence of events that causes a catastrophe remains to be resolved. The T_C -distribution for stalled microtubules (Fig. 4.3a) is clearly non-exponential and therefore different from that for free microtubules (Fig. 4.5b), which suggests a different dominant mechanism that needs to be taken into account in our thinking about dynamic instability (see section 6.3).

Effect of force on k_{off} during shortening.

Besides an off-rate during elongation one can define a second off-rate during disassembly. Additional information on molecular off rates under load was obtained from our analysis of shortening events while the microtubule was still buckled. If there is any effect of a growth opposing force, F , on the shortening rate during disassembly, it is expected to be a disassembly enhancing effect because the free energy dip upon disassembly is lowered by an extra amount, $F \cdot \delta$, with $\delta = 8/13$ nm. The data as plotted in Fig. 4.6 show an opposite trend. Because of sliding, the errors on the shortening velocity are likely larger than indicated and therefore it is not clear whether the effect is real. For one particular event we are reasonably sure that the point of barrier contact remained constant over a duration of 4.8 sec. The initial length before disassembly was relatively long, 15.5 μm , and the buckling amplitude was large. This simplified the extrapolation of the buckled shape to the point of barrier-contact. For this microtubule we obtained a shortening velocity of 30.6 ± 0.3 $\mu\text{m}/\text{min}$ (mean \pm standard deviation) at an average force of 1.4 pN. Measured shortening velocities on free microtubules are very narrowly distributed around the mean value (standard deviation equals 1 $\mu\text{m}/\text{min}$), indicating that no large velocity differences occur between microtubules. If this property is preserved under load and the mean shortening velocity at 1.4 pN would be significantly different from that without load (let's say 40 $\mu\text{m}/\text{min}$), we would not expect an individual measurement of 30.6 $\mu\text{m}/\text{min}$. Furthermore, the average velocity of all events under load, 33.1 ± 1.6 $\mu\text{m}/\text{min}$, is close to the overall velocity without load, 28.7 ± 0.2 $\mu\text{m}/\text{min}$. Therefore, it is likely that the off-rate during disassembly is not largely altered by a force of a few piconewtons. Both k_{off} during elongation and shortening are thus likely to be constant under load. Constant molecular off-rates under load may be a general feature of cytoskeleton filaments.

Chapter 4

In vivo consequences

Our findings have consequences for microtubule dynamics *in vivo*. Recently reported observations showed that catastrophes occur more frequently at the cell periphery than in the cytoplasm in CHO and NRK animal cells [74] as well as in fission yeast cells [42,77,78]. Force is applied on a microtubule tip when it impinges on the cellular outer membrane and therefore, taken our observations, force is a likely cause for the increased catastrophe rate near boundaries. A force-dependent catastrophe rate gives the cell the opportunity to combine a high catastrophe rate near cellular boundaries with a negligible catastrophe rate in the cytoplasm without the need for localised catastrophe regulating factors. Evidence that microtubule assembly forces do play a role in cells comes from recent progress in imaging GFP-tubulin in fission yeast, which has led to new insights in assembly-based motility. In these cells interphase microtubules are attached to the nucleus and grow towards the cell cortex. Microtubules are seen to buckle, decrease their growth velocity and increase their catastrophe rate upon reaching the cortex [42,78]. The motion of the nucleus correlates with interactions of growing microtubules with the cortex [42]. Observed microtubules have lengths on the order of 5 μm and therefore generated assembly forces can be several piconewtons [42]. These findings combined with our *in vitro* results strongly suggest that assembly forces are responsible for both nuclear motion and an increased catastrophe rate. Computational models based on this assumption and experimental *in vitro* model systems show that catastrophes at the cortex are crucial requisites for nuclear positioning in the geometrical middle of the cell [42,49-51]. The efficiency of positioning depends on the assumed catastrophe rate under force.

We have shown that a force-induced catastrophe is an intrinsic property of microtubules that occurs without regulation by other proteins. The effect may be generally used by different cell types and for different ways of utilising assembly-based motility. Other proteins, like tip1 [77] are known to affect catastrophes and may play an additional role in these processes. Although microtubules are longer in larger animal cells they may be capable of generating piconewton assembly forces sufficient to induce catastrophes. Microtubules can effectively become stiffer by making links to the rest of the cytoskeleton or by forming bundles, which enables them to withstand higher forces. Force-induced catastrophes may be used to accelerate search and capture like processes [83]. Microtubules search for kinetochores or docking sites at the cortex but when capture fails a force-induced catastrophe quickly causes disassembly after which a new search direction can be tried. One could also argue that premature force-induced catastrophes are undesirable for example in chromosomal positioning during mitosis. Stabilisation of microtubules against catastrophes may therefore be needed during prolonged kinetochore attachment [29]. An accurate description of spindle dynamics [26,29] should take force-induced catastrophes into account. Other *in vivo* work suggests that the molecular motor dynein is often bound to the cell-cortex where it can bind microtubules and influence their dynamics [41]. Our work suggests a possible mechanism by which microtubule-dynamics

Dynamic instability of microtubules under load

is changed. The minus end directed motion of dynein might pull the growing plus-end of the microtubule into the cortex causing it to continue growth at a lower rate and making a catastrophe more likely. According to this picture, dynein does not have to interfere directly with the addition of new sub-units in order to have an effect on microtubule-dynamics. In general, a local change in microtubule dynamics inside living cells might be a clue for force generation by growing microtubules.

4.5 Acknowledgements

The work on stalled microtubules has been performed together with Mathilde de Dood. I would like to thank Wim van der Zande, Alfons van Blaaderen and Bela Mulder for a critical reading of the manuscript.

V

Rigidity measurements on growing microtubules using higher order thermal shape fluctuations

In chapter 3 we presented data on force generation by assembling microtubules. These experiments needed to be calibrated with the rigidity of microtubules. Here, we present rigidity measurements using thermally driven shape fluctuations on growing microtubules nucleated by surface-connected nucleation sites. Due to its long correlation time, the dominant first order fluctuation could not be sampled completely during the observation time of many minutes. Amplitudes of four higher-order, short-wavelength modes could, however, be sampled satisfactory. A mode analysis method was developed and tested that accounts for growth during observation. Significantly different rigidities were obtained at two different growth-conditions. We found that microtubule rigidity correlates with growth velocity.

5.1 Introduction

Microtubules are long protein filaments that are able to give mechanical strength to a living cell [1,2]. Their ability to do so depends on their flexural rigidity, a quantity that determines how the microtubule responds to applied forces and bending moments [65]. The flexural rigidity is determined by the chemical bonds within each individual protein and by the bonds between neighbouring tubulin proteins in the filament. Proteins and other compounds that are believed to effect these bonds, such as Microtubule Associated Proteins (MAPs), taxol and GMPCPP, have been shown to change the flexural rigidity [84-88].

Because of their rigidity, microtubules have been used as a very sensitive force probe. The buckling of microtubules was used to measure the force that microtubule based

Chapter 5

motor proteins exert [64] as well as the force microtubules can generate themselves by assembly [47] (see chapter 3). A precise estimate of the rigidity of microtubules is essential in order to calibrate these experiments.

Different experimental methods have been employed in the past to measure the flexural rigidity of microtubules. Distinction can be made between active and passive techniques. In active techniques, the rigidity is derived from an observed shape response to an experimentally controlled force. A homogeneous flow field was used [85,86], for example, to introduce a drag force that bends the microtubule. The drag coefficient, which determines the force applied, depends on experimental details and is a function of the distance between microtubule and cover slip [10,84,89]. This dependence is hard to estimate and thus introduces an unknown systematic error. Other active measurements are based on optical tweezers by which forces can be applied on objects that differ in refractive index from their surrounding liquid [90]. Tweezers were used directly on the microtubule to bend the filament [87,88]. The speed of relaxation to the equilibrium shape after tweezers are taken away is determined by the flexural rigidity and again the drag coefficient. Measuring relaxation times thus introduces similar systematic errors. Calibrated optical tweezers were used to exert a known compressive force on a microtubule via a silica bead coupled to the microtubule [91]. Considerable additional bending moments were also exerted on the microtubule in this geometry, which introduced experimental uncertainties. Furthermore, the calibration of optical tweezers is not without experimental errors. A last example of an active method is the observation of buckled microtubules inside lipid vesicles [92]. Forces are applied on the ends of microtubules by controlling the membrane tension of the vesicle. Controlling the number of microtubules inside the vesicle is hard in this experimental set-up.

In contrast to active techniques, no externally applied forces are needed in passive approaches to rigidity measurements. The shape of a microtubule is in thermal equilibrium with the surrounding liquid and as a consequence of thermal motion the bending of the filament changes continuously. These thermal forces are well characterised by the laws of statistical physics [56] and shape fluctuations can be used for rigidity measurements [10]. Central to this passive approach is the persistence length. For microtubules that are shorter than this length, the direction of one end of the filament is still correlated to the direction of the other end. Microtubules are in general much shorter than their persistence length, which is on the order of a few millimetres, and therefore the amplitudes of thermal motion are much smaller than their length. The advantage of passive methods in general is that neither externally applied calibrated forces nor an exact knowledge of the drag coefficient in liquid is needed.

Gittes *et al.* [10] observed shape fluctuations of stabilised microtubules in a sample-cell that was made so thin that motion was effectively confined to two dimensions. Observed bending shapes were projected onto Fourier cosine modes. The amplitude of every mode fluctuates over time with a correlation time that decreases with the mode

Rigidity measurements on growing microtubules

number. The measured variance in each mode amplitude can be linked directly to the rigidity of the filament. A good estimate of the mode variance can only be based on observations with a duration that many times exceeds the correlation time. Only then a microtubule is able to sample a large part of all accessible configurations. An additional advantage of the mode analysis over other methods is that each mode gives a statistically independent estimate of the flexural rigidity. Different modes can in principle be used to decrease the experimental error by averaging over several modes. In practice, only a few modes were observed because amplitudes get rapidly smaller for higher modes. One can check whether estimates based on different modes yield the same value for the persistence length and thereby test if basic assumptions made during the development of the theoretical background were correct.

Our interest in rigidity measurements is to obtain an accurate value for the rigidity that can be used to calibrate our experiment in which growing microtubules generate pushing forces [47]. One cannot rule out that the exact experimental conditions influence microtubule rigidity. It has been shown for example that lowering the temperature makes microtubules less rigid [84]. Apart from systematic errors related to the measurement method, differences in experimental conditions are probably part of the explanation of the large scatter in reported values for the rigidity. Rigidity measurements for naked microtubules, grown from GTP-tubulin alone, done with different experimental techniques range between 4 and 34 pN μm^2 [47,76,84-88,92]. For this reason we would like to measure the rigidity of microtubules for conditions similar to those in our force generation experiment with a method that introduces small systematic errors.

In our force generation experiment, microtubules grow from cover slip connected nucleation sites and the free end clearly exhibits thermally induced shape fluctuations. This configuration in which one side is clamped and the other end is free is known in literature as the cantilevered beam problem. The mode analysis seems appropriate to use apart from the fact that stabilised microtubules with a fixed length were used in the original work [10,84]. During a short observation time, however, a non-stabilised microtubule can be considered as having a fixed length. Using this approximation, thermal fluctuations of the free-end relative to its equilibrium position were measured in the cantilevered beam set-up [76,84,86]. This method gives in contrast to the mode analysis only a single persistence length estimate per microtubule. The configuration is prone to errors because small flows of fluid in a sample may cause non-thermal bending leading to an underestimation of rigidity. A mode analysis, similar to Gittes *et al.* [10], was applied as well to the cantilevered beam set-up using growing microtubules [85]. In their analysis the authors take the microtubule length as a constant and it is not clear what kind of errors are generated by microtubule growth. Microtubules used in this study were relatively short, approximately 25 μm , and as a consequence only the first mode amplitude was large compared to the experimental noise and could be used for a persistence length measurement. In general, doubling the length of a microtubule will increase amplitudes

Chapter 5

and will make twice as many modes observable. Long microtubule lengths have the disadvantage of long correlation times and long observation times become necessary, during which the microtubule will grow substantially and no constant length can be assumed.

We will show in the following sections that a mode analysis is also possible for microtubules that grow substantially during the observation time. For this we need solutions of the equation of motion for the cantilevered beam problem [93]. The clamping of one end of the microtubule increases correlation times considerably and changes the basic functions on which observed shapes should be projected. Building on these results out of literature we propose a suitable mode analysis, which is tested both theoretically and experimentally. We were able to obtain persistence length estimates based on four different modes and thereby test the assumptions made. Image analysis methods were used to digitise the shape of the observed microtubules in an unbiased and precise manner allowing us to decrease experimental noise.

5.2 Materials and methods

Sample preparation.

A flow cell was constructed by spacing two acid-cleaned cover slips, sized 24 mm × 24 mm and 24 mm × 60 mm, 25 μm apart using two lines of vacuum grease. Here we used two cover slips instead of one cover slip and a glass slide as described in paragraph 2.4. Cover slips display little visible roughness and give a good contrast between microtubules and surrounding. First, the cell was filled with 1 μm diameter latex beads (Sigma) in MRB80, which were allowed to stick to the surface for 5 minutes. The amount of beads added yielded about 500 beads per mm^2 of surface. Next, the cell was filled with biotin-labeled bovine serum albumin (Sigma, 2.5 mg/ml in acetate buffer pH 5.2, 5 min incubation), flushed with MRB80, refilled with streptavidin (1 mg/ml in MRB80, 5 min incubation), flushed again with MRB80 and filled with biotin-labeled nucleation seeds (400 fold diluted in MRB80, 5 min incubation, see paragraph 2.3). Tissue paper was used to blot solutions out of the flow cell while refilling. Finally a solution containing tubulin (Cytoskeleton, Denver, CO), 1 mM GTP and 10 mg/ml non-labelled BSA in MRB80 was flown into the flow cell. Measurements were done at two different growth conditions, three samples were made containing 28 μM tubulin and an added oxygen-scavenging system (OXS-system, paragraph 2.4) and one sample contained 26 μM tubulin without OXS-system. Pressure was applied on the top cover slip while blotting excess fluid, which reduced the sample thickness to the diameter of the latex beads. Hot candle wax was used to seal the flow cell along the edges.

Rigidity measurements on growing microtubules

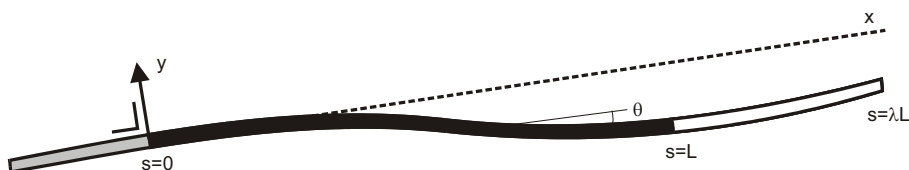


Figure 5.1 Notations used to describe the experimental configuration. The microtubule shape is described by $y(s)$ or alternatively by $\theta(s)$. The path length s is chosen to be zero at the transition between the clamped (grey) and the free (black plus white) part of the microtubule. The centre of the coordinate system is located at $s = 0$ with the x -axis along the direction of clamping. In the experiment only the length between $s = 0$ and $s = L$ (black) is analysed. During the course of the experiment the microtubule is growing. The time dependent relative length increase equals λ such that the total length of the microtubule equals λL .

Video microscopy and image acquisition.

Samples were observed by video-enhanced differential interference contrast (DIC) microscopy at 23°C. See paragraph 2.5 for details. The resulting image stream was digitised at a rate of 6 sec/frame online (SGI visual workstation).

Microtubule shape digitisation

The shapes of microtubules were digitised using image-processing algorithms described in paragraph 2.5 (see Fig. 5.2). The transition point between seed and free microtubule was determined while looking at the raw video stream in real time. This allowed the best observation of small thermal fluctuations close to the seed. A new transformed set of coordinates $[x, y]$ was obtained by rotation around this transition point, such that the new x -axis was in line with the direction of the seed (fig. 5.1). The horizontal spacing between two points, Δx , was approximately 50 pixels. The increase in microtubule path length between two consecutive points equals $\Delta x(1+(dy/dx)^2)^{1/2}$. A value for the local derivative, dy/dx , at a certain x -coordinate was estimated by applying a linear fit to 30 adjoining points.

Analysis of the full-length microtubule

In this section we look at the thermally excited dynamics of a microtubule that is clamped at one side and does not change its total length, λL , during the observation time (see Fig. 5.1). As a result of thermal motion, the tangent angle $\theta(s)$ along the microtubule deviates from the intrinsic value $\theta^0(s)$, which is small but not necessarily zero. Due to clamping the angle of the seed at $s = 0$ is constant over time, $\theta(0) = 0$. These statistical fluctuations [2] are described by

Chapter 5

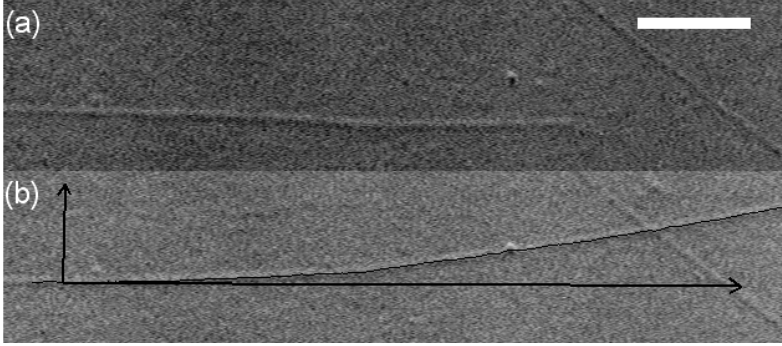


Figure 5.2 DIC images of a growing microtubule with an analysed length of 29.2 μm . **(a)** A plus end microtubule is nucleated by a seed at the left side. **(b)** The microtubule has grown out of our field of view. A digitised curve is superimposed on the image. The transition point between clamped and free microtubule collides with the centre of the coordinate axis. Digitised points are transformed to this coordinate system. Scale bar equals 5 μm .

$$\langle \cos [(\theta(s) - \theta^0(s)) - \theta(0)] \rangle = \langle \cos(\theta(s) - \theta^0(s)) \rangle = \left\langle \sqrt{1 - \left(\frac{dy}{ds}\right)^2} \right\rangle = \exp\left(-\frac{s}{2L_p}\right). \quad (5.1)$$

Angle brackets denote a time-averaged value. The persistence length, L_p , relates to the flexural rigidity κ (Nm^2) by

$$L_p = \frac{\kappa}{k_B T}, \quad (5.2)$$

where k_B equals Boltzmann's constant and T the absolute temperature.

In order to find the thermally-excited modes in a microtubule we look for solutions of the equation of motion for the full-length microtubule. Experimentally observed microtubules are much shorter than L_p , so by Eq. 5.1, θ will be small along the microtubule. The balance between elastic restoring forces inside the microtubule and the hydrodynamic drag experienced when moving [93] can in this small angle limit be written as

$$\kappa \frac{d^4 y}{ds^4} = -\gamma \frac{dy}{dt}, \quad (5.3)$$

where γ ($\text{kgm}^{-1}\text{s}^{-1}$) is the perpendicular drag coefficient for a microtubule in water per unit length. An infinite number of solutions to this equation of motion exist,

Rigidity measurements on growing microtubules

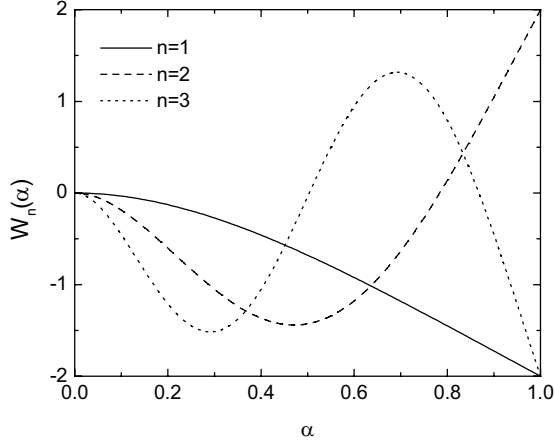


Figure 5.3 The spatial part W_n of the first three solutions to the hydrodynamic beam equation plotted as a function of the scaled path length $\alpha = s/\lambda L$. The functions are normalised on the interval $[0,1]$.

$$y_n(s,t) = e^{-t/\tau_n} W_n\left(\frac{s}{\lambda L}\right), \quad (5.4)$$

$$\tau_n = \frac{\gamma}{\kappa} \left(\frac{\lambda L}{q_n}\right)^4. \quad (5.5)$$

The spatial part, $W_n(s/\lambda L)$, is determined by boundary conditions [65,93]. At the clamped end these are $y(0) = 0$ and $y'(0) = \theta(0) = 0$. No bending moment or force is applied on a free end which implies $y'(\lambda L) = 0$ and $y''(\lambda L) = 0$. The solution written as a function of the scaled path length $\alpha = s/\lambda L$ equals

$$W_n(\alpha) = \frac{-\cosh q_n - \cos q_n}{\sin q_n + \sinh q_n} (\sin q_n \alpha - \sinh q_n \alpha) + \cos q_n \alpha - \cosh q_n \alpha \quad (5.6)$$

The values q_n are given by the subsequent solutions of

$$\cos q_n \cosh q_n = -1, \quad (5.7a)$$

$$q_1 \approx 1.875, q_2 \approx 4.695, q_3 \approx 7.855, q_n = (n - \frac{1}{2})\pi \text{ for } n > 3. \quad (5.7b..d)$$

The functions, W_n , are plotted in Fig. 5.3 for $n = 1, 2$ and 3 .

Chapter 5

If a microtubule is bent in a shape given by one of the functions W_n , it will relax to its native shape according to the relaxation time $\tau(s)$ given by Eq. 5.5, after externally applied forces are taken away [93]. Any arbitrary shape of a microtubule, $y(s)$, that satisfies the boundary conditions at the clamped and free end can be projected on the infinite series of functions W_n . For such microtubules these functions or modes form a complete orthonormal basis in function space and each mode relaxes with its corresponding τ_n [93]. We focus on microtubules that are bent by thermal forces and whose shapes thus satisfy the boundary conditions. These shape, $y(s)$, and mode amplitudes a_n may now be expressed as,

$$y(s) = \sum_{n=1}^{\infty} \sqrt{\frac{1}{\lambda L}} a_n W_n \left(\frac{s}{\lambda L} \right), \quad (5.8)$$

$$a_n = \sqrt{\frac{1}{\lambda L}} \int_{s=0}^{\lambda L} y(s) W_n \left(\frac{s}{\lambda L} \right) ds. \quad (5.9)$$

Due to thermal motion, the mode amplitudes will fluctuate in time, and mode relaxation happens while new excitations occur. The resulting correlation time of each mode amplitude equals the calculated relaxation time [10].

Next we calculate how much bending energy is stored in a bent microtubule. For any shape $y(s)$ the stored bending energy equals

$$U = \frac{1}{2} \kappa \int_{s=0}^{\lambda L} \left(\frac{d\theta}{ds} - \frac{d\theta^0}{ds} \right)^2 ds \cong \frac{1}{2} \kappa \int_{s=0}^{\lambda L} \left(\frac{d^2 y}{ds^2} - \frac{d^2 y^0}{ds^2} \right)^2 ds = \frac{1}{2} \kappa \sum_{n=1}^{\infty} \left(\frac{q_n}{\lambda L} \right)^4 (a_n - a_n^0)^2. \quad (5.10)$$

θ^0 , y^0 and a_n^0 describe the intrinsic, relaxed shape of the microtubule which is not necessarily straight [10]. In experiments microtubules are often observed to have an intrinsic curvature, which is probably caused by imperfections in the microtubule lattice. We made use of the small angle approximation

$$\frac{d\theta}{ds} = \frac{1}{\sqrt{1 - (dy/ds)^2}} \frac{d^2 y}{ds^2} \cong \frac{d^2 y}{ds^2}. \quad (5.11)$$

By Eq. 5.1, the time averaged value $\langle (dy/ds)^2 \rangle$ at $s = \lambda L$ approximately equals $\lambda L/L_p$. The error made in the derivation of Eq. 5.10 due to the small angle approximation can be shown to be less than 1% for the microtubules used in this study. For our purposes, we will neglect this error. To solve the integral in Eq. 5.10 [93] one uses integration by parts and the equality

Rigidity measurements on growing microtubules

$$\frac{d^4 W_n(\alpha)}{d\alpha^4} = q_n^4 W_n(\alpha). \quad (5.12)$$

Equipartition theorem [10,56] states that each quadratic term in Eq. 5.10 contributes on average $1/2k_B T$ to the total bending energy. The variance in the mode amplitudes thus equals,

$$\sigma_n^2 = \left\langle (a_n - a_n^0)^2 \right\rangle = \frac{k_B T}{\kappa} \left(\frac{\lambda L}{q_n} \right)^4 = \frac{1}{L_p} \left(\frac{\lambda L}{q_n} \right)^4. \quad (5.13)$$

Experimentally, the variances in mode amplitudes can be deduced from observed shape fluctuations [10]. Eq. 5.13 links the observable variance to the quantity of interest being the persistence length. The correlation time of the fluctuations determine the time scale on which the variance can be sampled [10]. In order to calculate the correlation time for subsequent modes, we need an estimate for the perpendicular drag coefficient γ in the vicinity of surfaces [84], which in our case are the two cover slips

$$\gamma \cong \frac{8\pi\eta}{\ln\left(\frac{4h}{D}\right)}. \quad (5.14)$$

Here η ($\text{kgm}^{-1}\text{s}^{-1}$) equals the viscosity of water, h the distance to the cover slips and D the diameter of the microtubule. In the experiment we restrict ourselves to the observation of microtubules that have a maximum length of $60 \mu\text{m}$. For such microtubules we calculate for $h = 0.5 \mu\text{m}$ and $D = 25 \text{nm}$, $\tau_1 = 400 \text{s}$, $\tau_2 = 10 \text{s}$, $\tau_3 = 1.3 \text{s}$. and $\tau_4 = 340 \text{ms}$. In order to make a good experimentally estimate of σ_n^2 , we need to sample values of a_n over a time period exceeding many times τ_n . Furthermore, the sample time between two measurements has to exceed τ_n for the acquisition of statistically independent samples. A good estimate of the variance in the amplitude of the first mode can thus only be obtained with a total observation time on the order of an hour which is unpractical and even unfeasible in our case because dynamic instability limits the lifetime of microtubules when they are not stabilised. A shorter observation time may cause an underestimation of the variance and an overestimation of the derived persistence length. A measurement of the rigidity of approximately $60 \mu\text{m}$ long microtubules in the experimental condition depicted in Fig. 5.1 can thus only be based on the second or higher modes.

For a microtubule that is free to move at both ends the correlation time of the first mode can be shown to be a factor 40 shorter [10]. This dramatic difference in correlation time is purely a consequence of the imposed boundary condition at $s = 0$.

Chapter 5

Analysis of only a part of the full-length microtubule

In the preceding section we showed in Eq. 5.13 that the variance in every mode is a strong function of the full-length of a microtubule. It is therefore not clear how we should define a variance in case of a microtubule that grows during observation. In this section, we examine the following questions. Can we infer the rigidity of a microtubule by only observing part of its length and how does the slow correlation time, τ_1 , interfere with this process?

For our purposes, we analyse only the first fraction (fraction size = $1/\lambda$, Fig. 5.1) of the microtubules length between $s = 0$ and $s = L$. The equation of motion for this part alone cannot be solved because boundary conditions are not constant at $s = L$. However, we would like to make a similar projection of the observed shape fluctuations onto a set of orthonormal functions and apply equipartition theorem again. We try to use a set W_l similar to Eq. 5.6, with $\alpha = s/L$. We obtain an expression for the shape of the analysed length and the new mode amplitudes

$$\tilde{y}(s) = \sum_{l=1}^{\infty} \sqrt{\frac{1}{L}} \tilde{a}_l W_l \left(\frac{s}{L} \right), \quad (5.15)$$

$$\tilde{a}_l = \sqrt{\frac{1}{L}} \int_{s=0}^L y(s) W_l \left(\frac{s}{L} \right) ds. \quad (5.16)$$

A tilde in general denotes a quantity for the analysed length L . The new mode amplitudes do fluctuate due to thermal motion and will show to be a good observable for measuring persistence length. By substitution of Eq. 5.8 we may write Eq. 5.16 as

$$\tilde{a}_l = \sum_{n=1}^{\infty} a_n \eta_{n \rightarrow l}. \quad (5.17)$$

The coupling coefficients $\eta_{n \rightarrow l}$, that link full-length mode amplitudes a_n to the analysed-length mode amplitude \tilde{a}_l are a function of λ

$$\eta_{n \rightarrow l}(\lambda) = \sqrt{\frac{1}{\lambda}} \int_{\alpha=0}^1 W_n \left(\frac{\alpha}{\lambda} \right) W_l(\alpha) d\alpha. \quad (5.18)$$

Coupling coefficients were when needed calculated using numerical methods (Mathematica, Wolfram Research).

Next, we calculate to what amount the full-length mode amplitudes, of which we know the correlation times, contribute to the variance of the new mode amplitudes. Because of Eq. 5.17 we write for the long-term variance of the new mode amplitudes

Rigidity measurements on growing microtubules

$$\tilde{\sigma}_l^2 = \sum_{n=1}^{\infty} \eta_{n \rightarrow l}^2 \sigma_n^2. \quad (5.19)$$

The functions, W_l , satisfy the boundary conditions at $s = 0$, but imply wrong boundary conditions at $s = L$. Therefore, the summation in Eq. 5.16 is expected to equal $y(s)$ at the open interval $[0, L>$ and the following bending energy calculation is only an approximation that will be tested afterwards. We write

$$U \cong \frac{1}{2} \kappa \int_{s=0}^L \left(\frac{d^2 \tilde{y}}{ds^2} - \frac{d^2 \tilde{y}^0}{ds^2} \right)^2 ds = \frac{1}{2} \kappa \sum_{n=1}^{\infty} \left(\frac{q_l}{L} \right)^4 (\tilde{a}_l - \tilde{a}_l^0)^2. \quad (5.20)$$

Using equipartitioning on Eq. 5.20 we find a more convenient expression for the long-term variance that directly links variance to the persistence length

$$\tilde{\sigma}_l^2 \cong \frac{1}{L_p} \left(\frac{L}{q_l} \right)^4. \quad (5.21)$$

Note that the calculated variance is not a function of λ and therefore does not change if the microtubule grows which was a problem in Eq. 5.13. For our envisaged experimental condition this mode analysis thus looks promising.

By dividing Eq. 5.19 by Eq. 5.21 we can normalise all contributions to the analysed-length variance,

$$\sum_{n=1}^{\infty} \eta_{n \rightarrow l}^2 \left(\frac{\lambda q_l}{q_n} \right)^4 \cong 1. \quad (5.22)$$

The normalised contributions of the first eleven full-length modes (n) to the first 6 analysed-length modes (l) are plotted in Fig. 5.4a. For λ equals 1.5, a value that on average represents the experimental conditions used in this study, a narrow distribution of full-length modes contribute to the variance in the analysed-length modes. In general only two successive full-length modes contribute significantly for a certain value of l for λ equals 1.5. For example, for $l=2$ only $n=2$ and $n=3$ contribute significantly whilst other contributions are only minor. The sum over all contributions $n=1$ to 11 for $l=2$ very nearly equals 1. For $l=6$ this sum deviates most from unity and equals 0.995, which indicates that modes larger than 11 play a negligible role. We conclude that for all practical purposes Eq. 5.21 is a very good approximation for the analysed-length mode variance. For $\lambda=3$ distributions become broader and full-length modes larger than 11 start to play an important role for $l=4$ and higher.

Chapter 5

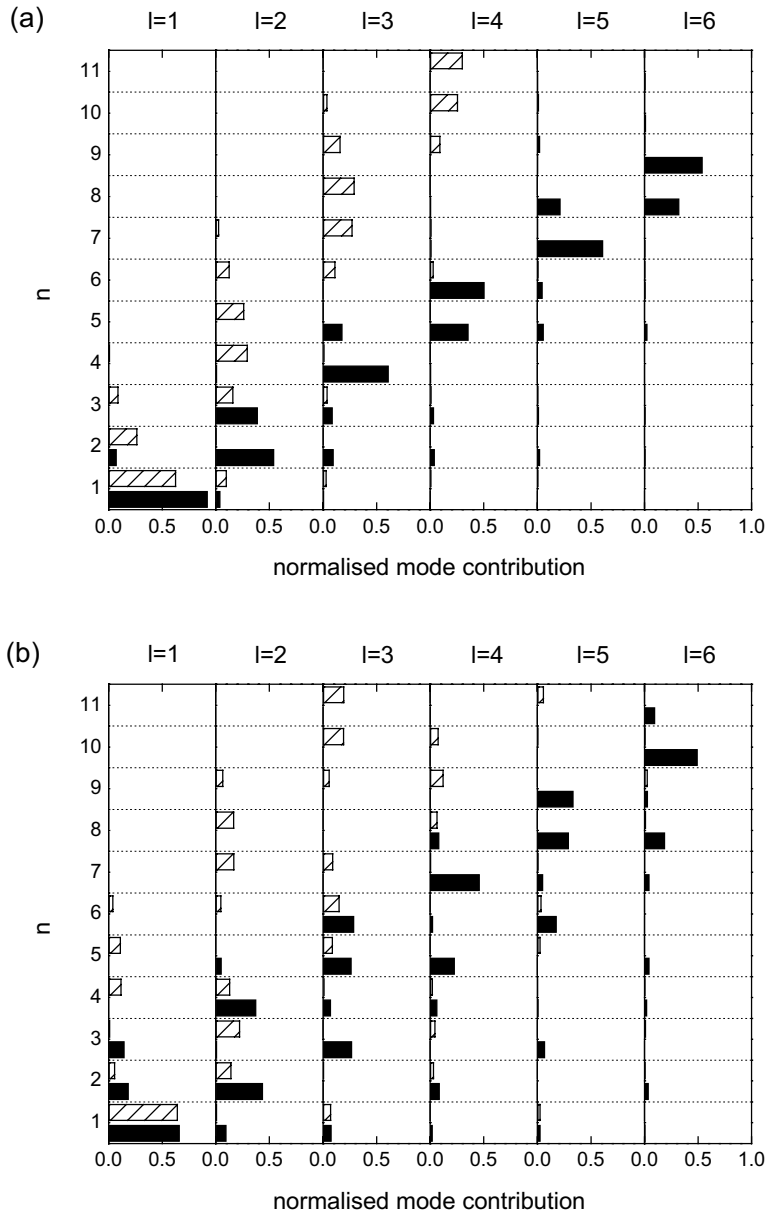


Figure 5.4 Normalised contributions of the first eleven full-length modes (n) to the first 6 analysed-length modes (l) for $\lambda = 1.5$ (filled bars) and $\lambda = 3$ (hatched bars). Plotted contributions equal $\eta_{n \rightarrow l}^2 (\lambda q_l / q_n)^4$ for projections of $y(s)$ onto the W -functions of Eq. 5.6 (a). Contributions for projections of $\theta(s)$ onto Fourier cosine functions are plotted as well for the same values of λ (b).

Rigidity measurements on growing microtubules

The correlation times of the new modes \tilde{a}_l are a priori unknown and are ill-defined because they do not represent solutions of the equation of motion. With help of Fig. 5.4a we can however estimate the temporal behaviour of the analysed-length modes. For $\lambda = 1.5$, we see that τ_2 and τ_3 dictate fluctuations for $l = 2$ and that the longest correlation time τ_1 hardly plays a role. In general, the following picture arises. The contributing full-length modes for a certain analysed mode l peak around $n = \lambda l$. The correlation time of an analysed-mode is thus roughly given by $\tau_{\lambda l}$, which using Eq. 5.7d can be written as the following rule of thumb

$$\tilde{\tau}_l \approx \frac{\gamma}{\kappa} \left(\frac{L}{q_l} \right)^4. \quad (5.23)$$

Full-length mode amplitudes for two different values of n are independent quantities and are thus not correlated in time. Analysed-length modes can also be considered as independent modes because distributions plotted in Fig. 5.4a hardly show any overlap. Small dependencies do exist for example between $l = 3$ and $l = 4$ which both depend significantly on $n = 5$. Apart from small dependencies, analysed-length mode amplitudes do provide to a large degree independent estimates of L_p .

Next we try to estimate variances within a finite observation time. Imagine a fixed-length microtubule that is observed during an observation time T which is on the order of τ_1 . The ratio, ε_n , between the full-length mode variance in the observation time T and the long-term variance σ_n^2 is defined by

$$\text{var}^T(a_n) = \varepsilon_n \sigma_n^2. \quad (5.24)$$

Based on the calculated correlation times and an assumed observation time of approximately 10 minutes, we take $\varepsilon_1 < 1$ and $\varepsilon_n = 1$ for $n > 1$. Due to the finite observation time the observed variance in the analysed-length mode will differ from the long-term variance. Using Eq. 5.17, we obtain

$$\text{var}^T(\tilde{a}_l) = \varepsilon_1 \eta_{1 \rightarrow l}^2 \sigma_n^2 + \sum_{n=2}^{\infty} \eta_{n \rightarrow l}^2 \sigma_n^2 = \frac{1}{L'_{p,l}} \left(\frac{L}{q_l} \right)^4. \quad (5.25)$$

If we now mistake the measured variance for the long-term variance we obtain a mode number dependent false estimate of the persistence length $L'_{p,l}$,

$$\frac{L_p}{L'_{p,l}} = 1 - \eta_{1 \rightarrow l}^2 \left(\frac{q_l \lambda}{q_1} \right)^4 (1 - \varepsilon_1). \quad (5.26)$$

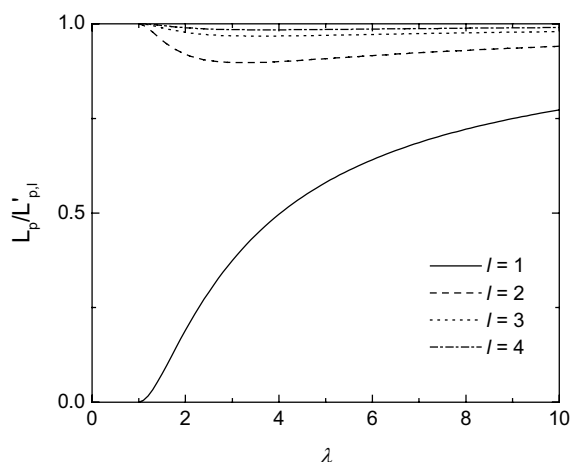


Figure 5.5 The ratio $L_p / L'_{p,l}$, calculated by Eq. 5.26, plotted for the first four mode numbers as a function of λ . The assumptions made, $\varepsilon_l = 0$ and $\varepsilon_n = 1$ for $n > 1$, are valid for microtubules with lengths for which τ_2 is small compared to the observation time.

The former equation is plotted for the first four modes for different values of λ for the worst-case scenario $\varepsilon_l = 0$, for which the variance in the 1st mode of the full-length microtubule is completely zero during the observation time (see Fig. 5.5). In Fig. 5.4a this corresponds to leaving out the variances in the bottom row for $n = 1$. For this situation large errors are made if persistence length estimation is based on the first analysed-length mode. For the second mode the error made is at most 10% and for higher modes errors can be neglected. Our experimental conditions are such that ε_1 will be much closer to 1 and errors made will be even smaller. In our experiment the microtubule grows while we analyse only the fixed-length L . The value λ increases continuously but large errors are for no single value of λ introduced except for $l = 1$. We conclude that a good estimate of the persistence length based on the 2nd and higher analysed-length modes must be possible without introducing large systematic errors. Note that all of the above is only valid if the full-length of the microtubule is small enough to justify the assumption $\varepsilon_2 = 1$.

Projections on cosine modes

Finally, we can check how full-length modes contribute to analysed-length modes if shapes are projected onto a different set of orthonormal functions. In the original mode analysis [10], the tangent angle $\theta = dy/ds$ along the microtubule, instead of y , was projected onto Fourier cosine modes. Cosine modes mimic the solutions of the equation of motion for a situation where both ends are not clamped. To check how these modes would work as analysed-length modes in the cantilevered beam problem, we differentiated the

Rigidity measurements on growing microtubules

full-length modes of Eq. 5.8, to obtain $\theta(s)$ and project them on cosine functions. The mode amplitudes of the analysed-length equal

$$\tilde{u}_l = \sqrt{\frac{2}{L}} \int_0^L \theta(s) \cos\left(\frac{l\pi s}{L}\right) ds = \sqrt{\frac{2}{\lambda L^2}} \sum_{n=1}^{\infty} a_n W_n'\left(\frac{s}{\lambda L}\right) \cos\left(\frac{l\pi s}{L}\right) ds. \quad (5.27)$$

New coupling coefficients as in Eq. 5.17 can be calculated and the contributions of the full-length modes to the total variance in \tilde{u}_l can be calculated and normalized to the total variance, which equals $L^2/(L_p n^2 \pi^2)$ [10]. These values are plotted in Fig. 5.4b for λ equals 1.5 and 3. The distribution of contributing modes is in general broader and extends to higher values of n than the contributions for the W -functions of Eq. 5.6 (see Fig. 5.4a). For $\lambda = 3$ and $l = 3$ the first eleven full-length modes together only contribute 89% of the total variance. This value is still 99% for the W -functions. An easy expression for the correlation time of the analysed mode such as Eq. 5.23 cannot be given.

Sources of Error

The discussion on errors introduced by the slow fluctuation time of the first mode is central in our approach and is discussed in the previous paragraph. Other possible sources of errors do exist and will be discussed below. Most of these errors were already discussed in the literature [10] but need to be reassessed for the cantilevered beam geometry under study.

Statistical errors in the measurement of $L'_{p,l}$

The variance in the mode amplitudes is a direct measure of the persistence length. The error in the persistence length is thus directly related to the experimental inaccuracy in the determination of $\text{var}^T(\tilde{a}_l)$. The standard deviation, δ , [10] is given by

$$\delta \text{var}^T(\tilde{a}_l) = \sqrt{\frac{2}{M-1} \text{var}^T(\tilde{a}_l)}. \quad (5.28)$$

M is the number of samples in the observation time T . This equation only holds if all estimates of \tilde{a}_l used in the calculation of $\text{var}^T(\tilde{a}_l)$ are statistically independent of each other. The correlation time of the first full-length mode, which is larger than the sample time, governs the time dependence of \tilde{a}_l . Therefore successive estimates of \tilde{a}_l are not statistically independent and the error in $\text{var}^T(\tilde{a}_l)$ is underestimated. Second and higher mode amplitudes are governed by τ_2 or even shorter correlation times and therefore Eq. 5.27 gives a good error estimate for higher modes numbers.

Instead of analysing $L'_{p,l}$ we will work with $\ln(L'_{p,l})$ because for this quantity the statistical error in the plus and minus direction is approximately equal [10]. We therefore write,

Chapter 5

$$\ln(\dot{L}_{p,t}) = \ln\left(\frac{L^4}{q_t^4 \text{var}^T(\tilde{a}_t)}\right) \pm \sqrt{\frac{2}{M-1}}. \quad (5.29)$$

Errors due to an uncertainty in the clamp location

The transition between the part of the microtubule that is clamped and the free part could be analysed best by observing thermal fluctuations near the seed by looking at the real time microscope images at 25 frames/s. A superposition of all digitised shapes was used in addition. The point where no transverse motion is observed is designated as $s = 0$ with an uncertainty of approximately $0.5 \mu\text{m}$. Choosing the transition point on the seed, a distance ΔL away from the real transition point leads to an effective overestimation of the filament length L . According to Eq. 5.16 this causes an underestimation of the mode amplitude by a factor of $L/(L+\Delta L)$ and by Eq. 5.25 this leads to a total overestimation of the persistence length by a factor of $((L+\Delta L)/L)^5$. Underestimation of the filament length introduces an underestimation equal to $((L-\Delta L)/L)^5$. If the length of the analysed-part of the microtubule equals $30 \mu\text{m}$, the uncertainty in the exact location of the transition point introduces a maximal error of 10%.

Digitisation noise

For the calculation of mode amplitudes we made use of a digitised version of the microtubule shape which consists of approximately 600 values for the path length s and the perpendicular coordinate y . Errors in the path length determination were dominated by the uncertainty in the designation of $s = 0$. The image processing routine determines values for y and made errors on the order of 100 nm. Due to the large amount of points used in the calculation of the mode amplitudes, using a discrete version of Eq. 5.16, digitisation errors average out to a large degree. A complete treatment of digitalisation noise is given by Gittes *et al.* [10]. Because our analysis is based on the y -coordinate instead of θ , we had to change the analysis slightly. The absolute error introduced can be shown to be small and mode number independent influencing only high mode numbers.

Another source of errors is sample drift. During the observation time the sample drifted slowly under our microscope. We corrected for this by tracking the position of a fixed point in the sample. Nonetheless some remaining motion caused additional variance of the mode amplitudes. The effect of this motion on mode amplitudes was relatively small compared to thermal amplitudes for the lower mode numbers.

Clamping at $s = 0$

The solutions of the equation of motion for the full-length microtubule, Eq. 5.4, are only valid for the assumed boundary conditions. The condition of a free end at $s = \lambda L$ is fulfilled by definition, however, the quality of the clamp at $s = 0$ needed to be investigated. Small rotations around the clamp during the course of an experiment will give rise to additional variance in the measured mode amplitudes and lead to an

Rigidity measurements on growing microtubules

underestimation of L_p . For small angles of rotation, α , a rotated microtubule may be described as $y_{rot}(s) = s \cdot \sin(\alpha)$, which can be projected on the functions $W_l(s/L)$ to obtain the induced mode amplitudes $\tilde{a}_{l,rot}$. In this way, one can show that the variance in $\tilde{a}_{l,rot}$ caused by rotational diffusion around the clamp scales as q_l^{-4} just as the variances caused by thermal deflections do. We can thus not rule out rotational diffusion by checking the mode number dependency of the measured mode amplitudes. Cross correlations between modes might be used to differentiate, but due to their stochastic nature this is problematic.

Instead of looking at the variance per mode one can look at the total variance in the positional coordinate y at a fixed value for the path length s . Motion governed mainly by rotational diffusion would show a quadratic dependency on s ,

$$\text{var}(y_{rot}) = s^2 \text{var}(\sin \alpha) \approx s^2 \text{var}(\alpha). \quad (5.30)$$

A cubic s -dependency [2] is expected for thermally induced fluctuations

$$\text{var}(y_{bend}) = \frac{s^3}{3L_p}. \quad (5.31)$$

Observations of bending on a perfectly clamped seed should thus obey a cubic s -dependence. Eq. 5.31 is a direct result of equipartition theorem but can also be calculated using our mode analysis. Therefore we take the analysed length L equal to s and using Eq. 5.15 and Eq. 5.21 we find

$$\text{var}(\tilde{y}) = \frac{1}{s} \sum_{l=1}^{\infty} \tilde{\sigma}_l^2 W_l^2(1) = \frac{s^3}{L_p} \sum_{l=1}^{\infty} 4q_l^{-4}. \quad (5.32)$$

The converging sum can be computed numerically and equals 1/3 reproducing the direct result of Eq. 5.31. This again shows that Eq. 5.21 correctly predicts the fluctuations of the analysed-length modes.

Errors induced by background flow

Small flows of liquid in the sample may cause a hydrodynamic drag on the microtubule, which will cause non-thermal bending [2,84]. Care has been taken in our experiment to prevent currents due to evaporation of fluid by closure of the sample at all sides.

We tried to estimate the effect of flow on mode amplitudes. A uniform flow with velocity v_{flow} in a direction perpendicular to the relaxed shape will induce bending [86] which can be calculated in the small angle limit,

$$y_{flow} = \frac{\pi \eta v_{flow} (\lambda L)^4}{6 \kappa \ln(\lambda L / 2D)} \left(\left(\frac{s}{\lambda L} \right)^4 - 4 \left(\frac{s}{\lambda L} \right)^3 + 6 \left(\frac{s}{\lambda L} \right)^2 \right). \quad (5.33)$$

Chapter 5

We can project this shape on the functions $W_l(s/L)$ to obtain the induced mode amplitudes $\tilde{a}_{l, flow}$. The variance in these mode amplitudes caused by a variance in v , can be calculated to roughly follow a q_l^{-10} dependency. Although currents occurring in the sample are not necessarily uniform it is clear that they will not reproduce a q_l^{-4} dependency as in Eq. 5.21.

5.3 Results

Sample characterisation

We studied microtubule rigidity under two different growth-conditions. Conditions were chosen to mimic the two growth-conditions used in the buckling experiments of chapter 3 and 4, where samples with and without an oxygen scavenging system were used. In chapter 3 we observed that the addition of an OXS-system did not change microtubule growth velocity and catastrophe rate, however there might be an effect on rigidity. Previously, it was suggested that disulphide-reducing agents like dithiothreitol (DTT), a constituent of our OXS-system, may have an effect on microtubule rigidity [84]. To check for a possible effect, we measured rigidity with and without added OXS-system at almost the same tubulin concentration. We measured rigidity at $C_T = 28 \mu\text{M}$ with OXS-system (3 samples) and at $C_T = 26 \mu\text{M}$ without OXS-system (1 sample). Surprisingly, we found a significantly different average growth velocity of respectively $2.77 \pm 0.08 \mu\text{m}/\text{min}$ (mean \pm SEM) and $1.80 \pm 0.13 \mu\text{m}/\text{min}$. We think that we lost some control over the tubulin concentration when we decreased the height of our flow cell to a very low value of $1 \mu\text{m}$. Errors may have been introduced if some parts of the flow cell were not flushed with tubulin during the final step of the sample preparation. Therefore, we will compare our samples on the basis of the observed velocities and not on the assumed tubulin concentrations. Catastrophes were very rare under both conditions and most microtubules grew up to lengths exceeding $60 \mu\text{m}$ without undergoing catastrophes. Microtubule length was measured with respect to the end of the seed. In most cases observation was started at a microtubule length of approximately $30 \mu\text{m}$ and observation was stopped after 10 to 15 minutes or earlier when a catastrophe occurred. During this time the microtubule had grown out of the field of view of the set-up (35 by $26 \mu\text{m}$) and directly after the observation time an estimate was made of the total length of the microtubule. For this, we moved the microscope stage to move the growing tip into the field of view. Only microtubules that remained shorter than $60 \mu\text{m}$ were used in this study. Once every 6 seconds a frame was captured and the shape of the microtubule was digitised. The microtubule did not move out of the plane of focus because the sample chamber had a thickness of only $1 \mu\text{m}$. Image quality was good enough for automated microtubule shape digitisation of almost all grabbed images. Some microtubules were pinned at a single point along their length during part of the total observation time. Note that pinning involves temporarily non-specific bonding between a microtubule and the surface, which is

Rigidity measurements on growing microtubules

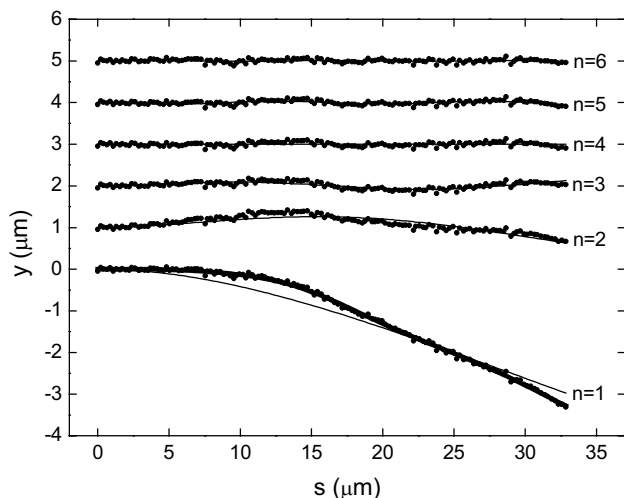


Figure 5.6 Raw digitised points are plotted that represent the shape of a microtubule ($C_T = 28 \mu\text{M}$ with OXS-system) at a certain time point (lower curve). Only 25 % of all digitised points are plotted for clarity. Overlaid on the raw data is a reconstituted shape based on the first five modes calculated with Eq. 5.15 (thick line) plus the shape of the first mode only (thin line). The shape of the 2nd until 6th mode is plotted with an increasing offset equal to a multiple of $1 \mu\text{m}$ (thin lines). For each mode n larger than 1, the raw data points with mode functions 1 until $n-1$ subtracted are overlaid.

different from the specific clamping of the seed. Pinning constrains thermal motion and these microtubules were not analysed. A few microtubules had a large intrinsic curvature and were not analysed. Growing minus ends, identified by a slow growth rate were not analysed. In total seven out of twelve observed plus-end microtubules were analysed with OXS-system and five out of five without OXS system.

Mode analysis

The part of the microtubule that was analysed was chosen around $30 \mu\text{m}$ and mode amplitudes were calculated for each time point, using a discrete version of Eq. 5.16. With Eq. 5.15 we could reconstitute the shape of a digitised frame using only the first five modes (Fig. 5.6). The first six mode functions were multiplied with the calculated mode amplitude and are plotted separately. Subsequently, these modes were subtracted from the data points to show the residual shape fluctuations. The fifth mode is overlaid with data points from which the first four modes were subtracted. There is still some undulation in this data and the fifth mode thus represents true thermal fluctuations. In this case the 6th mode seems to describe only digitisation noise.

For one fluctuating microtubule the analysed mode amplitudes, \tilde{a}_i , are shown as a function of time (Fig. 5.7). As expected on theoretical grounds the correlation time of the

Chapter 5

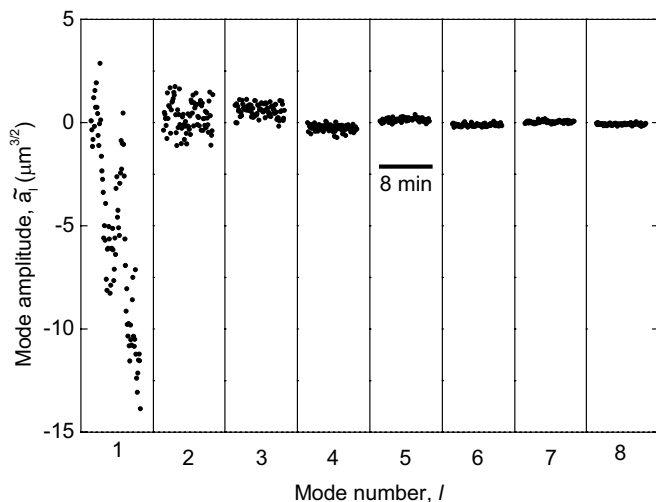


Figure 5.7 Calculated mode amplitudes, \tilde{a}_l , for a microtubule ($C_T = 28 \mu\text{M}$ with OXS-system) with an analysed-length of $34.3 \mu\text{m}$. Data are plotted as a function of time for the first eight mode numbers. The observation time was 8 minutes. The variance in the data points clearly becomes smaller as a function of the mode number l .

first mode is much larger than the sample time. Indicative is the clear trend that can be seen in the first mode data as a function of time. Such trends are not observable for higher modes and individual time points seem statistically independent of each other. Higher modes are thus not dictated by the slow first full-length mode.

In order to test the inverse 4th power dependence of the measured variance on q_l as predicted by Eq. 5.21, the measured variance of the mode amplitudes, \tilde{a}_l , multiplied by L^{-4} was plotted as a function of q_l for both growth conditions (Fig. 5.8). According to Eq. 5.21 this quantity should be length independent and equal $L_p^{-1} q_l^{-4}$. Within one single growth condition, the 2nd until the 5th mode values all lay on the same straight line. This indicates that there are no large differences in persistence length between the analysed microtubules within one growth-condition. The variance in the 1st mode amplitude is smaller than expected because our observation time is too short relative to the correlation time of the 1st full-length mode τ_l . 6th order and higher modes have variances larger than expected, which is caused by digitisation noise as is discussed in the methods section.

Rigidity measurements on growing microtubules

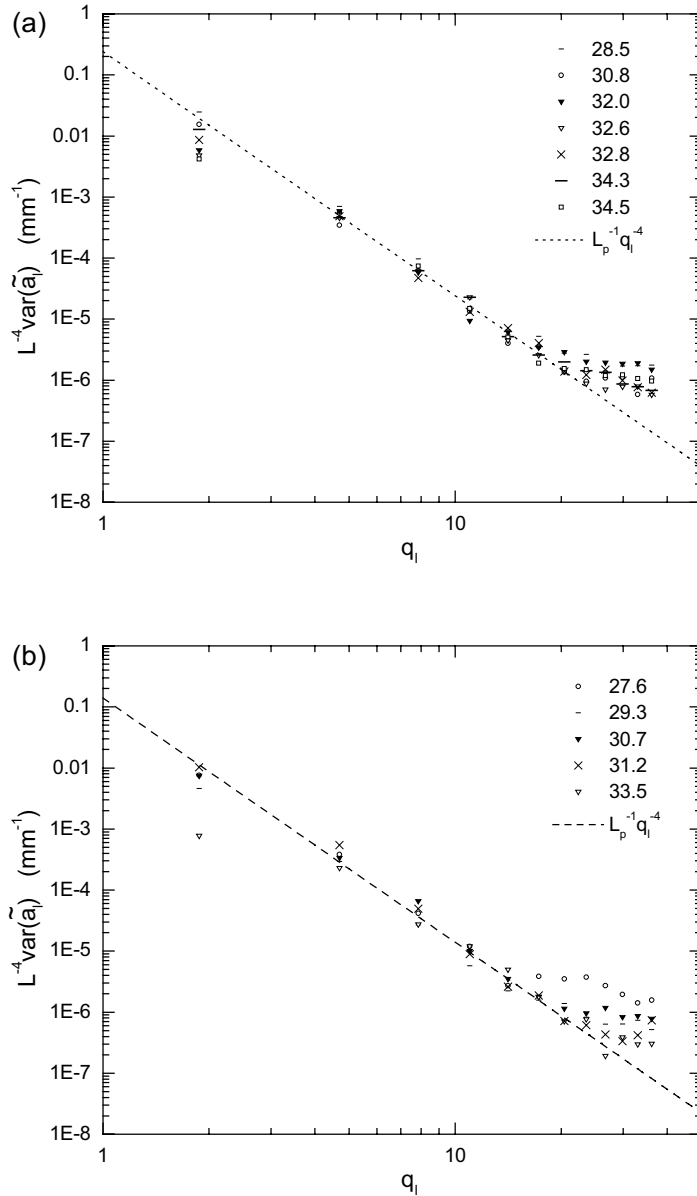


Figure 5.8 Variance of the measured mode amplitudes, \tilde{a}_l , multiplied by L^4 as a function of q_l . The theoretical expectation, $L_p^{-1} q_l^{-4}$, is plotted for our final estimate of the persistence length (table 5.1). The length of the analysed-part of the eight microtubules is given in the legend. (a) $C_T = 28 \mu\text{M}$ with OXS-system. (b) $C_T = 26 \mu\text{M}$ without OXS-system.

Chapter 5

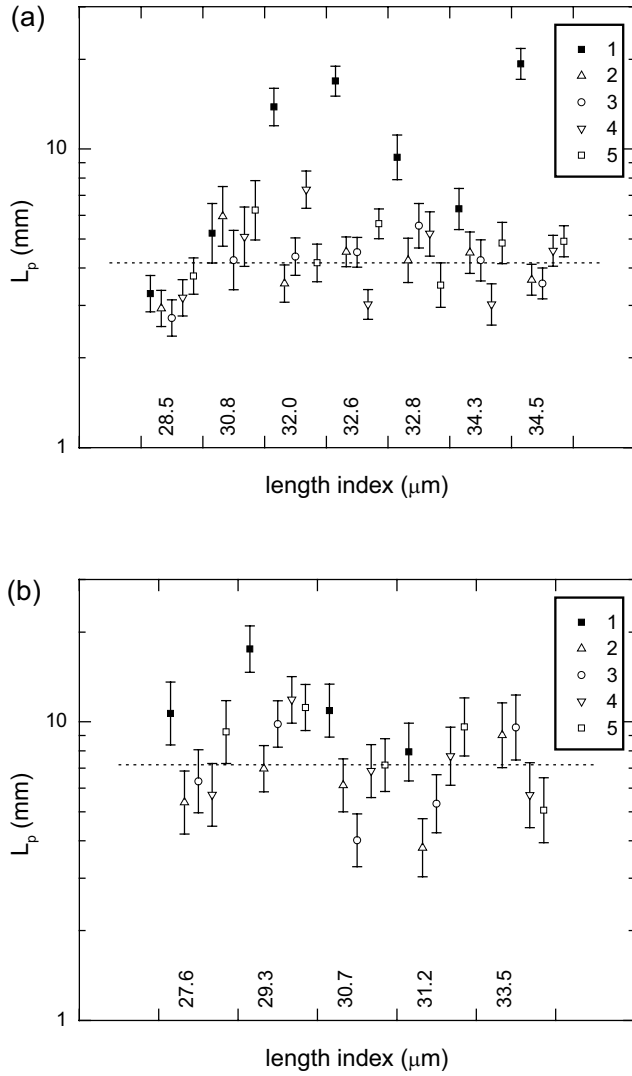


Figure 5.9 Estimates for the persistence length based on the first five modes are plotted in order of increasing filament length. Standard deviations calculated by Eq. 5.29 are plotted as error bars. The straight line corresponds to our final estimate of the persistence length.(table 5.1). **(a)** $C_T = 28 \mu\text{M}$ with OXS-system. **(b)** $C_T = 26 \mu\text{M}$ without OXS-system. The 1st mode persistence length estimate for the microtubule with length $33.5 \mu\text{m}$ does not fit on the scale, but equals 104 mm .

Rigidity measurements on growing microtubules

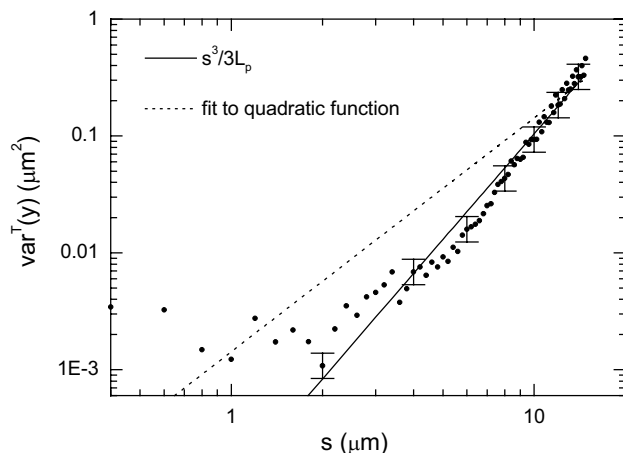


Figure 5.10 Variance in the positional coordinate y along a growing microtubule ($C_T = 28 \mu\text{M}$ with OXS-system) as a function of path length s . Each point represents an estimate over 33 time-points. An error bar is plotted for seven points representing the standard deviation on the variance. Within the observation time the microtubule grew from 15 to 25 μm . Variance predicted by thermal bending (Eq. 5.31 using our final estimate of L_p for this growth condition) is plotted over the data as well as is a quadratic fit to the data (based on Eq. 5.30).

In Fig. 5.9 we plotted for every analysed microtubule 5 estimates for the persistence length based on mode numbers 1 till 5. The weighted average of all 1st mode estimates per growth-condition was calculated as was done for the 2nd until 6th mode (see table 1). Due to the short observation time, the two estimates based on the 1st mode are clearly too large. We based our final persistence length estimates for the two studied conditions on modes 2 till 5. Sixth order and higher modes were not used because the influence of digitisation noise becomes pronounced which leads to an underestimation of the persistence length. For $C_T = 28 \mu\text{M}$ with OXS-system we found $L_p = 4.2 \pm 0.1 \mu\text{m}$ (7 microtubules) and for $C_T = 26 \mu\text{M}$ without OXS-system $L_p = 7.2 \pm 0.4 \mu\text{m}$ (5 microtubules). To check whether microtubules within one single growth-condition have a constant rigidity, we calculated an individual persistence length value for each microtubule based on modes 2 till 5 (see table 2). For each growth condition the probability, P , was calculated that the individual estimates could be drawn out of a homogeneous parent distribution using a χ^2 test. For the two conditions we found $P < 0.001$ (28 μM) and $P < 0.01$ (26 μM). The errors, which are tabulated in table 1 and 2, are statistical errors and were not corrected for systematic errors. If we increase all standard errors by 5% of the persistence length to roughly account for errors introduced by an uncertainty in the clamp location we find $P = 0.12$ (28 μM) and $P = 0.17$ (26 μM). These probabilities are both small and we cannot rule out that there are differences in rigidity between individual microtubules within one growth-condition.

Chapter 5

Mode number	L_p' (mm), $v = 2.77 \pm 0.08 \mu\text{m}/\text{min}$	L_p' (mm), $v = 1.80 \pm 0.13 \mu\text{m}/\text{min}$
1	28 μM Tubulin plus OXS system	26 μM Tubulin
1	10.4 ± 0.6 (7)	16.4 ± 1.7 (5)
2	3.9 ± 0.2 (7)	6.0 ± 0.6 (5)
3	4.0 ± 0.2 (7)	6.7 ± 0.7 (5)
4	4.1 ± 0.2 (7)	7.8 ± 0.8 (5)
5	4.6 ± 0.3 (7)	8.5 ± 0.9 (5)
6	3.8 ± 0.2 (7)	5.7 ± 0.6 (5)
2...5	4.2 ± 0.1 (28)	7.2 ± 0.4 (20)

Table 5.1 Persistence length estimates per mode. For each condition studied, the average of all 1st mode estimates is shown (mean \pm uncertainty of the mean). The number of values averaged is indicated in parentheses. Similar values were calculated for mode 2 until 6. The 2nd until 5th mode were used for our final persistence length estimate. Microtubule growth velocity, v , is indicated for both growth conditions.

28 μM Tubulin + OXS system		26 μM Tubulin	
$v = 2.77 \pm 0.08 \mu\text{m}/\text{min}$		$v = 1.80 \pm 0.13 \mu\text{m}/\text{min}$	
MT length (μm)	$L_{p,2..5}'$ (mm)	MT length (μm)	$L_{p,2..5}'$ (mm)
28.5	3.1 ± 0.2	27.6	6.5 ± 0.8
30.8	5.3 ± 0.6	29.3	9.8 ± 0.9
32.0	4.7 ± 0.3	30.7	5.9 ± 0.6
32.6	4.3 ± 0.3	31.2	6.2 ± 0.7
32.8	4.5 ± 0.4	33.5	7.1 ± 0.9
34.3	4.1 ± 0.3		
34.5	4.1 ± 0.3		

Table 5.2 Persistence length estimates per microtubule for the 12 (7 + 5) studied microtubules subdivided per experimental condition. The 2nd until 5th mode estimate of the persistence length were averaged for every microtubule (mean \pm uncertainty of the mean).

Rigidity measurements on growing microtubules

Quality of the clamp

One growing microtubule was analysed while its length increased from 15 to 25 μm . For this maximum length the fluctuation time τ_1 does not exceed the sampling time and observed shapes are completely statistically independent. The part between $s = 0$ and $s = 15 \mu\text{m}$ was subdivided into 75 equally sized parts of which the positional coordinate y was estimated out of the digitised curves. The variance of y is well described by Eq. 5.31 (see Fig. 5.10). Deviations are caused by digitisation noise which is, for small values of s , relatively large compared to thermal variance. Also uncertainty in the exact position of the clamp causes errors. A quadratic dependency as expected for rotational diffusion by Eq. 5.30, fits the data very poorly. From this we conclude that the biotin-streptavidin bond generates a good clamp.

5.4 Discussion

We used the cantilevered beam configuration to experimentally estimate the persistence length of a microtubule using thermal fluctuations. We chose conditions as temperature and tubulin concentration such that they mimic the experimental conditions under which we measure assembly forces in a separate experiment. For these conditions microtubules grow relatively fast (2 $\mu\text{m}/\text{min}$) and microtubules cannot be considered constant in length during the time that is required to obtain sufficient statistics over the thermal fluctuations.

Thermal fluctuations can best be analysed using a mode analysis, which was first introduced for stabilised microtubules with both ends free [10]. We extended this method and made it applicable to microtubules that are clamped at one side and grow at the other side. The main advantage of the chosen approach is that we can now study microtubule rigidity of non-stabilised microtubules using a mode analysis. Furthermore, clamping prevents the microtubules from longitudinal rotation. Rotation of microtubules with an intrinsic curvature caused additional shape fluctuations in the non-clamped configuration [10]. Torsion of microtubules does not generate errors [10]. To make the mode analysis work in the clamped configuration we only analysed shape fluctuations of the first part of the growing microtubule. We project this analysed-length on to a set of orthonormal functions. The functions used are the solutions of the equation of motion for a full-length microtubule with one free end and one clamped end. We thus pretended that the analysed part has a free end and later checked what kinds of errors were introduced. The variance in the mode amplitudes does not depend on the total length of the microtubule and growth during observation is thus not a problem (Eq. 5.21).

Slow fluctuations

The advantages of the mode analysis are exploited maximally if long microtubules are observed. For these long microtubules amplitudes of more modes are large enough to be detectable [10]. The dynamics of thermal shape fluctuations is considerably slower in the

Chapter 5

clamped configuration compared to the completely free situation, which becomes problematic for long microtubules. We calculated the correlation time of full-length modes that describe the true dynamics of the system and checked how they influence our analysed modes. Individual microtubules used in this study had a maximum length of 60 μm of which approximately 30 μm was analysed. For these microtubules, the correlation time of the 1st full-length mode is on the order of many minutes and the correlation time of the 2nd and higher modes is comparable or smaller than the sampling time of 6 seconds. Experimentally we observed these slow 1st mode fluctuations, which could not be sampled completely within our observation time of approximately 10 minutes. Slow fluctuations caused an overestimation of the persistence length when its calculation was based on the first analysed mode only (Table 1). Measuring fluctuations of the tip of a microtubule [76,84,86] comes down to probing the dynamics of the 1st mode and can lead to similar errors if long microtubules are used. Theoretically and experimentally we showed that 2nd and higher analysed mode amplitudes are hardly affected by the slow fluctuation of the 1st full-length mode. The 2nd mode estimate of the persistence length agrees within the statistical error with the overall estimate (Table 1), which indicates that the systematic error caused by a limited observation time does not dominate.

Sample digitisation

We used image analysis methods for the digitisation of the microtubule shape, which yielded about 600 points per microtubule shapes. Approximately 10 points, obtained with manual methods, were used for mode calculations in earlier work [10,85]. As a result we could observe fluctuations of the first five modes whereas earlier, digitisation noise limited the number of visible modes to one [85] or two [10] for approximately 30 μm long microtubules. By averaging over more modes we obtained better statistics on our rigidity estimate. Averaging was allowed because our analysis showed that persistence length estimates based on different modes are statistically independent.

Fast correlation times

We discussed errors introduced by slow correlation times, but fast correlation times also introduce errors. Fluctuations with a correlation time faster than the image acquisition time of 40 ms will appear smoothed on the digitised images. An average microtubule in our experiment has a length of 45 μm of which approximately 30 μm is analysed. This situation corresponds to $\lambda = 1.5$ in Fig. 5.4a. The 6th full-length mode, with $\tau_6 = 17.6$ ms, contributes strongly to the 4th analysed mode. We might thus expect a measured variance in the 4th and higher analysed-modes that is lower than predicted by Eq. 5.21. The measured data presented in Fig. 5.8, however, seems to follow the q_l^{-4} law up to $l = 5$. Around $l = 5$ the variance is generated by a complex combination of thermal bending, digitisation noise and smoothing, which might mimic the inverse 4th power law. Furthermore, the calculation of the correlation time is based on a rough estimate of the

Rigidity measurements on growing microtubules

perpendicular drag coefficient γ and might be underestimated which makes fluctuations slower than expected. It is therefore hard to tell how well Eq. 5.5 predicts the correlation time. Some evidence for mode smoothing is obtained from table 5.1, where the 5th mode persistence length estimate looks significantly larger than the 2nd until 4th mode estimate for both growth conditions. More data is needed to test whether this is a real difference or just measurement noise. The equation of motion for an elastic rod can be extended with a term representing internal friction or flow of water through the pores of a filament [94]. Correlation times can be shown to become mode number independent for higher mode numbers if this term has a significant contribution. It would be interesting to see whether or not such effects occur. For this one should try to lower the digitisation noise, which is caused by sample drift and limited image quality. The first cause can be easily minimised by using a stabilised microscope stage. Finally, we note that the use of cosine functions in the cantilevered beam set-up [85] makes the analysed modes dependent on higher full-length modes (see Fig. 5.4b). Application of these functions would have made the correlation times of analysed modes even more unpredictable.

Sources of error

Apart from possible fast correlation times, our rigidity measurement is affected by four main sources of errors. The statistical error due to a finite number of estimates of the mode amplitudes, errors introduced by the slow 1st mode fluctuation, errors caused by digitisation noise and errors introduced by uncertainty in the exact location of the clamp. The effects of important systematic errors, clamp location and slow fluctuations, were roughly quantified and are approximately equal to the statistical error. Digitisation noise is only a problem at the higher mode numbers, which were not used in our final rigidity analysis, except for the 5th mode that might have been influenced slightly. Additional errors could, but were not introduced by fluid flow in the sample and by fluctuations in the direction of clamping. The analysis of the 2nd until 5th all yielded a similar value for the rigidity. This shows that we did not have large bending contributions due to fluid flow and that the microtubule can be described as an elastic rod. The direction of clamping was shown to be constant.

Chapter 5

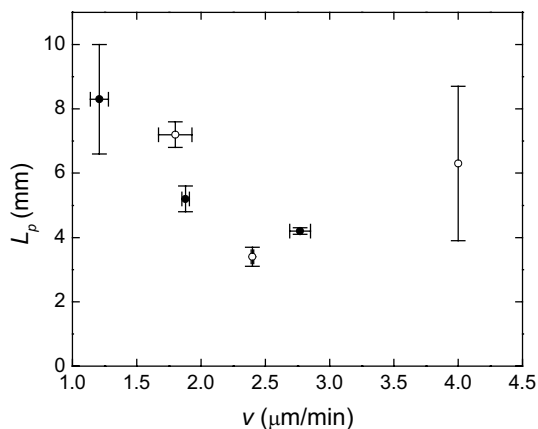


Figure 5.11 Persistence length estimates for six different growth-conditions versus average growth velocity (see table 5.3). Standard errors are plotted for the velocity and standard deviations for L_p . Growth conditions with added OXS-system are plotted as closed symbols and without OXS-system as open symbols. The data at 4 $\mu\text{m}/\text{min}$ are taken from Fygenon *et al.* [92] and were measured under different buffer conditions while microtubules were generating forces when entrapped inside lipid vesicles.

Rigidity estimates

We have measured microtubule rigidity under two growth-conditions and found significantly different values for the average L_p (table 5.1). The conditions differ both in the average growth velocity and in the presence of the oxygen scavenging system. Both these differences may have caused a rigidity difference. Because of the effect of growth-conditions, it is dangerous to measure rigidity in one sample and use this value for the calibration of force measurements in another sample (chapter 3). In chapter 3 we described an effort to derive microtubule rigidity from the microtubules observed in the samples with buckling microtubules. The method outlined here could not be used because the microtubules that were recorded on tape were short and often were only partially in focus because of Brownian motion. Therefore we used a less precise method that is often used in the literature that makes use of thermal fluctuations of one single point of the microtubule. Eq. 5.31 was used to obtain rigidity values. In the literature we found two rigidity measurements [47,92] on growing microtubule together with a documented value for the growth velocity. Values from Fygenon *et al.* [92] were measured under different buffer conditions while microtubules were generating forces when entrapped inside lipid vesicles. All available measurements are summarised in table 5.3 and Fig. 5.11.

Rigidity measurements on growing microtubules

Source	Temperature (°C)	OXS-system	Growth velocity \pm SEM ($\mu\text{m}/\text{min}$)	L_p (mm)
this chapter ⁽¹⁾	23	yes	2.77 ± 0.08	4.2 ± 0.1
this chapter ⁽¹⁾	23	no	1.80 ± 0.13	7.2 ± 0.4
chapter 3 ⁽²⁾	23	yes	1.88 ± 0.03	5.2 ± 0.4
chapter 3 ⁽²⁾	23	no	2.40 ± 0.01	3.4 ± 0.3
Dogterom <i>et al.</i> ⁽³⁾	22	yes	1.21 ± 0.07	8.3 ± 1.7
Fyngenson <i>et al.</i> ⁽⁴⁾	30	no	≈ 4	6.3 ± 2.4

Table 5.3 Summarised persistence length estimates for five different growth-conditions. Methods that were used were: ⁽¹⁾ a mode analysis of thermal fluctuations as outlined in this chapter. ⁽²⁾ a one point analysis of thermal fluctuations outlined in chapter 3. ⁽³⁾ a two point analysis of thermal fluctuations [47]. ⁽⁴⁾ entrapment of microtubules inside vesicles [92]. The OXS-systems used in different studies was equal.

There is no clear separation in rigidity between measurements done with and without an OXS-system, but there seems to be an effect of growth velocity on microtubule rigidity. Slower growing microtubules appear to be stiffer. The underlying mechanism is puzzling. The number of protofilaments inside a microtubule varies between 10 and 16, but values of 12,13 or 14 are by far the most observed [72]. If a microtubule is modelled by a homogeneous rod, one can show that the rigidity difference between a 13 and 14 filament microtubule should be 20 % [10]. Although this can explain rigidity variations observed within one single growth-condition it cannot explain differences between growth-conditions. Microtubules observed by Dogterom *et al.* at $1.2 \mu\text{m}/\text{min}$ [47] should therefore have consisted entirely out of 14 protofilaments whereas microtubules at approximately $2.5 \mu\text{m}/\text{min}$ must consist out of entirely 12 protofilaments, which is unlikely. Transitions between different types of lattices and protofilament numbers were observed within individual microtubules [72]. If transition areas correspond to spots with a lowered rigidity we might only be able to measure an average rigidity value for a microtubule. The transition areas should not be seen as very weak links, because such a freely jointed chain would not give rise to the observed q^{-4} dependency of the mode variance [10]. If the spatial frequency of such transitions is high and growth velocity dependent they might explain our data. Reported frequencies observed with electron microscopy range from 0.08 transitions per micrometer, averaged over many microtubules, [95] to $2 \mu\text{m}^{-1}$ on one individual microtubule [72]. A mechanism based on defects is therefore very speculative and we should first expand our observations with more experiments at several growth velocities using the approach to rigidity measurements outlined above. For our buckling experiments we decided to use the rigidity measurements that were done with a less

Chapter 5

precise method for the reason that they were made in the same sample as the force generation experiments

Our final estimates fall within the range of published persistence lengths for non-stabilised microtubules grown from GTP-tubulin, 0.91-8.3 μm [47,76,84-88,92]. We included here reports for microtubules that were stabilised with small GMPCPP-tubulin caps at their ends [84]. Quantitative comparisons are difficult because different methods were used all having different degrees of systematic errors. Furthermore different growth conditions might have altered rigidities as suggested by this study. Passive methods that are based on thermal fluctuations suffer in general to a lesser degree from systematic errors and should give more reliable values than active methods. A mode analysis of thermal fluctuations allows for an internal consistency check of the method. We extended this method so that it can be applied to long growing microtubules and carefully checked the time scale on which the microtubules fluctuate. Therefore we now have access to an accurate analysis that can be used to measure microtubule rigidity under many conditions.

5.5 Acknowledgements

I would like to thank Cătălin Tănase and Marco Consentino-Lagomarsino for helpful discussions and numerical calculations and Yvette de Natris for her initial work on microtubule rigidity.

VI

Final considerations and new research directions

We have characterised in chapter 3 and 4 how the growth velocity and the catastrophe rate of a microtubule are changed when a force opposes microtubule assembly. As shown, we can extract valuable information about rate constants and the assembly process in general from our observations. In this chapter we describe an optical-tweezers-based set-up with which we can probe the assembly process at a higher temporal and spatial resolution. One of the parameters we hope to measure is the force that stalls a microtubule. Studying single growing microtubules that push against non-specific barriers can be seen as a first important step to understand assembly-aided force generation inside living cells. In cells, microtubule dynamics is however clearly regulated by other proteins, and new experiments are needed to understand the molecular mechanisms behind regulation and the effect of regulation on force generation. Some first results in this direction will be discussed in this chapter as well. Finally, we discuss some aspects of the mechanism behind dynamic instability related to our experimental results.

6.1 Probing microtubule dynamics with optical tweezers

In order to measure forces generated by microtubule assembly, we used in chapter 3 and 4 the buckling of microtubules as a force probe. This experimental set-up has been shown to have some drawbacks. First, a certain degree of chance determines what happens, i.e. a randomly deposited seed should nucleate a microtubule which grows in a perpendicular way towards the barrier and upon touching the barrier should not start sliding nor grow over the barrier. Secondly, the rigidity of the microtubule under study should be known precisely in order to calibrate forces. Errors in the force measurement are generated if the point of barrier contact and the location of the seed are not found correctly by fitting (see

Chapter 6

chapter 2) or if the microtubule is not intrinsically straight. Thirdly, microtubule force generation is difficult to study at a large load, because force does induce a catastrophe on the time scale of 20 seconds. In this time the microtubule hardly grows or buckles because the growth velocity decreases significantly under load. Forces cannot be measured if buckling is not observed. To circumvent these problems we propose an alternative method based on optical tweezers with which we hope to measure assembly forces and supplement out knowledge about force generation and microtubule dynamics. Optical tweezers are a relatively new tool in biology, which were for example used to visualise individual steps made by motor proteins along microtubules [4].

Optical tweezers are used to measure forces applied on small particles suspended in liquid. A tweezers set-up is constructed by focussing a parallel laser beam through the objective lens of a microscope in the focal plane. The tight laser focus created has a remarkable effect on small suspended particles such as glass beads with a diameter of about a micron. If the index of refraction of the bead differs from the liquid then the momentum change of the laser light upon refraction is compensated such that the particle is pushed towards the laser focus. The bead can become trapped in three dimensions in a tightly focused beam [90,96]. Depending on the light intensity and index of refraction mismatch, forces in the piconewton range are needed to pull the bead out of the tweezers [97]. The force that retracts the particle towards the middle of the trap can be shown to depend linearly on the displacement out of the trap centre over a range of approximately 150 nm [97]. Displacement in the focal plane can be measured with nanometer accuracy by essentially imaging the trapped particle onto a quadrant photodiode [97], i.e. four light sensitive elements arranged in a 2×2 matrix. Displacement corresponds to a change in light refraction, which can be measured by the diodes with a sub-millisecond time resolution.

Experiments on the nanometer / millisecond scale

In principal we could try to let a microtubule push against a optical-trapped micron-sized glass bead and measure assembly forces from the bead displacement. A microtubule is however likely to loose contact with the small bead and therefore we propose the set-up as is depicted in Fig. 6.1. A bead with a strong affinity to microtubules is trapped and positioned on the end of a long growing microtubule nucleated by a surface-connected seed. By moving the microscope stage or the laser focus, we can move the sample relative to the location of the trap. The microtubule can now be bend in such a way that the end is located close to a barrier pointing in a perpendicular direction towards it. The force that is needed will cause the bead to have a new equilibrium position inside the trap. Note that the direction of growth can be controlled because the microtubule is connected to a surface-connected seed. In an earlier experiment we used an extra bead attached to a free microtubule to control the direction with a second trap [54]. The configuration described here seems to be easier to achieve experimentally. After a short period of growth the

Final considerations and new research directions

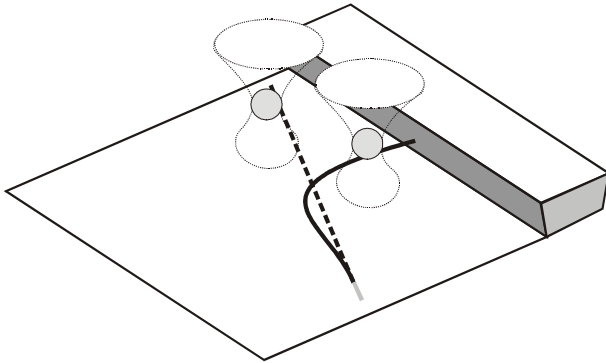


Figure 6.1 Schematic view of the optical tweezers based set-up. A microtubule (dashed line) is nucleated from a surface attached seed (grey area). Using optical tweezers (represented as a cone of light) a bead is trapped and positioned next to the growing microtubule within $2\ \mu\text{m}$ from the tip. The bead binds to the microtubule and is manipulated such that its growing tip encounters a barrier.

microtubule will reach the barrier and will push the bead out the new equilibrium position. The displacement can be used to measure growth velocity and force. The microtubule will not buckle if the distance between trap and barrier is kept smaller than a few microns. A number of experiments should be feasible with this set-up:

Measurement of the stall force. As the microtubule grows the trap will increase its opposing force until the stall force is reached for which the assembly rate at the tip equals the disassembly rate (Eq. 1.9). In the buckling experiment this force could not be estimated precisely (see chapter 4), whereas here the maximum force is obtained directly from the maximum displacement.

Force-velocity measurements under constant load. The opposing force can be kept constant during microtubule growth by a feedback mechanism that moves the barrier in nanometer sized steps using a controllable piezoelectric microscope stage. It will be interesting to see what kinds of growth fluctuations occur at the nano-meter / millisecond scale. GTP-hydrolysis of tubulin dimers at the tip or fluctuations in the length of a sheet structure at the tip may cause velocity fluctuations over short time scales. The question is whether or not the system will be able to probe these subtle differences.

Catastrophe rate measurements. As shown in chapter 4, the catastrophe rate will increase at low velocities of growth. With the light microscope it is very difficult to measure microtubule dynamic instability on free microtubules at low growth velocities ($\approx 0.2\ \mu\text{m}/\text{min}$), because high catastrophe rates limit the length of microtubules to approximately the spatial resolution of the microscope ($\approx 0.5\ \mu\text{m}$). By using high load forces or low tubulin concentrations, we should be able to measure in a velocity range that was previously hardly- or in-accessible [11,19,55]. Models describing catastrophes

Chapter 6

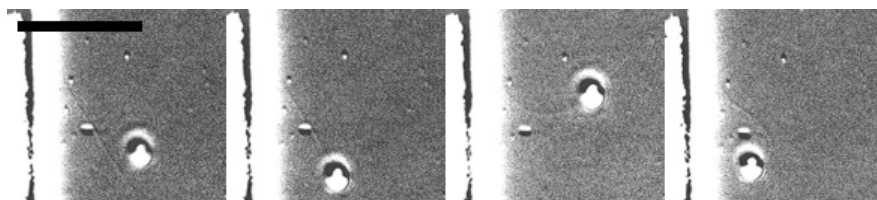


Figure 6.2 A series of DIC microscopy images showing from left to right: a free growing microtubule nucleated by a seed together with a trapped bead, attachment of the bead to the microtubule and microtubule manipulation. The barrier is at the left of each frame, but its exact position can be observed poorly. The black vertical line is a good indication. The scale bar equals 10 μm . Growth conditions were 15.3 μM tubulin in MRB80 with 0.51 mg/ml casein, 0.51 mM biotin and 1.53 mM GTP.

[18,58,98] can then be tested at high and low growth velocities. Free growing microtubules have been observed to exhibit pause states in which growth is apparently stopped [19]. Pauses have been suggested to correspond to microtubules with blunt end structures as observed by electron microscopy [59] and may be a transient state towards a catastrophe. Short pauses before a catastrophe occurs should be measurable with the optical tweezers.

Measuring rate of subunit removal k_{off} . In chapter 4 we presented measurements of catastrophe times of stalled microtubules for which the rate of subunit addition (on-rate) and removal (off-rate) were balanced by application of the stall force. Higher forces above the stall force should decrease the assembly rate below the rate of disassembly based on thermodynamic arguments (see section 1.3). A microtubule should therefore shrink at large forces with a rate governed by the off rate. This experiment may allow for a direct measurement of the off-rate but for studying the mechanism behind catastrophes it will also be interesting to see if the catastrophe rate can be decreased below the 24 seconds measured on stalled microtubules (chapter 4). Microtubule dilution experiments to zero tubulin concentration suggest that catastrophe times around 1 second are possible when the on-rate is completely decreased to zero [99].

Probing tip structure. If extended sheet structures as observed with electron microscopy [16] do indeed form at the tip of a growing microtubule this should give a different compressibility of the microtubule between bead and barrier compared to a microtubule with a blunt end. By the application of compressive forces we might thus be able to find evidence for sheets under dynamic conditions. The fluctuation spectrum of the bead is likely to change due to an extra compressibility.

First results

Because the outcome of the above experiments can give us the opportunity to test different hypotheses on microtubule dynamics, we believe that it is worth developing the described system. DIC images of a pilot experiment are shown in Fig. 6.2. They show that it is

Final considerations and new research directions

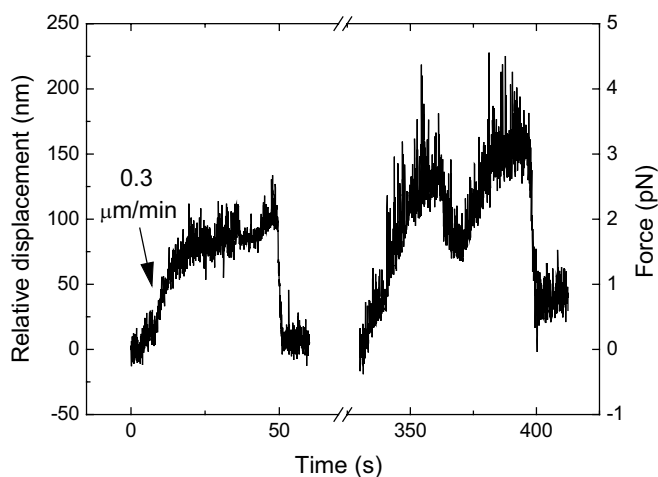


Figure 6.3 Results of two subsequent growth events nucleated by the same seed. The relative displacement of the bead was obtained from the recorded CCD images. The force (right axis) was calibrated with a trap stiffness of 0.02 pNm^{-1} .

possible to manipulate a microtubule in the envisaged way by connecting a bead to a growing microtubule. We used barriers like those used in chapter 3 and 4 but without an etched overhang. The experiment was set up in a flow cell similar to the one described in chapter 2. In the final step of preparation, we added silica beads with a strong affinity to microtubules and a diameter of $1.25 \mu\text{m}$.

The position of a trapped bead was not tracked yet with a quadrant photodiode, but was obtained from the DIC images with less but reasonable accuracy. Using an image convolution technique [100] the centre of a bead can be found from the images with sub-pixel resolution. Fig. 6.3. shows the recorded displacement after a microtubule struck the barrier in two successive growth events. In the first event, the microtubule was seen to push the bead out of the trap centre at a rate of $0.3 \mu\text{m}/\text{min}$. No good estimate of the free microtubule growth velocity was made in this sample but it is expected to be approximately $1 \mu\text{m}/\text{min}$ based on the tubulin concentration used. The microtubule stalls at a force of approximately 2 pN and has a catastrophe after 30 seconds, in good agreement with the 24 seconds reported in chapter 4. Similar behaviour is seen in the second event, but here the microtubule probably slipped along the barrier before stalling. Although we observed a very limited number of events so far and are not sure yet how to interpret all the observed length fluctuations, we do see similar behaviour as observed in chapter 3 and 4. Quantitatively we observed forces in the pN range but due to technical reasons we were not able to do a good force calibration of the optical trap under the same conditions as used for the experiment. The trap stiffness used in Fig 6.3 (0.02 pNm^{-1}) is

Chapter 6

inferred in an indirect way and therefore only indicative. In the final experiment, thermal fluctuations of a free bead will be analysed with the quadrant detector to measure trap-stiffness directly [101]. Preferentially we will use the same bead as used in the experiment. Problems that need to be solved include often breakage of the bond between bead and microtubule at high loads and the limited reproducibility of making these bonds.

6.2 Motor proteins as linking agents to growing microtubules tips

In chapter 3 and 4 we studied the effects of a growth opposing force on the two major parameters that describe microtubule dynamic instability, the growth velocity and the catastrophe rate. The experiments were done using microtubules grown from purified tubulin that were interacting with a glass barrier. In living cells, many proteins have been found that effect microtubule growth. Here we discuss some features of microtubule regulation to show part of the complexity of living cells. Regulatory proteins may have an effect on force generation and forces may change protein interactions. Therefore we think that force generation should be studied under biological relevant conditions in order to understand the complexity of motility inside living cells. We will present some efforts made towards this goal.

Regulation of microtubule dynamics

Microtubule regulatory proteins include so-called microtubule associated proteins (MAPS) as well as other proteins. Some have been shown to bind over the full length of microtubules and thereby increase growth velocity [55] and decrease the catastrophe rate [8,9]. Other proteins effect catastrophes by localising primarily to the plus ends of growing microtubules. Proteins like EB1 [102] and CLIP170 [77,103] stabilise whereas others like Op18 [104] increase the catastrophe rate. The mechanism used by these proteins to recognise the growing end and to control microtubule dynamics is not understood. Again different regulating proteins, like Dynein [41], or XKCM1 [105] are primarily located on specific microtubule binding sites in the cell like the kinetochores on chromosomes or protein complexes at the cortex of cells. These proteins bind to microtubules and regulate microtubule dynamics after the microtubule found a binding site by a search and capture mechanism [83].

Force generation by assembling microtubules in living cells occurs while they are attached to specific binding sites or when they non-specifically impinge on objects such as the arms of chromosomes [29]. The non-specific way resembles best our *in vitro* work with barriers. Reported observations from specific sites are very complex. Microtubules connected to kinetochores are observed to switch from growth to shrinkage and backwards while staying attached [24,29]. During these phases pulling and pushing forces are generated. Combined growth and shortening events are responsible for the construction of a well-aligned spindle, which is a prerequisite for accurate separation of chromosomes

Final considerations and new research directions

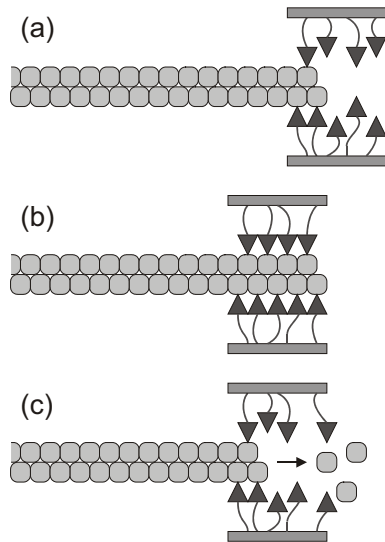


Figure 6.4 A model for directed motion driven by microtubule disassembly originally proposed by Hill for the kinetochore (adapted from [9,33]). The microtubule is schematically shown as a two-filament system on which coupling proteins (triangles) can attach or detach. A sleeve-like structure couples these proteins and models the kinetochore. The coupling proteins can diffuse along the lattice of the microtubule. The free energy of the system has decreased in going from (a) to (b) by the formation of more bonds. Because of their affinity, the microtubule wants to be in the sleeve created by the coupling proteins. Bonds between coupling-proteins and tubulin dimers are broken when attached dimers disassemble. (c). The ability of the sleeve to follow a disassembling microtubule depends on the rate at which coupling proteins can establish new contacts. This model describes the connection to a disassembling but not to an assembling microtubule. If the microtubule is in a state of growth, the sleeve can be positioned everywhere along the full length of the microtubule with equal probability. Loosely connected motor proteins that drive the sleeve towards the assembling end can, however, replace coupling proteins. The sleeve does not fall off the microtubule because motor proteins adjust their speed at the end or take over binding from neighbouring motors.

during cell division. To which extent proteins assembled on to the kinetochore regulate transitions in microtubule growth direction is under debate [26]. Our results as presented in chapter 3 and 4 show that the intrinsic microtubule properties give a regulatory effect of force on microtubule dynamics as well. It will be crucial to investigate the role of both regulatory pathways to fully understand the dynamics of the spindle. Other objects that anchor to the tip of growing or shrinking microtubules and that are likely to use the force generating properties of microtubules include phagosomes [106], cortical capture sites [41] and TAC complexes on the membrane of the endoplasmic reticulum [5,6].

Chapter 6

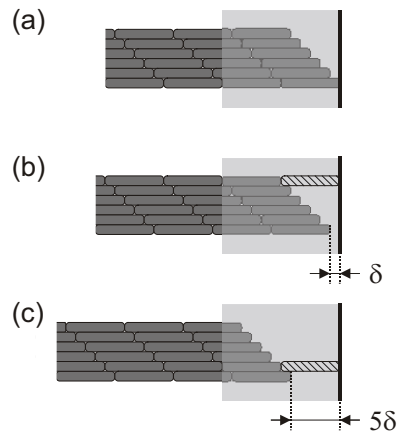


Figure 6.5 Upon binding a kinetochore, a microtubule will establish lateral contact. The microtubule is for simplicity represented as a six filament system and lateral contacts to the kinetochore are assumed to occur exclusively in the boxed area (grey). A barrier facing the tip (vertical black line) obstructs microtubule growth. Each protofilament in the initial situation (a) is allowed to grow. Two possible extensions are drawn in (b) and (c). The interaction area between microtubule and kinetochore remains constant in going from a to b, but is lowered significantly in going from a to c by which favourable interactions are lost. Microtubule growth can thus be coordinated to occur in an ordered manner with constant steps equal to δ , which is the average length increase per dimer addition.

Linking motion to assembling microtubules

A first intriguing question is how a dynamic microtubule tip can be linked to an object without losing its contact. Motor proteins are likely candidates for establishing this coupling because they make and break contacts with microtubules continuously. Motor proteins, which include Dynein [41] and CENP-E [107], have been shown to be bound to the kinetochore or have been suggested to be part of other microtubule binding complexes. These motor proteins may play a role in both linking and microtubule growth regulation. Hill [33] proposed a model for the connection between a microtubule and a kinetochore based on affinity concepts. This model was used to describe disassembly driven motion but as explained in Fig. 6.4 a slightly modified version can explain assembly driven motion as well. A key feature of the model is the necessity for multiple binding sites. The binding sites are involved in the coupling but may at the same time effect microtubule growth. In Fig. 6.5, we argue that protofilaments may be forced to grow in an ordered manner. Brownian ratchet models, discussed in chapter 1 and 3, predict larger growth velocities under load for ordered growth than for random growth. It is therefore conceivable that proteins change the force-velocity relation.

Final considerations and new research directions

In vitro experiments

We would like to measure whether or not proteins that regulate microtubule dynamics have a serious effect on force generation and in particular if binding to specific sites changes the effect of force on microtubule dynamics as measured in chapters 3 and 4. Forces are very difficult to apply or measure in living cells and an *in vitro* experiment would be preferable. Experiments in this direction were performed on kinetochores purified from CHO cells [108]. Microtubule ends were observed to bind to the kinetochore and forces were applied with optical tweezers using beads connected to these microtubules. Pulling forces of more than 15 pN were applied without detachment of the microtubule from the kinetochore. The effect of the kinetochore attachment on dynamical parameters was, however, only measured at zero force. In our lab, we reconstituted budding yeast kinetochores on silica beads coated with centromeric DNA as described by Severin *et al.* [109]. These beads were observed to bind to the plus ends of GMPCPP-microtubule seeds, but prolonged attachment to growing or shrinking microtubules could not be observed [110]. During reconstitution not all kinetochore functionality was preserved. Therefore we switched to a more abstract model system consisting of silica beads coated with only motor proteins [111]. Beads coated with the motor protein kinesin were earlier reported to follow the tip of a disassembling microtubule plus end after a catastrophe [112], whereas normally kinesin walks to the plus end of a microtubule. This observation showed that the energy stored in the microtubule lattice after hydrolysis of GTP can be exploited to do work. Kinesin-coated beads were to our knowledge never reported to attach to growing plus ends. In the experiments that we report here we observed attachment of kinesin-coated bead to both assembling and disassembling microtubule tips. Furthermore we noticed an effect of attachment on microtubule dynamics.

Methods

Microtubule seeds were bound to the bottom of a flow cell as described in chapter 2. Silica beads (carboxyl terminated), with a diameter of 1.25 μm were coated non-specifically with streptavidin and were then incubated with a genetically modified *Drosophila* kinesin containing a biotinylated domain [113]. The flow cell was filled with a solution containing 14 to 20 μM tubulin, GTP, adenosine triphosphate (ATP), oxygen scavenging system (paragraph 2.4), 0.8 mM free biotin, 10 mg/ml BSA, 10 mM phosphocreatine, 80 $\mu\text{g/ml}$ phosphocreatine kinase and kinesin coated beads. Afterwards the cell was closed without decreasing its thickness. Biotin was added to block vacant streptavidin binding sites. The levels of ATP (0-1 mM) and GTP (0-1 mM) were varied to control the walking velocity of kinesin coated beads. Kinesin uses primarily hydrolysis of ATP for walking but GTP can be hydrolysed at a lower rate. Because hydrolysis lowers the ATP concentration, a phosphocreatine ATP-regenerating system was added to keep the ATP level constant. Taxol stabilised microtubules [8] were used at zero GTP concentration in a different assay

Chapter 6

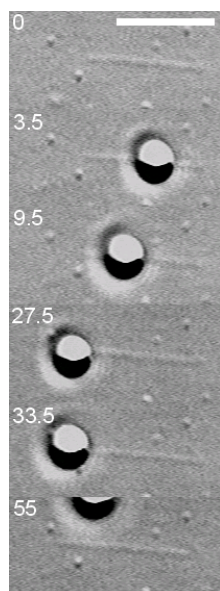


Figure 6.6 Snapshots of a kinesin-coated bead moving along a microtubule. The microtubule is nucleated by a seed at the right side and grows at $1.5 \mu\text{m}/\text{min}$. The bead is placed with optical tweezers on the microtubule ($t = 3.5 \text{ s}$) and moves initially at $16 \mu\text{m}/\text{min}$ towards the growing plus end. This motion slows down when the bead reaches the growing end ($t = 27.5 \text{ s}$). The bead loses its connection after 6 seconds ($t = 33.5 \text{ s}$) during which it moved at $0.9 \pm 0.7 \mu\text{m}/\text{min}$. The microtubule tip can be observed again after the bead diffused away ($t = 55 \text{ s}$). Scale bar equals $5 \mu\text{m}$.

as described earlier [114] in which stabilised microtubules are non-specifically bound over their full length to the surface. All samples were observed at $23 \text{ }^\circ\text{C}$.

Results

Microtubules were observed growing from the seeds at average velocities between $0.7 \mu\text{m}/\text{min}$ and $1.6 \mu\text{m}/\text{min}$ depending on the sample studied. Free-floating kinesin-coated beads were placed with optical tweezers on the microtubule near the seed region and after release were observed to walk at a GTP- and ATP-dependent velocity towards the plus end of microtubules (Fig. 6.6). Average bead velocities differed between $5.1 \mu\text{m}/\text{min}$ (0 mM ATP , 0.5 mM GTP) and $46.5 \mu\text{m}/\text{min}$ (1 mM ATP , 0 mM GTP). Most beads (184 out of 205 events) walked all the way to the microtubule end without releasing it with a typical run length exceeding $10 \mu\text{m}$. Beads that encountered a growing plus end did walk in most cases (79.2 %) off the microtubule within 0.5 seconds after reaching the end. The change between attachment and free Brownian motion of a bead could be observed on a time scale of 0.5 seconds. Some beads (17.4 %) did decrease their walk velocity abruptly

Final considerations and new research directions

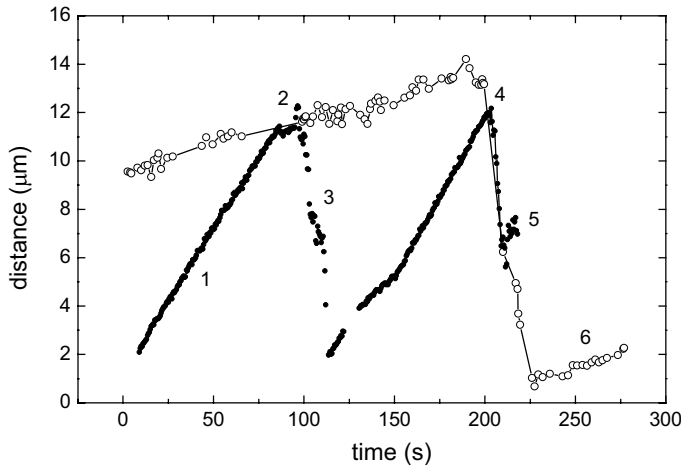


Figure 6.7 The measured distance for both the tip of a dynamic microtubule and a kinesin-coated bead relative to a fixed point on the microtubule seed are plotted as a function of time. Characteristic time points are indicated with numbers. The microtubule (open symbols) grows for 200 seconds and has a catastrophe (4) after which it again starts growing (6). The bead walks towards the plus end (1) and adjusts its speed to the speed of a growing microtubule after reaching the end (2). After connection is lost, the bead diffuses away (3) and is placed for a second time on the microtubule using optical tweezers and starts walking again. The bead encounters the shrinking microtubule when it has almost reached the microtubule end and is pulled along with the shrinking microtubule. Connection is lost at (5). The minus-end directed motion is not just diffusion, because it is clearly directed and faster than expected for diffusion.

upon reaching the microtubule end (Fig 6.6 and 6.7). This situation persisted for several seconds before the bead lost contact with the microtubule. Finally, in a few cases (3.5 %) a microtubule experienced a catastrophe apparently at the exact moment that the bead arrived at the end. Catastrophes were not seen when a bead lifted with the end of a growing microtubule, which was observed during a total time of 246.5 s for all experiments. In Fig. 6.8a we plotted the duration of individual attachment events versus the velocity at which the bead approached the end. The average duration (Fig. 6.8b) was longer at lower walk velocities. The ratio between bead velocity in the attached-state and microtubule growth velocity before bead arrival at the tip was on average 1.01 ± 0.08 (\pm standard error).

Beads interacted with shortening microtubules in two ways. Apart from the observed catastrophes (5 events) when a bead arrived at a growing microtubule end, it occurred (19 events) that an already disassembling microtubule overtook a walking bead. In both cases beads were observed to follow the end of disassembling microtubules for a few micrometers (8 out of 24 events in total) while others immediately detached. The total observation time of disassembly coupled bead motility was 19 seconds. The average bead

Chapter 6

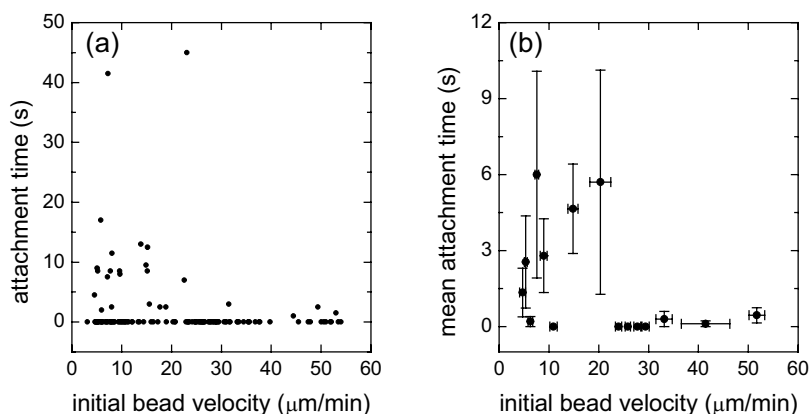


Figure 6.8 The measured attachment versus the velocity at which the bead walked towards the microtubule end. Individual events (a) are plotted with a zero attachment time if the bead directly lost contact upon arrival at the microtubule end. Ten events, successive in bead velocity, were averaged. The mean attachment time (b) (\pm standard error) is plotted versus the mean velocity of the binned data (\pm standard deviation).

velocity during this time was $36 \pm 0.5 \mu\text{m}/\text{min}$ with one extreme observation of $62 \mu\text{m}/\text{min}$ over 5.5 s. The average disassembly velocity of microtubule plus ends without connected beads was $17.5 \pm 0.4 \mu\text{m}/\text{min}$ in the samples studied.

Discussion

Our results show that kinesin-coated beads can adapt their speed to both growing and shortening microtubules. For growing microtubules no clear effect was seen of the bead on the assembly velocity. Although the number of observations is limited, the disassembly rate for a shortening microtubule seems to be accelerated by the attachment of the bead by a factor of two. A similar increase in disassembly rate was observed for kinesin-coated beads when catastrophes were induced by tubulin dilution [112]. A dilution buffer containing 40 mM KCl and 2 mM CaCl_2 was used in this study to weaken the association between kinesin and microtubules and increase the catastrophe rate [115]. Our results show that the effect on disassembly rate maintained at a larger kinesin affinity. There also seems to be an effect of the beads on the microtubule catastrophe rate. Five catastrophes were observed when a bead reached a growing microtubule end. The total observation time of interaction with a growing tip was 246.5 s. A catastrophe time of 49 ± 22 s (\pm standard error) can thus be calculated during tip attachment. The average catastrophe time in all samples for free microtubule growth without bead attachment was 486 ± 97 s. Catastrophes are thus induced by the kinesin-coated bead. It should be noted that catastrophes always occurred apparently at the exact moment that the bead reached the end. One can speculate that the microtubule is sometimes in a configuration that is prone

Final considerations and new research directions

to catastrophes and only needs a small extra kick. This configuration may correspond with an intermediate state between growth and shortening, which was proposed to explain microtubule severing experiments [116].

Motion of an object, like a bead, can thus be coupled to both assembling and disassembling microtubules. The mechanism must involve multiple motors, which is clear from the observed run lengths. Beads attached to single motors have run lengths of approximately $1\ \mu\text{m}$ [114]. One could argue that the observed effects might also occur when free kinesin, not linked to a bead, would have been added to dynamic microtubules. In fact, there are numerous free motors in our samples because we coat our beads with an excess of kinesin. The growth velocity and catastrophe time for non-attached microtubules are in these samples close to the values that were reported in chapters 3 and 4 for pure microtubules at similar tubulin concentrations but slightly different conditions. Free motors do thus not generate similar effects and multiple motors are necessary to affect catastrophe rate and disassembly velocity. We should note that the disassembly rate of shortening microtubules in these samples was $17.5 \pm 0.4\ \mu\text{m}/\text{min}$ whereas in motor free samples it was $28.9 \pm 0.3\ \mu\text{m}/\text{min}$ (chapter 3). Free motors possibly coat to some degree the microtubule wall and thereby slow down disassembly. We are not aware of reports on the motion of single motors near the ends of dynamic microtubules.

Coupling to an assembling microtubule is achieved somehow by an equilibrium between forward directed kinesin walking and the inherent affinity of kinesin to microtubules. Increasing the initial kinesin walk velocity, which causes beads to stick less long to microtubule ends (Fig. 6.7), shifts this equilibrium. It is not clear if kinesin motors do change their walk velocity after reaching the end of a microtubule in order to obtain a slower bead velocity. Alternatively, single kinesin molecules could detach at the end while others attach to the microtubule at the opposite site of the bead, which would cause the bead to rotate. We tried to observe this rotation by observing the walks of constructs of multiple beads that form during the coating procedure. A construct of two beads, with only one bead bound to the microtubule, was observed to stay at a fixed angle relative to the microtubule while walking along an already formed microtubule. Rotations with a short duration were observed but these were probably restricted to spots in the microtubule that contain lattice imperfections. It seems that during a normal walk a constant number of kinesin molecules form a train and all walk at the same rate without losing attachment. Until now we did not observe enough events of constructs that stayed sufficiently long at the end of a microtubule to make a statement about rotations at the end.

We did not apply forces to the beads other than the very small viscous drag that a bead experiences when moving. We could use the optical tweezers to exert forces tangent to the microtubule in two possible directions. Forces exerted on tubulin dimers via the bead might lead to different assembly behaviour. Forces should be tuned to relevant values because large forces would, depending on the direction, pull the bead off the microtubule or stall the bead, while the microtubule continues growth. The time a bead spends attached

Chapter 6

to the tip is limited to a few seconds. This short duration will be a complicating factor when applying forces. Other motors with other walk velocities and affinities might be useful to extend the duration of tip attachment. Preferentially one should study motors that are known to localise to the kinetochore. Salt concentration can be changed to tune the affinity of motor proteins [117]. Alternatively, we might perform an experiment as described in the previous paragraph but now with a barrier coated with motor proteins. In this configuration the end-on contact between an object and a growing microtubule is made explicitly, which may better represent the situation of a kinetochore bound microtubule whose tip impinges on the chromosomes while motor proteins take care of binding or growth modulation.

Results obtained so far show that multiple cooperating motor proteins are able to couple motion of an object to both assembling and disassembling microtubules under similar conditions. Together with the localisation of motor proteins on microtubule end binding complexes like kinetochores, this and other *in vitro* work [52,112] suggests a role for motors as couplers *in vivo*. At the same time we observed that cooperating motors can change both the catastrophe rate and disassembly rate of microtubules. Future work should be directed to elicit the contributions of both motors and intrinsic microtubule properties to force generation and regulation of dynamic instability.

6.3 On the mechanism of dynamic instability

Many researches have pursued the elucidation of the mechanism that causes an elongating microtubule to switch to rapid shortening. Linked to these catastrophes are rescues, i.e. the opposite process. In the past many ingenious experiments were performed to extract information about the process. However, there still does not exist a satisfying description that is able to describe all observations made. Knowing the details about processes that occur at the tip of a microtubule would allow us to speculate on the strategies that the cell uses to regulate dynamic instability. Proteins like Op18, XMAP215, EB1 all effect certain aspects of the growth process but the pathway used remains unclear. They might change hydrolysis rate, stop growth by blocking terminating tubulin proteins or recognise a sheet like structure at the end of growing microtubules to localise themselves to the tips of growing microtubules. Our work on force generating microtubules can be added to the list of observations that needs to be dealt with in coming to a good description of dynamic instability. Here we would like to summarise current ideas on the mechanism of dynamic instability, report a few ‘freak’ events that occurred during our experiments and speculate on their consequences.

Assembly process may not be perfectly first order

Microtubule growth is usually described using an on- and off-rate for GTP-tubulin like in Eq. 1.3. During growth, switches in growth velocity and even pauses occur of a duration

Final considerations and new research directions

that can not be explained by stochastic fluctuations during a simple assembly process [71,72]. This proves that other secondary processes effect microtubule assembly. Likely candidates are the hydrolysis of terminal GTP-subunits and structural effects caused by for example sheets. An incoming GTP-tubulin protein that wants to assemble is likely to have a different affinity for a lattice spot containing GDP-tubulin or GTP-tubulin [9,58]. Proteins that attach to one of the two protofilaments that form the edge of a sheet can not make lateral connections at one side and elongation might therefore be slower. The affinities for all these different conformations are not known and therefore one can only speculate on the on- and off-rates for these different types of attachments. Different affinities would not only change elongation, but the catastrophe mechanism as well. To assess the effect of hydrolysis it would be interesting to study possible velocity fluctuations and pauses during the growth of GMPCPP-microtubules, in which hydrolysis occurs slowly and very infrequently at terminal subunits.

If assembly is influenced by hydrolysis or other effects the concept of a critical concentration becomes ill-defined. Maybe this is the reason why a wide range of critical concentrations was reported in previous studies [9]. Also the relation between catastrophe time and growth velocity differs between different reports [11,19,55]. Experiments on catastrophes can best be compared by growth velocity instead of tubulin concentration to avoid misinterpretations caused by errors in estimating the exact tubulin concentration. In earlier experiments that are not included in this thesis, we used tubulin that we purified from pig-brain. The catastrophe rate was lower at a certain growth velocity compared to experiments at the same buffer conditions but with tubulin obtained from Cytoskeleton, Inc. (chapter 4). These kinds of differences should be taken seriously when describing dynamic instability. If the average elongation rate depends not only on tubulin concentration but also on the rate of GTP hydrolysis, different rates of GTP hydrolysis can cause different apparent critical concentrations and different velocity-catastrophe relations. The rate of GTP hydrolysis can differ between different tubulin iso-types [8] or may be influenced by the levels of GTP, GDP or phosphate in the sample [118-120]. In general, protein affinities may be changed by the exact salt concentration. Comparing quantitative result between different studies should be done with care.

Sheets at the ends of growing microtubules

The existence of sheets is under debate because their size makes them in general inappropriate for observations with the light microscope [16,59]. Special preparation methods were developed for sheet analysis with the electron microscope [16]. It has been shown clearly that the appearance of sheets can be regulated by the microtubule growth conditions [16,59] and therefore it is unlikely that they are only caused by the sample preparation method. When performing our experiments under the DIC microscope we occasionally observed curved structures at the ends of growing microtubules, with a length of the order of a micron, reminiscent of sheets (Fig. 6.9). Similar observations were

Chapter 6

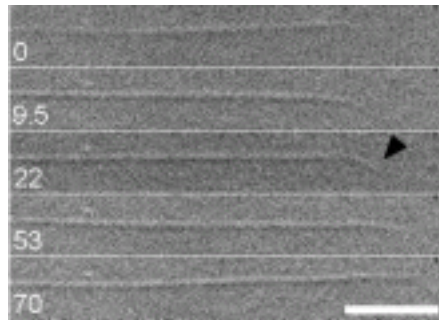


Figure 6.9 The appearance of a curved extension (indicated with an arrow) on a plus end of an elongating microtubule, which may be an unfolded sheet of protofilaments. The growth velocity of the sheet extension was close to the long term average speed of the microtubule, $2.9 \mu\text{m}/\text{min}$, but quantitative comparison is hard because the visibility of the sheet was poor. Time, relative to the first frame, is indicated in seconds and the scale bar is $5 \mu\text{m}$. After 9.5 s , a sheet forms, which first extends and later slowly disappears again around $t = 53 \text{ s}$. After $t = 70 \text{ s}$ no curving is observed and the microtubule grows as usual.

reported by Chrétien *et al.* [16]. These may be freak events or the extremes of a wide distribution of sheet sizes. Furthermore, we noted that beads coated with kinesin (section 6.2) occasionally stopped moving when they reached the end of an elongating microtubule. After some time the bead then suddenly resumed motion at a rapid speed. A possible interpretation is that the motors are halted by an open sheet, which needs to be folded into a tube before motion can be resumed.

Coupled hydrolysis

The main question still is: ‘What triggers a catastrophe?’. GTP hydrolysis is necessary, but it is not clear whether all 13 protofilaments should be hydrolysed including their terminal subunit in order for a catastrophe to occur. It is clear that approximately one ring of GMPCPP subunits is enough to prevent a catastrophe [121,122]. These kind of observations led to a coupled hydrolysis model in which it is assumed that an incoming GTP-subunit hydrolyses its predecessor that is now not longer the terminal subunit. The molecular structure of the tubulin protein suggests such a coupled hydrolysis mechanism [7]. The consequence of this mechanism would be a single ring of GTP-tubulin at the end of elongating microtubules. Using biochemical assays extended caps of GTP were indeed never observed [120,123]. Models made on the basis of coupled hydrolysis were however not able to describe the full range of observations listed or contained many unknown parameters [58,124].

At the onset of disassembly, the protofilaments lose their lateral contacts and peel outwards. This event may be regulated by the spontaneous hydrolysis or disassembly of terminal GTP-subunits. But how many terminal subunits should be transformed to GDP

Final considerations and new research directions

before a tube like structure is not stable anymore? A sheet at the end of a microtubule relaxes the outward curvature of protofilaments [16,73] and terminal GDP subunits may be allowed without an immediate catastrophe. The number of GDP subunits needed for a catastrophe may be dependent on the sheet length. The sheet length itself is dependent on tubulin concentration [16] and therefore, this mechanism could effect the catastrophe-growth velocity relation. It was suggested that catastrophes can occur only at microtubules that are completely closed into a cylinder [16] and we can also imagine that the appearance of a single terminal GDP subunit triggers sheet formation. The complexity of the system is the cause of our lack of understanding and a full description may not be a simple one but should describe many processes at the same time.

Information from stalled microtubules

The observed distribution of catastrophe times for stalled microtubules (Fig. 4.3) is surprising because it is different from the near exponential distribution for free microtubules (Fig. 4.5). Apparently there is a process with a well-determined timescale that needs to proceed before a catastrophe can occur. Could this be the hydrolysis of the terminal subunits of protofilaments? Imagine a microtubule with a complete crown of GTP-tubulin at its tip being halted suddenly by a barrier. We may argue that N out of 13 protofilaments should become hydrolysed before the occurrence of a catastrophe, with each hydrolysis step being a Poisson process with a certain rate. The probability distribution of the time needed for hydrolysis is plotted in Fig. 6.10 together with the data. The model fits the data well for $N > 7$, which, if the description is valid, indicates that the (non-coupled) hydrolysis rate is around 0.1 s^{-1} . Until now we were not successful in converting this knowledge into a model that describes our data on free catastrophes satisfactory [125]. After a single hydrolysis event on a terminating tubulin dimer, a GDP-dimer is exposed. For free microtubules, this GDP-dimer is recapped quickly by an incoming GTP-dimer before neighbouring protofilaments can hydrolyse their terminal dimer as well. The chance on the occurrence of multiple terminal GDP-dimers is very low. The calculated catastrophe time vs. growth-velocity relation is exponential in the growth velocity and not linear as was observed (chapter 4). Possible our approach is invalid or we need to assume some form of communication between protofilaments [124].

Minus ends

Most reported observations are made on the plus ends of growing microtubules whereas the minus end shows dynamic instability as well but at different rates [19]. We as well focused on the plus end but occasionally observed buckling and force generation of minus ends. Short microtubules ($\approx 5 \mu\text{m}$ long) with their minus end pushing were seen to stall for many minutes, which suggests that the catastrophe rate is less rigidly linked to elongation as it is at the plus end. We however did not characterise the free growth behaviour of minus ends so quantitative conclusions can not be drawn.

Chapter 6

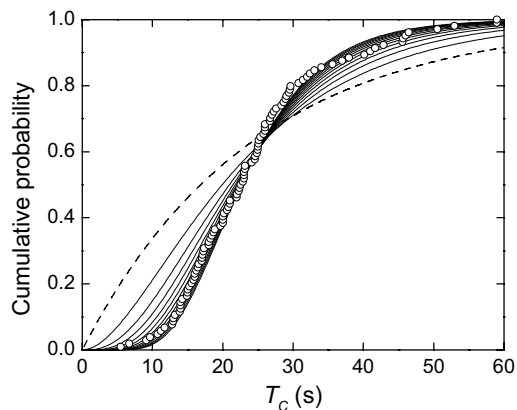


Figure 6.10 Cumulative distribution of catastrophe times measured on stalled microtubules (see Fig. 4.3). Plotted is the probability that at a given time N out of 13 parallel processes proceeded while $13 - N$ did not. Each individual process is modelled as a Poisson process with probability of occurrence equal to $(1 - \exp(-kt))$, where k is a rate and t is time. The resulting distribution is plotted for $N = 1$ (dashed) until $N = 13$. The experimentally observed ‘S-curve’ becomes more explicit at high N . The rate k is chosen to yield a mean catastrophe time equal to the experimentally observed time: $k = 0.134 \text{ s}^{-1}$ for $N = 13$.

Future experiments

Dynamic instability remains puzzling and progress will probably be made by studying mutated tubulin proteins [126] or tubulin iso-types that have different hydrolysis rates. The development of techniques that allow the distinction between GTP and GDP form of tubulin under the electron microscope would provide a wealth of information. As mentioned, detailed comparison between microtubule growth in the presence of GTP or GMPCPP should give more information on the role of hydrolysis than obtained until now. Furthermore, important information should become available from work on regulatory proteins. The application of force on a growing microtubule using optical tweezers as described in section 6.1 will allow for a new kind of control over rate constants, which hopefully will lead to new insights into microtubule dynamics.

6.4 Acknowledgements

The work on force generation measurements with optical tweezers has been performed together with Jacob Kerssemakers and the work on kinesin-coated beads with Eva Riemsdag. We would like to thank Astrid van de Horst and Cendrine Faivre-Moskalenko for setting up the tweezers, Gerbrand Koster and Martijn van Duijn for the preparation of biotinylated kinesin and Dirk Vossen for providing silica beads. Sander van Doorn did the work on the reconstitution of kinetochores in combination with dynamic microtubules.

Bibliography

- [1] B. Alberts, A. Johnson, J. Lewis, M. Raff, K. Roberts, and P. Walter, *Molecular biology of the cell*, 4th ed, Garland Science, New York (2002).
- [2] J. Howard, *Mechanics of motor proteins and the cytoskeleton*, Sinauer Associates, Sunderland (2001).
- [3] K. Svoboda, C. F. Schmidt, B. J. Schnapp, and S. M. Block, Direct observation of kinesin stepping by optical trapping interferometry, *nature* **365**, 721-727 (1993).
- [4] K. Visscher, M. J. Schnitzer, and S. M. Block, Single kinesin molecules studied with a molecular force clamp, *nature* **400**, 184-189 (1999).
- [5] C. M. Waterman-Storer, J. Gregory, S. F. Parsons, and E. D. Salmon, Membrane/microtubule tip attachment complexes (tacs) allow the assembly dynamics of plus ends to push and pull membranes into tubulovesicular networks in interphase xenopus egg extracts, *Journal of Cell Biology* **130**, 1161-1169 (1995).
- [6] C. Waterman-Storer and E. Salmon, Endoplasmic reticulum membrane tubules are distributed by microtubules in living cells using three distinct mechanisms, *Current Biology* **8**, 798-806 (1998).
- [7] E. Nogales, Structural insights into microtubule function, *Annual Review of Biophysics and Biomolecular Structure* **30**, 397-420 (2001).
- [8] J. S. Hyams and C. W. Lloyd, *Microtubules*, Wiley-Liss, New York (1994).
- [9] A. Desai and T. J. Mitchison, Microtubule polymerization dynamics, *Annual Review of Cell and Developmental Biology* **13**, 83-117 (1997).
- [10] F. Gittes, B. Mickey, J. Nettleton, and J. Howard, Flexural rigidity of microtubules and actin filaments measured from thermal fluctuations in shape, *Journal of Cell Biology* **120**, 923-934 (1993).
- [11] D. K. Fygenson, E. Braun, and A. Libchaber, Phase diagram of microtubules, *Physical Review E* **50**, 1579-1588 (1994).
- [12] S. Doxsey, Re-evaluating centrosome function, *Nature Reviews Molecular Cell Biology* **2**, 688-698 (2001).
- [13] T. J. Mitchison and M. W. Kirschner, Dynamic instability of microtubule growth, *nature* **312**, 237-242 (1984).
- [14] A. A. Hyman, S. Salser, D. N. Drechsel, N. Unwin, and T. J. Mitchison, Role of gtp hydrolysis in microtubule dynamics - information from a slowly hydrolyzable analog, gmpcpp, *Molecular Biology of the Cell* **3**, 1155-1167 (1992).
- [15] W. V. Nicholson, M. Lee, K. H. Downing, and E. Nogales, Cryo-electron microscopy of gdp-tubulin rings, *Cell Biochemistry and Biophysics* **31**, 175-183 (1999).
- [16] D. Chretien, S. D. Fuller, and E. Karsenti, Structure of growing microtubule ends - 2-dimensional sheets close into tubes at variable rates, *Journal of Cell Biology* **129**, 1311-1328 (1995).
- [17] T. Muller-Reichert, D. Chretien, F. Severin, and A. A. Hyman, Structural changes at microtubule ends accompanying gtp hydrolysis: Information from a slowly hydrolyzable analogue of gtp, guanylyl (alpha,beta)methylenediphosphonate, *Proceedings of the National Academy of Sciences of the United States of America* **95**, 3661-3666 (1998).
- [18] H. Flyvbjerg, D. Chretien, and I. M. Janski, Structural microtubule cap: Stability, catastrophe, rescue, and third state, *Biophysical Journal* **82**, 2023 (2002).

Bibliography

- [19] R. A. Walker, E. T. O'Brien, N. K. Pryer, M. F. Soboeiro, W. A. Voter, H. P. Erickson, and E. D. Salmon, Dynamic instability of individual microtubules analyzed by video light-microscopy - rate constants and transition frequencies, *Journal of Cell Biology* **107**, 1437-1448 (1988).
- [20] F. Verde, M. Dogterom, E. Stelzer, E. Karsenti, and S. Leibler, Control of microtubule dynamics and length by cyclin a- and cyclin b-dependent kinases in xenopus egg extracts, *Journal of Cell Biology* **118**, 1097-1108 (1992).
- [21] T. Wittmann, A. Hyman, and A. Desai, The spindle: A dynamic assembly of microtubules and motors, *Nature Cell Biology* **3**, E28-E34 (2001).
- [22] C. L. Rieder and E. D. Salmon, Motile kinetochores and polar ejection forces dictate chromosome position on the vertebrate mitotic spindle, *Journal of Cell Biology* **124**, 223-233 (1994).
- [23] R. Heald and C. E. Walczak, Microtubule-based motor function in mitosis, *Current Opinion in Structural Biology* **9**, 268-274 (1999).
- [24] C. L. Rieder and E. D. Salmon, The vertebrate cell kinetochore and its roles during mitosis, *Trends in Cell Biology* **8**, 310-318 (1998).
- [25] A. P. Joglekar and A. J. Hunt, A simple, mechanistic model for directional instability during mitotic chromosome movements, *Biophys Journal* **83**, 42-58 (2002).
- [26] A. Khodjakov, I. S. Gabashvili, and C. L. Rieder, "dumb" versus "smart" kinetochore models for chromosome congression during mitosis in vertebrate somatic cells, *Cell Motility and the Cytoskeleton* **43**, 179-185 (1999).
- [27] L. Mahadevan and P. Matsudaira, Motility powered by supramolecular springs and ratchets, *Science* **288**, 95-99 (2000).
- [28] J. A. Theriot, The polymerization motor, *Traffic* **1**, 19-28 (2000).
- [29] S. Inoue and E. D. Salmon, Force generation by microtubule assembly/disassembly in mitosis and related movements, *Molecular Biology of the Cell* **6**, 1619-1640 (1995).
- [30] N. Watanabe and T. J. Mitchison, Single-molecule speckle analysis of actin filament turnover in lamellipodia, *Science* **295**, 1083-1086 (2002).
- [31] A. Mogilner and G. Oster, Cell motility driven by actin polymerization, *Biophysical Journal* **71**, 3030-3045 (1996).
- [32] C. S. Peskin, G. M. Odell, and G. F. Oster, Cellular motions and thermal fluctuations - the brownian ratchet, *Biophysical Journal* **65**, 316-324 (1993).
- [33] T. L. Hill, *Linear aggregation theory in cell biology*, Springer-Verlag, New York (1987).
- [34] V. C. Abraham, V. Krishnamurthi, D. L. Taylor, and F. Lanni, The actin-based nanomachine at the leading edge of migrating cells, *Biophysical Journal* **77**, 1721-1732 (1999).
- [35] L. Tilney and S. Inoue, Acrosomal reaction of thymosin sperm. II. The kinetics and possible mechanism of acrosomal process elongation, *Journal of Cell Biology* **93**, 820-827 (1982).
- [36] J. A. Theriot, Worm sperm and advances in cell locomotion, *Cell* **84**, 1-4 (1996).
- [37] J. E. Italiano, T. M. Roberts, M. Stewart, and C. A. Fontana, Reconstitution in vitro of the motile apparatus from the amoeboid sperm of ascaris shows that filament assembly and bundling move membranes, *Cell* **84**, 105-114 (1996).
- [38] D. Pantaloni, C. L. Clainche, and M.-F. Carlier, Mechanism of actin-based motility, *Science* **292**, 1502-1506 (2001).
- [39] A. Bernheim-Groswasser, S. Wiesner, R. M. Golsteyn, M. F. Carlier, and C. Sykes, The dynamics of actin-based motility depend on surface parameters, *nature* **417**, 308-311 (2002).
- [40] D. J. Sharp, G. C. Rogers, and J. M. Scholey, Microtubule motors in mitosis, *nature* **407**, 41-47 (2000).

Bibliography

- [41] D. L. Dujardin and R. B. Vallee, Dynein at the cortex, *Current Opinion in Cell Biology* **14**, 44-49 (2002).
- [42] P. T. Tran, L. Marsh, V. Doye, S. Inoue, and F. Chang, A mechanism for nuclear positioning in fission yeast based on microtubule pushing, *Journal of Cell Biology* **153**, 397-411 (2001).
- [43] J. G. Ault, A. J. Demarco, E. D. Salmon, and C. L. Rieder, Studies on the ejection properties of asters - astral microtubule turnover influences the oscillatory behavior and positioning of mono-oriented chromosomes, *Journal of Cell Science* **99**, 701-710 (1991).
- [44] A. A. Hyman and T. J. Mitchison, 2 different microtubule-based motor activities with opposite polarities in kinetochores, *nature* **351**, 206-211 (1991).
- [45] H. Miyata, S. Nishiyama, K. Akashi, and K. Kinoshita, Protrusive growth from giant liposomes driven by actin polymerization, *Proceedings of the National Academy of Sciences of the United States of America* **96**, 2048-2053 (1999).
- [46] D. K. Fygenson, J. F. Marko, and A. Libchaber, Mechanics of microtubule-based membrane extension, *Physical Review Letters* **79**, 4497-4500 (1997).
- [47] M. Dogterom and B. Yurke, Measurement of the force-velocity relation for growing microtubules, *Science* **278**, 856-860 (1997).
- [48] A. Mogilner and G. Oster, The polymerization ratchet model explains the force-velocity relation for growing microtubules, *European Biophysics Journal with Biophysics Letters* **28**, 235-242 (1999).
- [49] T. E. Holy, M. Dogterom, B. Yurke, and S. Leibler, Assembly and positioning of microtubule asters in microfabricated chambers, *Proceedings of the National Academy of Sciences of the United States of America* **94**, 6228-6231 (1997).
- [50] C. Faivre-Moskalenko and M. Dogterom, Dynamics of microtubule organizing centers in micro-fabricated chambers: The role of catastrophes, submitted to *Proceedings of the National Academy of Sciences of the United States of America*.
- [51] M. Dogterom and B. Yurke, Microtubule dynamics and the positioning of microtubule organizing centers, *Physical Review Letters* **81**, 485-488 (1998).
- [52] V. A. Lombillo, C. Nislow, T. J. Yen, V. I. Gelfand, and J. R. McIntosh, Antibodies to the kinesin motor domain and cenp-e inhibit microtubule depolymerization-dependent motion of chromosomes in-vitro, *Journal of Cell Biology* **128**, 107-115 (1995).
- [53] G. S. v. Doorn, C. Tanase, B. M. Mulder, and M. Dogterom, On the stall force for growing microtubules, *European Biophysics Journal with Biophysics Letters* **29**, 2-6 (2000).
- [54] M. Dogterom, M. E. Janson, C. Faivre-Moskalenko, A. Van der Horst, J. W. J. Kerssemakers, C. Tanase, and B. M. Mulder, Force generation by polymerizing microtubules, *Applied Physics a-Materials Science & Processing* **75**, 331-336 (2002).
- [55] D. N. Drechsel, A. A. Hyman, M. H. Cobb, and M. W. Kirschner, Modulation of the dynamic instability of tubulin assembly by the microtubule-associated protein tau, *Molecular Biology of the Cell* **3**, 1141-1154 (1992).
- [56] F. Reif, *Statistical physics*, McGraw-Hill, New York (1965).
- [57] C. Tanase, B. M. Mulder, and M. Dogterom, The multifilament brownian ratchet model for growing microtubules, in preparation.
- [58] S. R. Martin, M. J. Schilstra, and P. M. Bayley, Dynamic instability of microtubules - monte-carlo simulation and application to different types of microtubule lattice, *Biophysical Journal* **65**, 578-596 (1993).
- [59] I. Arnal, E. Karsenti, and A. A. Hyman, Structural transitions at microtubule ends correlate with their dynamic properties in xenopus egg extracts, *Journal of Cell Biology* **149**, 767-774 (2000).

Bibliography

- [60] P. T. Tran, P. Joshi, and E. D. Salmon, How tubulin subunits are lost from the shortening ends of microtubules, *Journal of Structural Biology* **118**, 107-118 (1997).
- [61] M. Pluta, *Advanced light microscopy, vol. 2 specialized methods*, Elsevier (1989).
- [62] C. Wiese and Y. X. Zheng, Gamma-tubulin complexes and their interaction with microtubule-organizing centers, *Current Opinion in Structural Biology* **9**, 250-259 (1999).
- [63] M. Caplow, R. L. Ruhlen, and J. Shanks, The free-energy for hydrolysis of a microtubule-bound nucleotide triphosphate is near zero - all of the free-energy for hydrolysis is stored in the microtubule lattice, *Journal of Cell Biology* **127**, 779-788 (1994).
- [64] F. Gittes, E. Meyhofer, S. Baek, and J. Howard, Directional loading of the kinesin motor molecule as it buckles a microtubule, *Biophysical Journal* **70**, 418-429 (1996).
- [65] L. D. Landau and E. M. Lifshitz, *Theory of elasticity*, Pergamon, New York (1986).
- [66] R. P. Feynman, *The feynman lectures on physics, vol 2*, Addison-Wesley, Reading, MA (1964).
- [67] M. Abramowitz and I. A. Stegun, *Handbook of mathematical functions*, Dover Publications, New York (1965).
- [68] W. H. Press, S. A. Teukolsky, W. T. Vetterling, and B. P. Flannery, *Numerical recipes in c*, 2nd ed, Cambridge University Press, Cambridge (1992).
- [69] A. B. Kolomeisky and M. E. Fisher, Force-velocity relation for growing microtubules, *Biophysical Journal* **80**, 149-154 (2001).
- [70] C. S. Peskin and G. F. Oster, Force production by depolymerizing microtubules : Load-velocity curves and run-pause statistics, *Biophysical Journal* **69**, 2268-2276 (1995).
- [71] R. F. Gildersleeve, A. R. Cross, K. E. Cullen, A. P. Fagen, and R. C. Williams, Microtubules grow and shorten at intrinsically variable rates, *Journal of Biological Chemistry* **267**, 7995-8006 (1992).
- [72] D. Chretien and S. D. Fuller, Microtubules switch occasionally into unfavorable configurations during elongation, *Journal of Molecular Biology* **298**, 663-676 (2000).
- [73] D. Chretien, I. Janosi, J. C. Taveau, and H. Flyvbjerg, Microtubule's conformational cap, *Cell Structure and Function* **24**, 299-303 (1999).
- [74] Y. A. Komarova, I. A. Vorobjev, and G. G. Borisy, Life cycle of mts: Persistent growth in the cell interior, asymmetric transition frequencies and effects of the cell boundary, *Journal of Cell Science* **115**, 3527-3539 (2002).
- [75] K. Kinoshita, I. Arnal, A. Desai, D. N. Drechsel, and A. A. Hyman, Reconstitution of physiological microtubule dynamics using purified components, *Science* **294**, 1340-1343 (2001).
- [76] L. Cassimeris, D. Gard, P. T. Tran, and H. P. Erickson, Xmap215 is a long thin molecule that does not increase microtubule stiffness, *Journal of Cell Science* **114**, 3025-3033 (2001).
- [77] D. Brunner and P. Nurse, Clip170-like tip1p spatially organizes microtubular dynamics in fission yeast, *Cell* **102**, 695-704 (2000).
- [78] D. R. Drummond and R. A. Cross, Dynamics of interphase microtubules in *schizosaccharomyces pombe*, *Current Biology* **10**, 766-775 (2000).
- [79] R. A. Walker, N. K. Pryer, and E. D. Salmon, Dilution of individual microtubules observed in real-time invitro - evidence that cap size is small and independent of elongation rate, *Journal of Cell Biology* **114**, 73-81 (1991).
- [80] M. E. Janson, J. W. J. Kerssemakers, M. E. de Dood, and M. Dogterom, Microtubule dynamic instability under load, *Biophysical Journal* **82**, 2489 (2002).
- [81] H. M. Wadsworth, *Handbook of statistical methods for engineers and scientists*, McGraw-Hill, New York (1990).
- [82] D. J. Odde, Kinetics of microtubule catastrophe assessed by probabilistic analysis, *Biophysical Journal* **69**, 796-802 (1995).

Bibliography

- [83] T. E. Holy and S. Leibler, Dynamic instability of microtubules as an efficient way to search in-space, *Proceedings of the National Academy of Sciences of the United States of America* **91**, 5682-5685 (1994).
- [84] B. Mickey and J. Howard, Rigidity of microtubules is increased by stabilizing agents, *Journal of Cell Biology* **130**, 909-917 (1995).
- [85] J. C. Kurz and R. C. Williams, Microtubule-associated proteins and the flexibility of microtubules, *Biochemistry* **34**, 13374-13380 (1995).
- [86] P. Venier, A. C. Maggs, M.-F. Carlier, and D. Pantaloni, Analysis of microtubule rigidity using hydrodynamic flow and thermal fluctuations, *Journal of Biological Chemistry* **269**, 13353-13360 (1994).
- [87] H. Felgner, R. Frank, and M. Schliwa, Flexural rigidity of microtubules measured with the use of optical tweezers, *Journal of Cell Science* **109**, 509-516 (1996).
- [88] H. Felgner, R. Frank, J. Biernat, E. M. Mandelkow, E. Mandelkow, B. Ludin, A. Matus, et al., Domains of neuronal microtubule-associated proteins and flexural rigidity of microtubules, *Journal of Cell Biology* **138**, 1067-1075 (1997).
- [89] A. J. Hunt, F. Gittes, and J. Howard, The force exerted by a single kinesin molecule against a viscous load, *Biophysical Journal* **67**, 766-781 (1994).
- [90] A. Ashkin, Optical trapping and manipulation of neutral particles using lasers, *Proceedings of the National Academy of Sciences of the United States of America* **94**, 4853-4860 (1997).
- [91] M. Kurachi, M. Hoshi, and H. Tashiro, Buckling of a single microtubule by optical trapping forces - direct measurement of microtubule rigidity, *Cell Motility and the Cytoskeleton* **30**, 221-228 (1995).
- [92] D. K. Fygenson, M. Elbaum, B. Shraiman, and A. Libchaber, Microtubules and vesicles under controlled tension, *Physical Review E* **55**, 850-859 (1997).
- [93] C. H. Wiggins, D. Riveline, A. Ott, and R. E. Goldstein, Trapping and wiggling: Elastohydrodynamics of driven microfilaments, *Biophysical Journal* **74**, 1043-1060 (1998).
- [94] M. G. Poirier and J. F. Marko, Effect of internal friction on biofilament dynamics, *Physical Review Letters* **88**, art. no.-228103 (2002).
- [95] D. Chretien, F. Metoz, F. Verde, E. Karsenti, and R. H. Wade, Lattice-defects in microtubules - protofilament numbers vary within individual microtubules, *Journal of Cell Biology* **117**, 1031-1040 (1992).
- [96] K. Svoboda and S. M. Block, Biological applications of optical forces, *Annual Review of Biophysics and Biomolecular Structures* **23**, 247-285 (1994).
- [97] K. Visscher and S. M. Block, in *Methods in enzymology*, edited by R. B. Vallee, Academic Press, San Diego, Vol. 298, p. 460-489 (1997).
- [98] H. Flyvbjerg, T. E. Holy, and S. Leibler, Microtubule dynamics: Caps, catastrophes, and coupled hydrolysis, *Physical Review E* **54**, 5538-5560 (1996).
- [99] W. A. Voter, E. T. O'Brien, and H. P. Erickson, Dilution-induced disassembly of microtubules - relation to dynamic instability and the gtp cap, *Cell Motility and the Cytoskeleton* **18**, 55-62 (1991).
- [100] J. Gelles, B. J. Schnapp, and M. P. Sheetz, Tracking kinesin-driven movements with nanometre-scale precision, *nature* **331**, 450-453 (1988).
- [101] K. Svoboda and S. M. Block, Force and velocity measured for single kinesin molecules, *Cell* **77**, 773-784 (1994).
- [102] J. S. Tirnauer and B. E. Bierer, Eb1 proteins regulate microtubule dynamics, cell polarity, and chromosome stability, *Journal of Cell Biology* **149**, 761-766 (2000).
- [103] F. Perez, G. S. Diamantopoulos, R. Stalder, and T. E. Kreis, Clip-170 highlights growing microtubule ends in vivo, *Cell* **96**, 517-527 (1999).

Bibliography

- [104] R. P. Budde, A. Kumagai, W. G. Dunphy, and R. Heald, Regulation of op18 during spindle assembly in xenopus egg extracts, *Journal of Cell Biology* **153**, 149-157 (2001).
- [105] A. W. Hunter and L. Wordeman, How motor proteins influence microtubule polymerization dynamics, *Journal of Cell Science* **113**, 4379-4389 (2000).
- [106] A. Blocker, G. Griffiths, J. C. Olivo, A. A. Hyman, and F. F. Severin, A role for microtubule dynamics in phagosome movement, *Journal of Cell Science* **111**, 303-312 (1998).
- [107] S. Endow, *Dynamics of cell division*, Oxford University Press, New York (1999).
- [108] A. J. Hunt and J. R. McIntosh, The dynamic behavior of individual microtubules associated with chromosomes in-vitro, *Molecular Biology of the Cell* **9**, 2857-2871 (1998).
- [109] F. Severin, K. Kaplan, P. Sorger, and T. Hyman, In vitro assays for studying saccharomyces cerevisiae kinetochore activity, *Methods in Cell Biology* **61**, 145-153 (1999).
- [110] G. S. v. Doorn, *The interaction between kinetochores and dynamic microtubules*, undergraduate thesis, FOM institute AMOLF, Amsterdam (1999).
- [111] E. E. F. Riemsdag, *Motor proteins as couplers to dynamic microtubules*, undergraduate thesis, FOM institute AMOLF, Amsterdam (2002).
- [112] V. A. Lombillo, R. J. Stewart, and J. R. McIntosh, Minus-end-directed motion of kinesin-coated microspheres driven by microtubule depolymerization, *nature* **373**, 161-164 (1995).
- [113] E. Young, E. Berliner, H. Mahtani, B. Perez-Ramirez, and J. Gelles, Subunit interactions in dimeric kinesin heavy chain derivatives that lack the kinesin rod, *Journal of Biological Chemistry* **270**, 3926-3931 (1995).
- [114] S. M. Block, L. S. B. Goldstein, and B. J. Schnapp, Bead movement by single kinesin molecules studied with optical tweezers, *nature* **348**, 348-352 (1990).
- [115] E. T. O'Brien, E. D. Salmon, and H. P. Erickson, How calcium causes microtubule depolymerization, *Cell Motility and the Cytoskeleton* **36**, 125-135 (1997).
- [116] P. T. Tran, R. A. Walker, and E. D. Salmon, A metastable intermediate state of microtubule dynamic instability that differs significantly between plus and minus ends, *Journal of Cell Biology* **138**, 105-117 (1997).
- [117] R. D. Vale, D. R. Soll, and I. R. Gibbons, One-dimensional diffusion of microtubules bound to flagellar dynein, *Cell* **59**, 915-925 (1989).
- [118] M. Caplow and J. Shanks, Induction of microtubule catastrophe by formation of tubulin - gdp and apotubulin subunits at microtubule ends, *Biochemistry* **34**, 15732-15741 (1995).
- [119] Y. Tanaka-Takiguchi, T. J. Itoh, and H. Hotani, Visualization of the gdp-dependent switching in the growth polarity of microtubules, *Journal of Molecular Biology* **280**, 365-373 (1998).
- [120] D. Panda, H. P. Miller, and L. Wilson, Determination of the size and chemical nature of the stabilizing "cap" at microtubule ends using modulators of polymerization dynamics, *Biochemistry* **41**, 1609-1617 (2002).
- [121] D. N. Drechsel and M. W. Kirschner, The minimum gtp cap required to stabilize microtubules, *Current Biology* **4**, 1053-1061 (1994).
- [122] M. Caplow and J. Shanks, Evidence that a single monolayer tubulin-gtp cap is both necessary and sufficient to stabilize microtubules, *Molecular Biology of the Cell* **7**, 663-675 (1996).
- [123] A. Vandecandelaere, M. Brune, M. R. Webb, S. R. Martin, and P. M. Bayley, Phosphate release during microtubule assembly: What stabilizes growing microtubules?, *Biochemistry* **38**, 8179-8188 (1999).
- [124] V. VanBuren, D. J. Odde, and L. Cassimeris, Estimates of lateral and longitudinal bond energies within the microtubule lattice, *Proceedings of the National Academy of Sciences of the United States of America* **99**, 6035-6040 (2002).

Bibliography

- [125] M. E. de Dood, *Catastrophes of stalled microtubules*, undergraduate thesis, FOM institute AMOLF, Amsterdam (2002).
- [126] A. Davis, C. R. Sage, C. A. Dougherty, and K. W. Farrell, Microtubule dynamics modulated by guanosine triphosphate hydrolysis activity of beta-tubulin, *Science* **264**, 839-842 (1994).

Summary

Living cells contain specialised proteins that are designed to bind to identical duplicates, which causes them to assemble into long filamentous structures that form the cytoskeleton of the cell. It is believed that the assembly as well as disassembly of these filaments can generate forces that are important for various forms of cellular motility like chromosome and nuclear positioning. Evidence that underlines the importance of these forces is summarised in chapter 1. Other force generation mechanisms such as motor proteins are the focus of many investigations. In contrast, little is known about assembly-related forces.

This thesis deals with microtubules, long stiff protein aggregates that are assembled from the cytoskeletal protein tubulin. Because of their stiffness, experimentally observable microtubules with lengths of several micrometers do not collapse under the application of piconewton forces. This makes them well suited for the study of assembly forces. Microtubules show a remarkable assembly behaviour that is utilized by the cell. They alternate between phases of steady elongation and rapid shortening. This behaviour is termed dynamic instability and the transition to shortening is called a catastrophe. Parameters like growth velocity and catastrophe time, i.e. the mean time until a catastrophe, are clearly regulated by the biochemical machinery of the cell in order to perform different cellular functions. The work presented in this thesis is aimed at answering questions like: ‘How much force can one microtubule generate?’, ‘How does an opposing force change the parameters that describe dynamic instability?’ and ‘What can we learn from this about the mechanism of force generation and dynamic instability?’.

Methods developed to measure force generation by single microtubules are described in chapter 2. Microtubules grown from substrate-attached nucleation sites were made to push against barriers. Rigid barriers of silicon-monoxide were created using photolithographic techniques and nucleation sites were prepared from modified microtubules. Rapid nucleation of dynamic microtubules was observed from these sites. Microtubules were imaged using video enhanced differential interference contrast (DIC) microscopy. Methods were developed to trace and analyse the elastic deformation of a microtubule caused by the continuation of growth after barrier contact. The force that acts on the tip of a buckled microtubule was calculated using the flexural rigidity of microtubules.

The flexural rigidity of microtubules can be accurately measured by analyzing thermally driven shape fluctuations preferentially using a mode analysis. A method applicable to growing microtubules was developed and tested in chapter 5. The dynamics of the 1st mode was too slow to be analyzed but up to four higher order modes yielded consistent rigidity values. Faster growing microtubules appeared to be less rigid. A more

Summary

elaborate study is needed to study this phenomenon, which was not reported earlier. Defects inside the microtubule lattice may provide an explanation.

Shorter microtubules need to generate more force to buckle themselves compared to short microtubules. In our experiments, we did not observe buckling of microtubules shorter than 5 micrometer, from which we concluded that the force needed to stop growth is on the order of 10 piconewton. At this stall force, the growth process is in equilibrium and the rate of subunit addition (on-rate) equals that of subunit removal (off-rate).

The elastic restoring force of a buckled microtubule opposes elongation. As a consequence, both the microtubule growth velocity and the catastrophe time were seen to decrease with increasing force. We quantitatively studied the force-velocity (chapter 3) and velocity-catastrophe (chapter 4) relation. The ratio between growth velocity at a certain load and the initial, zero load, growth velocity was independent of the initial velocity. Under load, the velocity-catastrophe relation resembled that of free growing microtubules. For stalled microtubules we measured a catastrophe time that was independent of the velocity at which the microtubule grew initially towards the barrier. These observations indicate that a growth opposing force decreases the on-rate but does not change the off-rate during assembly. Some evidence was obtained for a force independent off-rate during the stage of rapid shortening, but this study suffered from experimental uncertainties. By comparing the measured force-velocity relation to predictions by Brownian ratchet models that describe growth under a load, we estimated that the approximately 13 protofilaments that form the microtubule's wall are to some degree able to elongate independently of each other. As a consequence, the end structure of a microtubule is likely to be frayed and the growth process is not optimised to generate maximum force.

Many issues regarding microtubule dynamics and especially catastrophes, such as the hydrolysis rate of tubulin bound guanosine tri-phosphate and the structure of the elongating tip are not settled yet. In general there is a demand for experiments that allow a detailed study of processes at the microtubule tip. Knowing these processes would allow for a better understanding of the mechanisms of force generation and bio-chemical control by other proteins over dynamic instability. In chapter 6 we present first results on microtubule force generation measurements with optical tweezers that support the earlier results and in principal allow for a better estimation of the stall force. This technique enables the analysis of microtubule growth at a millisecond and nanometer scale. Detailed investigations of processes such as spontaneous velocity fluctuations are within reach. Results on an experiment in which motor proteins are used to couple microtubule elongation or shortening to directed motion of a glass bead are discussed in chapter 6 as well. The study of these kinds of connections that occur in living cells is important for unraveling the individual roles of force generation by filamentous assembly and by motor proteins. These two mechanisms are tightly coupled during processes such as cell division.

Summary

By studying force generation of individual microtubules, we obtained a good view on the amount of force that a microtubule can generate and how force changes growth velocity and catastrophe time. With these intrinsic properties of microtubules in mind we can better anticipate their behavior inside living cells. Recent reports on microtubule dynamics in yeast demonstrate clearly that assembly forces are indeed utilised and that force effects both the growth velocity and catastrophe time inside these cells.

In this thesis we studied the force generating properties of microtubules. Many of the described concepts will as well be applicable to other filamentous systems such as actin. Hopefully in the near future new experiments on force generation will be reported that will enable us to compare the force generating abilities of different biopolymers.

Samenvatting

De titel 'Krachtgeneratie door groeiende microtubuli', tracht het onderwerp van dit proefschrift te omschrijven. Eén korte zin is gelukkig niet genoeg om ruim vier jaar onderzoek samen te vatten en ik zal hier proberen uit te leggen welke vragen we hebben gesteld en wat we hebben ontdekt.

Het begrip kracht kennen we uit het dagelijks leven, maar het wordt door natuurkundige wetten kwantitatief gemaakt en uitgedrukt in newtons. Eén newton komt overeen met de kracht die je voelt wanneer je bijvoorbeeld een tomaat van 100 gram in je hand laat rusten. In dit proefschrift staan krachten beschreven welke een biljoen maal zo klein zijn (piconewtons). Deze krachten worden gegenereerd door groeiende microtubuli, kleine buisjes gemaakt van eiwitten die overvloedig aanwezig zijn in onze lichaamscellen. Samen met andere eiwitstructuren generen microtubuli de krachten die nodig zijn om bijvoorbeeld een cel te delen of van binnen uit te structureren. Met de hedendaagse kennis over het DNA hebben we van alle eiwitten in ons lichaam een ruwe bouwtekening in handen. Veelal moet echter nog worden uitgezocht hoe eiwitten samenwerken om bepaalde processen in cellen mogelijk te maken. Hoe eiwitten samenspannen om een krachtenspel mogelijk te maken dat vorm geeft aan levende cellen wordt bijvoorbeeld nog slecht begrepen. Het onderzoek hier beschreven kan bestempeld worden als biofysisch, waarmee we met natuurkundige kennis over krachten en dynamica proberen biologische processen te begrijpen.

Een microtubulus is een dunne flexibele buis opgebouwd uit eiwitten (zie figuur 1.1). Hoe kan zo'n bouwwerk duwkrachten uitoefenen? We kunnen een microtubulus vergelijken met een toren van elastische lego steentjes. Elk lego steentje in de toren is een tubuline eiwit dat zichzelf vasthoudt aan zijn burens. Door nieuwe steentjes bovenop toe te voegen kan de toren groeien. De langste microtubuli in onze cellen hebben een lengte vergelijkbaar met de dikte van een haar (100 micrometer). De dikte van de microtubulus zelf is ruim een factor duizend kleiner (25 nanometer). Stel nou dat we onze flexibele lego toren zo hoog bouwen dat we het plafond bereiken. Nieuwe steentjes passen niet meer en we moeten eerst kracht uitoefenen om de toren iets te verbuigen om ruimte te maken voor nieuwe steentjes. Tubuline eiwitten hebben echter zo'n grote hechttingsdrang voor het uiteinde van een microtubulus dat ze spontaan de buis kunnen buigen en daarmee dus een kracht kunnen uitoefenen op het plafond. De buis blijft dus toch groeien. In de cel wordt de rol van het plafond overgenomen door bijvoorbeeld de afbakening van het plasmamembraan of door een chromosoom dat in de weg ligt van een groeiend microtubulus. We kunnen nu een methode bedenken om deze zeer kleine duw krachten te meten. De kromtestraal van een gebogen microtubulus kan worden opgemeten en vertaald

Samenvatting

naar de kracht welke wordt uitgeoefend op het uiteinde. Hiervoor is kennis over elasticiteits wetten en de elasticiteit van microtubuli vereist.

Wanneer je met een sterke microscoop naar een microtubulus kijkt, valt op dat deze nooit stil ligt. Anders dan in onze macroscopische wereld is er voor de microscopische microtubulus nooit rust. Continue botsen zeer bewegelijke watermoleculen tegen de wand van een microtubulus. Het resultaat van al deze tikjes is een golfachtige beweging van de microtubulus. De flexibiliteit van microtubuli konden we verkrijgen door de grootte of uitslag van de golfpatronen nauwkeurig te bestuderen (hoofdstuk 5). Met onze analyse hebben we de flexibiliteit gemeten van microtubuli terwijl ze groeiden, iets wat niet mogelijk was met een eerder in de literatuur beschreven gelijksoortige aanpak. We hebben een grotere flexibiliteit gemeten voor snel groeiende microtubuli.

We hebben microtubuli zichzelf laten krom duwen door ze te laten groeien tegen zeer kleine (2 micrometer hoge) barrières. Microtubuli groeiden vanaf voorgeprepareerde stukjes buis vastgeplakt tussen de barrières (hoofdstuk 2). Inderdaad bereikten sommige microtubuli de barrières en kwamen ze krom te staan. Korte microtubuli die dichtbij de barrière vast zaten groeiden duidelijk minder snel tijdens het duwen en zij die heel kort waren groeiden helemaal niet en bleven recht. Een lange toren is makkelijker te buigen dan een korte en om dezelfde reden moet een korte microtubulus meer kracht genereren om zichzelf te buigen. Blijkbaar stopt het groeiproces bij een bepaalde 'stop'-kracht, welke in de buurt van de 10 piconewton bleek te liggen. Door vele microtubuli te bestuderen konden we de groeisnelheid als functie van de kracht kwantificeren (hoofdstuk 3). De plakkans van losse eiwitten aan het uiteinde van de microtubulus wordt lager bij toenemende kracht en groei gaat daardoor trager. Bij de stopkracht is er evenwicht tussen het aantal eiwitten dat per seconde vastplakt en zij die van het uiteinde afvallen. Door onze meetresultaten te vergelijken met theoretische voorspellingen konden we uitspraken doen over de vermoedelijke rafelige structuur van het uiteinde van een microtubulus en over de krachtafhankelijkheid van de plak- en afvalkans van eiwitten. Met deze informatie gaan we het groeiproces van microtubuli steeds beter begrijpen.

Eén van de dingen die we nog niet begrijpen is hoe een microtubulus soms spontaan een periode van groei beëindigt en overschakelt naar snelle krimp. Er is sprake van een instabiel evenwicht. Binnenin de microtubulus vindt een chemische omzetting plaats welke de vorm van het tubuline eiwit verandert. Na deze omzetting is de afvalkans vele malen groter, en wil de microtubulus eigenlijk uiteen vallen, beginnend bij het uiteinde. Daar heeft de chemische omzetting echter nog niet plaats gehad en het uiteinde stabiliseert dus de microtubulus. Wij hebben ontdekt dat de gemiddelde duur van een groeiperiode met wel een factor vijftig kan worden verkort wanneer een microtubulus tijdens het groeien kracht moet uitoefenen (hoofdstuk 4). Kracht destabiliseert dus het uiteinde. Door veel van dit soort kwantitatieve experimenten te doen krijgen we meer inzicht in het mechanisme dat schuilgaat achter de omschakeling van groei naar krimp.

Samenvatting

Waarom ben ik nou zo enthousiast over de beschreven resultaten? We weten nu hoe kracht genererende microtubuli zich gedragen in een model omgeving, en daardoor weten we nu beter wat voor gedrag we mogen verwachten in levende cellen. Er zijn reeds rapportages over onderzoek aan gist cellen welke aangeven dat kracht in levende cellen een gelijksoortig effect heeft op groeisnelheid en krimpkans. De complexiteit in levende cellen is vaak overweldigend, maar met onze resultaten in het achterhoofd zijn experimenten in levende cellen beter te interpreteren. Duwkrachten zijn belangrijk voor levende cellen (hoofdstuk 1) en de intrinsieke eigenschappen van microtubuli die we nu hebben gemeten bepalen mede hoe processen precies verlopen.

In het laatste hoofdstuk van dit proefschrift staan de eerste resultaten beschreven van twee vervolg experimenten. Veel vragen zijn nog niet beantwoord en nieuwe experimenten blijven nodig. Met behulp van een zeer intense lichtbundel, een optisch pincet, hebben we microtubuli vast kunnen pakken om krachtgeneratie nog nauwkeuriger te bestuderen op een kortere tijd en lengte schaal. Verder beschrijven we de hechting van een object aan het uiteinde van een groeiend of krimpend microtubulus met behulp van zogenaamde motor-eiwitten. Zulke dynamische connecties zijn belangrijk in levende cellen bijvoorbeeld bij de koppeling van een microtubulus aan een chromosoom. Al dit onderzoek is erop gericht om te begrijpen waarom een cel niet een vormeloos zakje met eiwitten is, maar een goed georganiseerde dynamische structuur heeft. In de toekomst zullen we dankzij het vele onderzoek dat in diverse laboratoria gebeurt beter begrijpen hoe een cel werkt, maar ook waarom hij af en toe faalt en ziektes veroorzaakt.

Nawoord

Experimenteren doe je op AMOLF gelukkig niet alleen en veel mensen hebben of een actieve bijdrage geleverd of regelmatig hun interesse getoond in mijn onderzoek. Dit heb ik altijd zeer op prijs gesteld. Voor het doen van biofysisch onderzoek is in korte tijd een zeer stimulerende werkomgeving gecreëerd.

De goede technische ondersteuning heeft het werk enorm vergemakkelijkt. Bij E&I kun je altijd aankloppen voor eerste hulp bij computers of elektronen. Marco Konijnenburg heeft met zijn computer programma's de analyse van microscoopbeelden enorm vereenvoudigd. Idsart Attema en Hans ter Horst waren altijd bereid om snel iets te fixen en Duncan Verheijde maakte de elektronica voor de thermosstaat. Maurice van de Boer heeft heel wat dikke lagen in het dunne lagen lab neergelegd en Hans Zeijlemaker stond altijd paraat met goede adviezen. Met de werkplaats van Wim Brouwer was het altijd goed en snel zaken doen. Jan, Menno, Wim, Ruud, Henk, Martijn, Jan-Willem en Hildo hebben mooie dingen gemaakt. Iliya Cerjak, Dirk-Jan Spaanderman en Joop van Dorsselaer mochten nooit iets groots ontwerpen, maar die kleine spulletjes zijn toch ook groots geworden.

De groep 'bio-assembly and organisation' begon heel klein maar is uitgegroeid tot een leuke en stimulerende groep mensen. In het begin waren er de pioniers: Sander van Doorn, Cendrine Faivre-Moskalenko en Astrid van der Horst. In die tijd (ik word oud) moesten we nog zelf onze pipetpunten bestellen. Nu zorgen Michiel Witlox en Anne-Marie Post-Langen hiervoor evenals voor heel veel andere zaken. Later kwamen Gerbrand Koster, Marco Consentino-Lagomarsino, Wouter Roos, Jacob Kerssemakers, Martijn van Duijn, Chris Retif, Henk Bar en Annebeth Kraij de groep versterken. De stage studenten Yvette de Natris, Eva Riemsdag en Mathilde de Dood hebben allen veel werk verricht waarvan ik veel profijt heb gehad.

Mijn experiment heeft wel geteld drie locaties gehad binnen Amolf, waaronder een ruimte gemaakt van gipsplaten en bouwzijl. Ed, Willem, Iwan en André hebben heel wat planken verhangen en leidingen gelegd. Verder ben ik zelf vaak verhuisd binnen het lab en heb ik met veel mensen een werkkamer gedeeld. De meeste tijd heb ik doorgebracht met de bewoners van kamer 141. Het was erg leuk om met jullie een kamer te delen. I apologise to my new 191-roommates Mark Miller and Tanja Shilling for chilling our room now and then. 'De overloop' is dankzij alle 'zacht-gecondenseerde' mensen een zeer geriefelijke werkplek geworden. Bij Alfons van Blaaderen en zijn groepsleden Jacob Hoogenboom, Dirk Vossen en Anand Yethiraj kon ik altijd terecht met allerhande vragen. Zij waren prettige labgenoten en leverancier van vele bolletjes. With Cătălin Tănase I had many discussions about microtubule issues and he was a true Mathematica hero.

Nawoord

Binnen en buiten het lab was er altijd voldoende afleiding. Bieren in de ‘East of Eden’ of ‘De Brouwerij’, professionele raket programma’s, lunch bij de biologie, bijpraten bij de transportdeur, zwemmen..... Voor een leuke tijd op Amolf waren mede verantwoordelijk: Iliya, Gerard, Wim, Frans, Han, Martin, Bart, Bernd, Steven, Paul, Hildebrand, Mike, Richard, Aletta, Gert, Oscar, Gisela, Jerre, Marc, Sander en Jorrit.

Geheel buiten het lab om hebben veel mensen gezorgd voor afleiding en een leuke tijd in Amsterdam. Van mijn vrienden wil ik in het bijzonder noemen: Gerben, Christy, Jan, Dorine, Marc, Clarisse en Oscar. Mijn broers Michiel en Bert hebben de afgelopen jaren het belang van microtubuli flink gerelativeerd met een goede mix van interesse en humor. Katja, bedankt voor je vrolijkheid en goede zorg met name tijdens het schrijven van dit proefschrift. Tenslotte wil ik hier graag mijn ouders bedanken voor hun steun en belangstelling door de jaren heen.

Curriculum Vitae

Marcel Ernestus Janson werd geboren op 6 september 1972 in Drachten. Na het behalen van het havo diploma in 1989 aan de chr. scholengemeenschap 'De Brug' in Lelystad begon hij met de studie Technische Natuurkunde aan de 'Hogeschool Enschede' waarvoor hij in 1993 met lof slaagde. Voor deze laatste opleiding volgde hij bedrijfsstages bij 'Philips Components' in Eindhoven en het 'Energieonderzoek Centrum Nederland' te Petten. Zijn afstudeerstage bracht hij door bij de vakgroep 'Lage Temperaturen' van de 'Universiteit Twente'. Onder leiding van prof. dr. ir. H.H.J. ten Kate werkte hij aan een meetopstelling voor magnetische eigenschappen van supergeleiders. Aan diezelfde universiteit begon hij in 1993 de opleiding 'Technische Natuurkunde' welke hij in 1996 afsloot met een afstudeeropdracht bij het lasercentrum van het 'Academisch Medisch Centrum' te Amsterdam onder leiding van dr. ir. H.J.C.M. Sterenborg. Hier onderzocht hij een meetmethode voor tripletvervaltijden van medisch toepasbare porfyries. In 1997 trad hij in dienst als onderzoeker in opleiding (OIO) bij het FOM Instituut voor Atoom- en Molecuulfysica in Amsterdam. De resultaten van zijn promotieonderzoek in de groep van prof. dr. M. Dogterom staan beschreven in dit proefschrift.